Real-Time Rail-Track Monitoring System Employing Innovative Wavelength Diversity Technique in Distributed Optical Fibre Sensors

N R Lalam

PhD

2018

Real-Time Rail-Track Monitoring System Employing Innovative Wavelength Diversity Technique in Distributed Optical Fibre Sensors

Nageswara Rao Lalam

A thesis submitted in partial fulfilment of the requirements of the University of Northumbria at Newcastle for the degree of

Doctor of Philosophy

Research undertaken in the Faculty of Engineering and Environmental Sciences

May 2018

Abstract

Brillouin based distributed fibre sensors gained a lot of attention in recent years for structural health monitoring applications, due to their higher sensing range over tens of kilometres and distributed measurement capability of simultaneous strain and temperature. In Brillouin optical time domain reflectometry (BOTDR) system, the signal-to-noise ratio (SNR) determines the sensing performance of the system. However, the SNR is limited by the restricted maximum input pump power, which is limited by the non-negligible nonlinear effects, such as stimulated Brillouin scattering.

In this research, a novel wavelength diversity technique is proposed to enhance the SNR, hence improve the strain and temperature measurement accuracies, which is required for accurate rail-track condition monitoring. In addition, this research work presents the following contributions (*i*) a simple, low-cost passive depolarizer is adopted to reduce the polarization noise; (*ii*) an inline erbium-doped fibre amplifier (EDFA) is employed at a certain distance to amplify the attenuated pulse in order to improve the sensing range; and (*iii*) a cost-effective reference Brillouin ring laser is used in BOTDR system to overcome the complexity of the receiver bandwidth reduction.

The proposed wavelength diversity BOTDR system combined with a passive depolarizer and Brillouin ring laser is validated over a 50 km sensing fibre with a 5 m spatial resolution. The SNR is improved by 5.1 dB, which corresponds to 180% improvement compared to a conventional BOTDR system. Whereas, the strain and temperature accuracies at a 50 km fibre distance are ±10 με and ±0.45^{o}C, respectively. Furthermore, for the first time, simultaneous integration of long-term evolution (LTE) radio-over-fibre (RoF) data system and BOTDR sensing system using a single optical fibre is proposed and demonstrated. The error vector magnitude (EVM) performance of LTE-RoF data system is analysed for three modulation formats of QPSK, 16-QAM and 64-QAM in the presence of various BOTDR sensing powers.

Acknowledgements

Firstly, I would like to express my sincere thanks to my principal supervisor Dr Wai Pang Ng for his continuous support, motivation, guidance and encouragement throughout my study at Northumbria University. I am very fortunate to have such great supervisor with excellent experience, who not only guided me through the technical phase but also strongly advised on being a good researcher and overall on how to be a person with an excellent personality. I am also grateful to my second supervisor Dr Xuewu (Daniel) Dai for his help and continued support. My special thanks to Dr Qiang Wu and Dr Richard Fu for valuable discussions and useful feedback.

Northumbria University studentship had played a big role in my PhD study, thus I would like to express my gratitude to the Faculty of Engineering and Environmental Sciences, Northumbria University. Moreover, I would like to thank British Council, UK for giving me three international travel grants and the opportunity to explore these research findings at international knowledge exchange research workshops held at Istanbul, Mexico City and Abu Dhabi organised by a British Council. Furthermore, I would like to convey my sincere acknowledgement to the members of the Optical Communications Research Group (OCRG) and Smart Sensors Research Group at the Department of Mathematics, Physics and Electrical Engineering, Northumbria University for their help and support during my study.

I would like to convey my sincere acknowledgement to my parents, sister and brother for their continuous support and encouragement. I owe everything that I have achieved to my family. Finally, I dedicate this thesis to my parents and my fiancée Swetha.

Declaration

I declare that the work contained in this thesis has not been submitted for any other award and that it is all my own work at Northumbria University. I also confirm that this work fully acknowledges opinions, ideas and contributions from the work of others.

The ethical clearance for the research presented in this thesis has been approved. The approval has been sought and granted by the Faculty Research Ethics Committee on 15/12/2015.

I declare that the word count of this Thesis is 36,301

Name: Nageswara Rao Lalam

Signature:

Date:

Table of Contents

Glossary of Acronyms

4G	4th generation
ASE	Amplified spontaneous emission
AWGN	Additive white Gaussian noise
BFS	Brillouin frequency shift
BGS	Brillouin gain spectrum
BOCDA	Brillouin optical correlation domain analysis
BPF	Band pass filter
B-PD	Balanced photodetector
BOSA	Brillouin optical spectrum analyser
BOTDA	Brillouin optical time domain analysis
BOTDR	Brillouin optical time domain reflectometry
BRL	Brillouin ring laser
BS	Base station
CRN	Coherent Raleigh noise
CS	Central station
DAS	Distributed acoustic sensing
DFB-LD	Distributed feedback laser diode
DD-MZM	Dual drive Mach-Zehnder modulator
DTS	Distributed temperature sensor
DWDM	Dense wavelength division multiplexing
EDFA	Erbium-doped fibre amplifier
EMI	Electromagnetic interference
EOM	Electro-optic modulator

ESA	Electrical spectrum analyser
EVM	Error vector magnitude
FBG	Fibre Bragg grating
FFT	Fast Fourier transform
FTTB	Fibre to the building/basement
FTTC	Fibre to the cabinet
FTTH	Fibre to the home
FTTN	Fibre to the node
FUT	Fibre under test
FWHM	Full width at half maximum
FWM	Four-wave mixing
GAWBS	Guided acoustic wave Brillouin scattering
ISO	Isolator
InGaAs	Indium Gallium Arsenide Phosphide
$LiNbO_3$	Lithium Niobate
LO	Local oscillator
LNA	Low noise amplifier
LPG	Long period grating
LTE	long-term evolution
MI	Modulation instability
MMF	Multimode fibre
MZM	Mach-Zehnder modulator
NEP	Noise equivalent power
OFDM	Orthogonal frequency division multiplexing
ORR	Office of rail regulations

OSA	Optical spectrum analyser
OSNR	Optical signal-to-noise ratio
OTDR	Optical time domain reflectometer
PBC	Polarization beam combiner
PBS	Polarization beam splitter
PC	Polarization controller
PCF	Photonic-crystal fibre
PS	Polarization scrambler
PD	Photodetector
PFGI-POF	Perfluorinated graded index-plastic optical fibre
PMF	Polarization maintaining fibre
PPM	Public performance measurement
PPP	Pulse pre-pump
PSP	Phase shift pulse
QAM	Quadrature amplitude modulation
QPSK	Quadrature phase-shift keying
RCM	Remote condition monitoring
RF	Radio frequency
RIN	Relative intensity noise
RMS	Root-mean-square
RoF	Radio over fibre
SBS	Stimulated Brillouin scattering
SMF	Single mode fibre
SNR	Signal-to-noise ratio
SpBS	Spontaneous Brillouin scattering

SPM	Self-phase modulation
SRS	Stimulated Raman scattering
TIA	Transimpeadance amplifier
VOA	Variable optical attenuator
VSG	Vector signal generator

Glossary of Symbols

A	Amplitude
A_{eff}	Effective fibre area
α	Fibre attenuation
α_B	Brillouin scattering coefficient
α_R	Rayleigh scattering coefficient
B	Photodetector bandwidth
c	Light velocity
C_ε	Strain coefficient
C_T	Temperature coefficient
$C_\varepsilon^{P_B}$	Strain coefficient of Brillouin peak power
$C_\varepsilon^{\nu_B}$	Strain coefficient of Brillouin frequency shift
$C_T^{P_B}$	Temperature coefficient of Brillouin peak power
$C_T^{\nu_B}$	Temperature coefficient of Brillouin frequency shift
d_m	Correlation peak intervals
$\Delta\chi$	Dielectric susceptibility
$\Delta\varepsilon$	Strain change
ΔP_B	Brillouin peak power change
Δt	Time delay
ΔT	Temperature change
$\Delta\rho$	Material density change

Δv_B	Brillouin linewidth
Δv	Frequency spacing
Δz	Spatial resolution
δ	Sweep frequency step
E	Electric field
E_B	Brillion signal electric filed
E_{LO}	Local oscillator electric filed
$\in$	Dielectric permittivity
$\in_o$	Vacuum permittivity
f	Phonon frequency
f_m	Modulation frequency of the laser
g_B	Brillouin gain coefficient
g_R	Raman gain coefficient
Γ_B	Acoustic damping coefficient
γ	Nonlinear coefficient
γ_e	Electrostrictive coefficient
h	Plank's constant
$h\nu$	Photon energy
I_{beat}	Beat signal intensity
I_p	Pump intensity
I_{ph}	Photocurrent
I_s	Stokes intensity

i_{th}	Thermal noise
i_{sh}	Shot noise
$< i^2_{E-noise} >$	Noise power form the electronic devices
K	Bulk modulus
k_p	Polarization coefficient
k	Boltzmann constant
k_B	Wave vector of acoustic wave
k_p	Wave vector of pump
k_s	Wave vector of Stokes
$\chi^{(1)}$	First order linear dielectric susceptibility
L	Fibre length
L_{eff}	Effective fibre length
λ_p	Pump wavelength
λ_s	Stokes wavelength
λ_B	Brillouin wavelength
μ_o	Vacuum permeability
N	Number of pump wavelengths
N_{avg}	Number of averages
$N_{phonons}$	Phonon population distribution
n	Refractive index
n_2	Nonlinear refractive index

ω_B	Angular frequency of acoustic wave
ω_p	Angular frequency of pump
ω_s	Angular frequency of Stokes
P	Induced polarization
p	Pressure
p_{el}	Electrostrictive pressure
p_{12}	Elasto-optic coefficient
P_B	Brillouin power
P_{LO}	Local oscillator power
P_{th}^{SBS}	Stimulated Brillouin scattering threshold power
P_{th}^{SPM}	Self-phase modulation threshold power
P_{th}^{SRS}	Stimulated Raman scattering threshold power
P_{T_B}	Total Brillouin power
$P_{T_{LO}}$	Total local oscillator power
q	Elementary charge
R_D	Photodetector responsivity
R_L	Load resistance
ρ	Material density
ρ_o	Mean material density
S	Backscattered signal capture fraction
$S_r(n)$	Received OFDM signal

$S_t(n)$	Transmitted OFDM signal
s	Entropy
σ_v	BFS uncertainty
T	Temperature
t	Time
τ_a	Acoustic lifetime
θ	Angle
$\theta_{p,s}$	Angle between the pump and Stokes wave
V_{bias}	MZM bias voltage
V_{RF}	RF voltage
V_π	Half-wave voltage
v	Optical frequency
v_a	Acoustic velocity
v_B	Brillouin frequency shift
v_g	Group velocity
v_p	Pump frequency
W	Pulse width
Z	Fibre distance

List of Figures

List of Tables

Chapter 1
Introduction

1.1 Introduction and Motivation

In 1966, Charles Kuen Kao [2] proposed an optical fibre made with a thin piece of a glass material as a transmission medium for communication and is notably known as the "Father of fibre optics". In 2009, he was awarded a Noble Prize in Physics for his pioneering work on optical fibres. When optical fibre were first invented, the attenuation exceeded 1000 dB/km [3]. In 1960, Miaman [4] invented the laser at a better wavelength of 1 μm, hence the attenuation was greatly reduced to 20 dB/km. In 1969, scientists concluded that the fibre material impurities caused the high attenuation in the fibres. In 1972, Corning Glass Works made a silica multimode fibre with minimised material impurities and achieved a loss of 4 dB/km [5]. During the 1970s, the optical fibres got the centre of interest for nonlinear optics community as well. In 1981 [6] the use of single-mode silica optical fibre over 44 km was demonstrated and the fibre attenuation was reduced to 0.2 dB/km at 1.55 μm wavelength. Since then, the optical fibre has been undergone intensive investigations and been applied to many different fields of applications. Apart from its low attenuation, the optical fibre demonstrates other advantages, such as low cost, small size, light weight, high bandwidth and immunity to electromagnetic interference (EMI). Fibre optic communication has become the ultimate choice for the gigabit and even beyond gigabit data transmission. Recent advances in fibre optic communication have significantly changed the telecommunications industry.

Whilst, the role of optical fibres in the communication industry is well known, the technology has been extended to another emerging application, optical fibre sensing. Among other kinds of sensors, optical fibre sensors have several advantages, such as high sensitivity, high measurement resolution, small size, light weight, immunity to EMI, resistance to chemical corrosion, remote sensing capability, ease of installation and harsh environmental capability [7]. The tremendous growth of fibre optic sensors can be applied to various sensing measurements such as strain, temperature, vibration, rotation, humidity and refractive index. Fibre sensors gradually become central for many industrial applications [8, 9], such as (i) structural health monitoring (rail-track, oil/gas pipelines, aeroplanes, dams/bridges, wind turbines, critical infrastructures), (ii) medical (blood flow, pH content, gas analysis, glucose content, breath rate) and (iii) military applications (aircraft, border security monitoring, fire detection, ships monitoring). Fibre sensors can be classified into three categories; (i) point based fibre sensors (ii) quasi-distributed fibre sensors and (iii) distributed fibre sensors. The point sensors, such as fibre Bragg grating (FBG) and long period grating (LPG) measures only at the specific location of interest, whose length is typically 5 to 10 cm [10]. Point sensors can be multiplexed (known as quasi-distributed) up to certain sensing range, but this will greatly increase the system cost and complexity. For distributed fibre sensors, the whole fibre medium acts as a sensing element in the range of several kilometres.

Large structural infrastructures, such as rail-track, railway tunnels/bridges, buildings, dams and pipelines are subjected to many unforeseen factors and events during their lifetime. They can be inspected manually, but the internal stresses and strains affecting their infrastructure remain all but impossible to measure in a practical efficient way. Structural health monitoring allows control of the safety and integrity of a structure over time. The monitoring of structural deformation of the entire structure is difficult with a point or quasi-distributed fibre sensors. Therefore, monitoring the health condition of the

infrastructures have become an ultimate driving force for the development of distributed fibre sensors. In the last two decades, distributed fibre sensors have gained a lot of attention and has seen a tremendous growth. Distributed fibre sensors offer an innovative technology for a spatially distributed measurement based on Raleigh, Brillouin and Raman scattering. By analysing the backscattered signal frequency, intensity and phase, one can realize a distributed measurement of strain, temperature and vibration over tens of kilometres [11, 12]. Large infrastructures, for instance rail-track and railway tunnels/bridges, are subject to continuous stress and temperature variations that produce flaws. Moreover, minor cracks due to heavy loads or temperature variations over time will lead to dramatic structural failure. The distributed fibre sensors market for different applications are illustrated in Figure **1.1**. The distributed fibre sensors are widely adopted in oil/gas industry and several structural health monitoring applications to enhance the inspection efficiency and distributed measurement capability. In 2016, the distributed fibre sensor market in the world stood at approximately US $1.18 billion. The market was predicted to approach more than US $1.85 billion in 2018 [13].

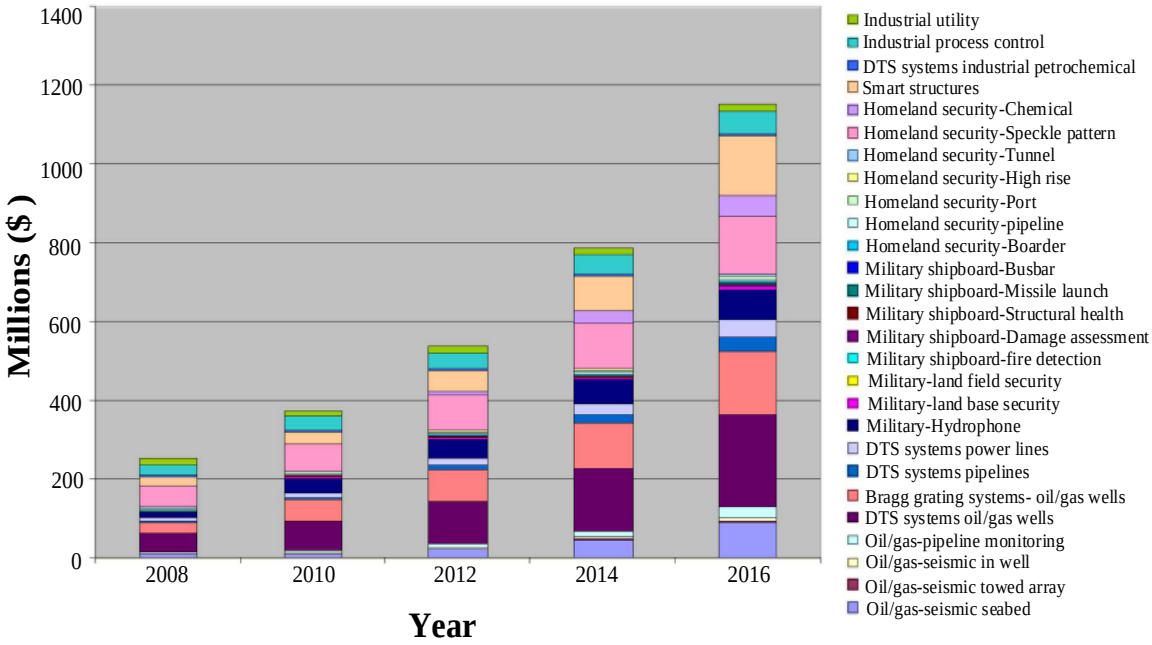

Figure 1.1. Distributed fibre optic sensors market prediction- Sep' 2017 [14]
(DTS=distributed temperature sensing)

1.2 Problem Statement

Modern British railways are required to operate trains with a high level of safety, reliability and punctuality. During 2016/2017, the British national PPM (public performance measurement) percentage is very low as 84.3% [15]. The PPM is defined as the percentage of trains arriving at the terminating station within ten minutes of commuter services. Normally in the UK, rail-track monitoring is carried out through visual inspection by a geometry car to detect the infrastructure failures. Some regions use a point sensors such as electrical strain gauges and temperature sensors. Rail-track infrastructure is affected by the extreme weather conditions, tons of load on track, landslides, track ballast deformation and flooding along the rail-track [16, 17]. The rail-track deformations and buckling-related derailments are a huge economic burden to the railway industry. As per UK's office of rail regulations (ORR) periodic review, during the 2015 summer heatwave, 137 track buckling events were reported within the UK, at a reportable damage of £2.5 million [18, 19]. The economic damages were projected to increase up to £4.5 million by the 2030s [19]. Current, conventional monitoring techniques are expensive and ineffective in achieving accurate condition monitoring of the rail-track for long life operation. The worst train accidents occurred in the world recently where the rail-track are inspected by the current generation of technology. Therefore, it is essential to deploy real-time monitoring system of the rail-track infrastructure with more accurate, cost-effective (£202/mile [20]) and efficient way.

In the field of railway/underground industry, the distributed fibre sensor is an innovative technology, due to easy maintenance, remote condition monitoring and distributed measurement capability of both strain and temperature in real-time. An installed optical fibre along the rail-track can monitor the health condition of the rail-track for up to several tens of kilometres. Recently, Brillouin based distributed fibre sensors

gained lots of attention, due to their advantages compared to Raman based sensors. Such popularity has emerged from their ability to measure both the strain and temperature simultaneously for a sensing range of several kilometres. However, the measurement accuracy and sensing range in Brillouin based distributed sensors are still limited by some factors, such as the weak nature of the backscattered Brillouin signal (typically at nW), silica fibre double path loss (typically 0.4 dB/km at 1550 nm), noise sources and nonlinear effects that limit the maximum input pump power. If the input pump power is above the nonlinear threshold, it will result in a rapid depletion of the pump power; hence reduce the sensing range and accuracy of strain and temperature. In Brillouin based distributed fibre sensors, the signal-to-noise ratio (SNR) determines the sensing performance. The SNR is primarily governed by the injected pump pulse power into the sensing fibre. Increasing the injected pump power into the sensing fibre will improve the SNR but the level of the pump power is limited by the non-negligible nonlinear effects. Therefore, Brillouin based distributed fibre sensors have a restricted SNR, thus limited measurement accuracy and sensing range. However, monitoring the rail-track infrastructure essentially requires higher measurement accuracy ($<\pm 0.5^{o}$C and $<\pm 10$ με for temperature and train, respectively) for a sensing range of more than 50 km [21].

On the other hand, providing a new fibre infrastructure for rail-track monitoring using distributed fibre sensor system is a huge economic burden and high complexity, which discourages the wide-spread use of distributed fibre sensor system. If we use the existing active data transmission fibre infrastructure for distributed sensing, this will turn out to be a cost-effective and efficient way to use with less complex. For example, rail industry uses a fibre link installed along the trackside for data transmission. The simultaneous integration of distributed sensing system with existing optical fibre cable can be used for remote condition monitoring of landslides, track ballast deformation, electric-pole/tree fall, snow drifts, flooding and lineside fire detection in real-time.

For measuring distributed strain and temperature, two Brillouin-based techniques are widely used; the Brillouin optical time domain reflectometry (BOTDR), based on spontaneous Brillouin scattering (SpBS) and Brillouin optical time domain analysis (BOTDA), based on stimulated Brillouin scattering (SBS). The BOTDR system features simple implementation schemes and only requires access to the single end of the sensing fibre. Whereas, the BOTDA system requires access to both ends of the sensing fibre with complex system implementation. The main aim of this research into BOTDR system is to address its limitations in order to improve the SNR and overall sensing performance. The work described in this thesis is based on the authors own research in collaboration and discussion with the members of research groups, Optical Communications Research Group (OCRG) and Smart Sensors research group at Northumbria University. Any material/data adopted from other sources to make this research work more comprehensive is clearly referenced.

1.3 Aim and Objectives

The aim of the present research is to introduce a wavelength diversity technique in BOTDR system in order to enhance the sensing performance. The innovative wavelength diversity BOTDR system is expected to be effectively applied for structural health monitoring applications, particularly rail-track condition monitoring.

The key objectives of this research include:

1. To design and investigate a novel BOTDR and BOTDA system performance and address the major noise sources and its limitations.
2. Propose and design the optimisation techniques, such as employing a balanced photodetector, reference Brillouin ring laser for cost-effective receiver bandwidth reduction, and employing an inline EDFA for sensing range improvement.

3. Propose an innovative wavelength diversity technique in order to improve the SNR of the BOTDR system, thus improving the sensing performance.
4. Experimental investigation of proposed wavelength diversity BOTDR combined with a simple, low-cost passive depolarizer to suppress the polarization noise.
5. Design and implementation of integrating the long-term evolution (LTE) radio-over-fibre (RoF) data system and BOTDR sensing system using a single optical fibre.

1.4 Original Contributions

This thesis introduces a number of original contributions to the knowledge that are summarised as follows:

- A detailed investigation of the BOTDR and BOTDA sensing system is carried out. The input pump power limitation and main noise sources are carefully identified in order to achieve better sensing performance. In this regard, a wavelength diversity technique is proposed in BOTDR system to overcome the input pump power limitation due to the nonlinear effects. As a result, the SNR is improved and higher measurement accuracy for strain and temperature is achieved. We developed an SNR equation for the proposed wavelength diversity BOTDR. These results have been published in [C4], [C6] [C7] and [C8].
- In order to detect the weak Brillouin signal at the receiver, a balanced photodetector is employed and demonstrated. Thereafter, for improving the sensing range, an inline erbium-doped fibre amplifier (EDFA) is used in BOTDR system at a certain distance to amplify the attenuated pulse without scarifying the spatial resolution. The proof-of-concept has been demonstrated with an improved sensing range of 50 km and 5 m spatial resolution. The results have been published in [C1].

- Considering the complexity and expensive methods required for polarization noise suppression in BOTDR system, a simple, low-cost passive depolarizer is adopted in proposed wavelength diversity BOTDR. In Chapter 6, the proposed system proof-of-concept is demonstrated using a 25 km sensing fibre with 5 m spatial resolution. The results demonstrate an SNR improvement of 4.85 dB, which corresponds to 174% improvement compared to a conventional BOTDR system. The results have been published in [C2], [C3] and [J2].
- As a solution to overcome the complexity of the receiver bandwidth reduction, a reference Brillouin ring laser is used in a proposed wavelength diversity BOTDR system with a passive depolarizer. The proposed system validated over a 50 km sensing fibre with a 5 m spatial resolution. At a 50 km fibre distance, the improved SNR is 5.1 dB and the strain and temperature measurement accuracies were ±10με and ±0.48^{o}C, respectively. These results have been published in [J1].
- In Chapter 7, we proposed and investigated the simultaneous integration of LTE-RoF data transmission system and BOTDR sensing system over a single optical fibre. The error vector magnitude (EVM) is analysed for three modulation formats of quadrature phase-shift keying (QPSK), 16-quadrature amplitude modulation (16-QAM) and 64-QAM in the presence of various BOTDR input pump powers. The temperature effects on EVM performance (0.024±0.0025%/^{o}C) and Brillouin gain spectrum (1.07±0.013 MHz/^{o}C) has been investigated simultaneously using a 25 km single-mode silica fibre. Finally, the sensing performance and spatial resolution in the presence of active data transmission has been investigated. For this purpose, the temperatures have been applied on a 20 m fibre at end of the sensing fibre. These output results have been submitted to [J3].

The overall contribution of this research is graphically illustrated with a research road map and shown in Figure 1.2.

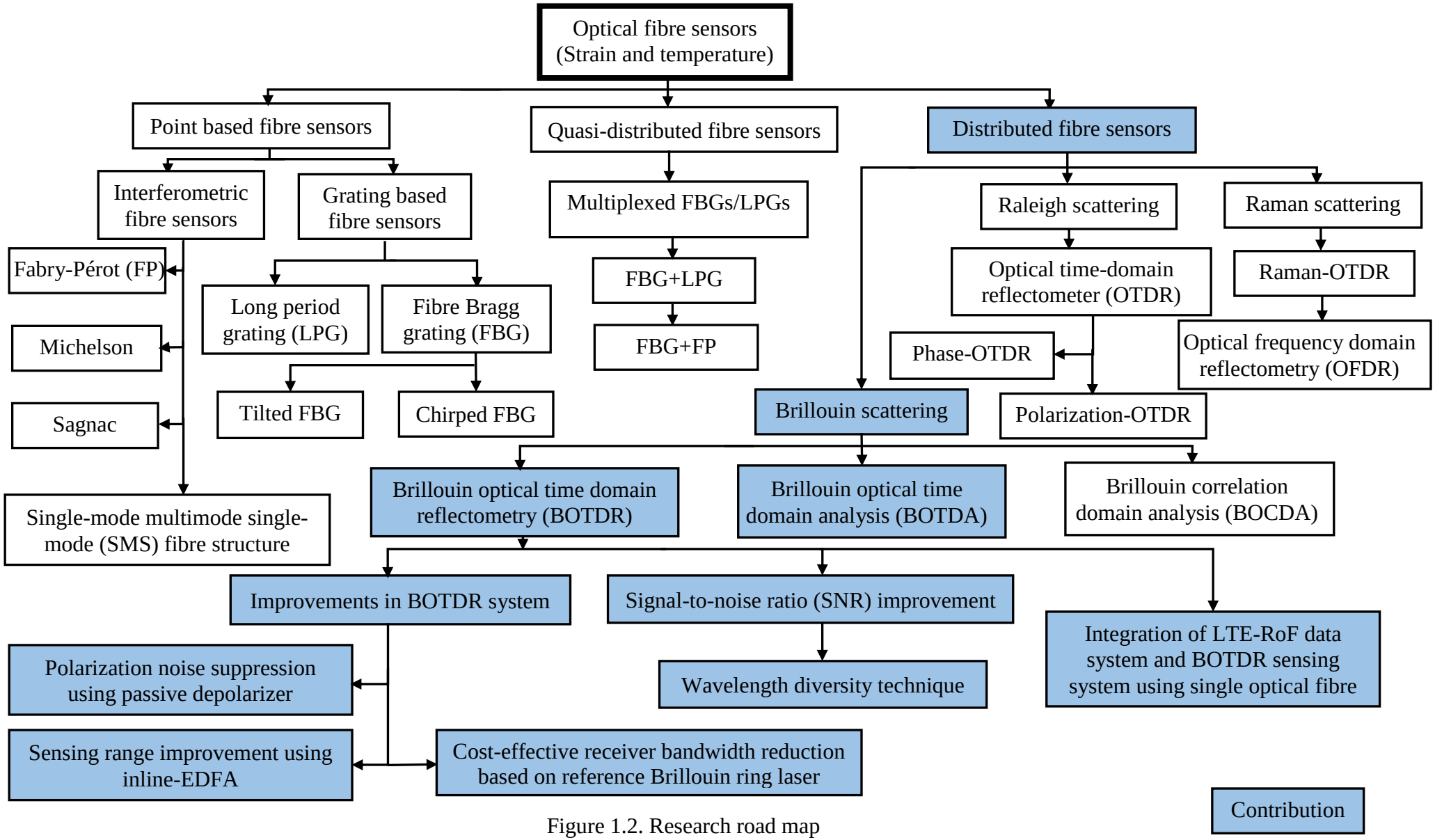

Figure 1.2. Research road map

1.5 Publications and Awards

The outcomes of the research that are published and under review in journals and conferences are enlisted below:

1.5.1 Journals

[J1]. N. Lalam, W. P. Ng, X. Dai, Q. Wu and Y. Q. Fu, "Performance Improvement of Brillouin Ring Laser based BOTDR System Employing a Wavelength Diversity Technique," *IEEE/OSA Journal of Lightwave Technology*, vol. 36, pp. 1084-1090, 2017. (DOI: 10.1109/JLT.2017.2766765).

[J2]. N. Lalam, W. P. Ng, X. Dai, Q. Wu and Y. Q. Fu, "Performance analysis of Brillouin optical time domain reflectometry (BOTDR) employing wavelength diversity and passive depolarizer techniques," *Measurement Science and Technology*, vol. 29, p. 25101, 2018. (DOI: 10.1088/1361-6501/aa9c6e).

[J3]. N. Lalam, W. P. Ng, X. Dai, Q. Wu, and Y. Q. Fu, "Integration of LTE-RoF data system and Brillouin based distributed sensing system using a single optical fibre," *IEEE/OSA Journal of Lightwave Technology*, 2018 (under review).

[J4]. N. Lalam, W. P. Ng, X. Dai, Q. Wu, and Y. Q. Fu, "Theoretical and experimental modelling of measurement uncertainty factors for Brillouin optical time-domain reflectometry (BOTDR)," *IEEE Sensors Letters*, 2018 (under review).

[J5]. G. Zhou, Q. Wu, R. Kumar, W. P. Ng, H. Liu, N. Lalam, X. Yuan, Y. Semenova, G. Farrell, J. Yuan, C. Yu, J. Zeng, G. Y. Tian and Y. Q. Fu, "High Sensitivity Refractometer Based on Reflective SMF-Small Diameter No Core Fibre Structure," *Sensors*, vol. 17, p. 1415, 2017. (DOI: 10.3390/s17061415).

1.5.2 Conferences

[C1]. T. Chen, X. Xu, N. Lalam, W. P. Ng, "Multi Point Strain and Temperature Sensing Based on Brillouin Optical Time Domain Reflectometry," in *2016 11th*

International Symposium on Communication Systems, Networks and Digital Signal Processing (*CSNDSP*), Bugapest, Hungary, 2018 (Accepted).

[C2]. N. Lalam, W. P. Ng, X. Dai, Q. Wu, and Y. Q. Fu, " Sensing Range Improvement of Brillouin Optical Time Domain Reflectometry (BOTDR) using inline Erbium-Doped Fibre Amplifier," *2017 IEEE Sensors*, Glasgow, 2017, pp. 1-3. (DOI: 10.1109/ICSENS.2017.8233878).

[C3]. W. P. Ng and N. Lalam, " Performance improvement of Brillouin based distributed fibre sensors employing wavelength diversity techniques (Invited Paper)," in *16th International Conference on Optical Communications and Networks* (*ICOCN*), Wuzhen, China, 2017, pp. 1-3. (DOI: 10.1109/ICOCN.2017.8121531).

[C4]. N. Lalam, W. P. Ng, X. Dai, Q. Wu, and Y. Q. Fu, "Performance improvement of BOTDR system using wavelength diversity technique," in *25th International Conference on Optical Fibre Sensors* (*OFS*), Jeju, South Korea, 2017, pp. 1032366-1032366-4. (DOI: 10.1117/12.2263294).

[C5]. W. P. Ng and N. Lalam, "Future of distributed fibre sensors (Invited Paper)," in *15th International Conference on Optical Communications and Networks* (*ICOCN*), Hangzhou, China, 2016, pp. 1-3. (DOI: 10.1109/ICOCN.2016.7932343).

[C6]. N. Lalam, W. P. Ng, Q. Wu, X. Dai, and Y. Q. Fu, "Perfluorinated polymer optical fibre for precision strain sensing based on novel SMS fibre structure," in *2016 10th International Symposium on Communication Systems, Networks and Digital Signal Processing* (*CSNDSP*), Prague, Czech Republic, 2016, pp. 1-3. **(**DOI: 10.1109/CSNDSP.2016.7573938).

[C7]. N. Lalam, W. P. Ng, X. Dai, Q. Wu, and Y. Q. Fu, "Analysis of Brillouin Frequency Shift in Distributed Optical Fibre Sensor System for Strain and

Temperature Monitoring," in *Proceedings of the 4th International Conference on Photonics, Optics and Laser Technology* (*PHOTOPTICS*), Rome, Italy, 2016, pp. 335-342**. (**INSPEC Accession Number: 16968590).

[C8]. N. Lalam, W. P. Ng, and X. Dai, "Employing wavelength diversity technique to enhance the Brillouin gain response in BOTDA system," in *Optical Fibre Communication Conference* (*OFC*), Anaheim, California, 2016, p. M2D.4. (DOI: org/10.1364/OFC.2016.M2D.4).

[C9]. N. Lalam, W. P. Ng, X. Dai, and H. K. Al-Musawi, "Characterization of Brillouin frequency shift in Brillouin Optical Time Domain Analysis (BOTDA)," in *20th European Conference on Networks and Optical Communications* (*NOC*), London, 2015, pp. 1-4. (DOI: 10.1109/NOC.2015.7238625).

[C10]. H. K. Al-Musawi, W. P. Ng, Z. Ghassemlooy, C. Lu, and N. Lalam, "Experimental analysis of EVM and BER for indoor radio-over-fibre networks using polymer optical fibre," in *20th European Conference on Networks and Optical Communications* (*NOC*), London, 2015, pp. 11-16. (DOI: 10.1109/NOC.2015.7238624).

1.5.3 Awards

1. Northumbria University studentship (2014-2017).
2. Northumbria LED teaching award in the category of "Best postgraduate student who teaches", 2017.
3. UK Science and Innovation travel grant for "UK-UAE Science Collaboration Symposium on Future Smart Cities", Abu Dhabi, United Arab Emirates, March 2017.
4. British Council travel grant for "British Council-International Workshop on Seismic Risk Assessment and Mitigation Strategies for Existing Buildings and Structures", Mexico City, Mexico, October 2016.

5. British Council travel grant for “Knowledge Exchange Research Conference on Remote Condition Monitoring (RCM) on Railway”, Istanbul, Turkey, March 2016.

1.6 Thesis Organization

This thesis is mainly focused on the research work dedicated to the BOTDR system performance improvement and simultaneous integration of LTE-RoF data system and BOTDR sensing system using a single optical fibre. The organization of this thesis includes literature reviews, original contributions, conclusions and future work divided into 8 Chapters.

After a brief introduction including a statement of the problem, aims and objectives, original contributions and research outcomes, **Chapter 2** introduces the light scattering properties of the optical fibre. The three scattering effects, Raleigh, Raman and Brillouin scattering are discussed. This includes a theoretical model for both linear and nonlinear scattering effects with a special focus on Brillouin scattering.

Chapter 3 provides the literature review on distributed fibre sensors with a special emphasis given to Brillouin based distributed fibre sensors. The various applications of distributed fibre sensors and operating principles are discussed and the well-known techniques summarized up to date. **Chapter 4** focuses on the investigations of the conventional BOTDR and BOTDA systems. The main devices such as distributed-feedback (DFB) laser and Mach-Zehnder modulator (MZM) have been characterized to better understand the individual device performance. The major noise sources and performance limitations of the BOTDR system are discussed. A simple, low-cost passive depolarizer is adopted to reduce the polarization noise and experimentally investigated including theoretical study. Furthermore, the different key factor effects on BOTDR system performance, such as a number of trace averages, Brillouin linewidth and sweep frequency step is evaluated experimentally and compared with the theoretical analysis.

Chapter 5 describes the few improvement techniques for BOTDR system such as (i) employing a balanced photodetector (ii) inline EDFA and (iii) reference Brillouin ring laser. The balanced photodetector, which consists of two well-matched photodiodes, which significantly improves the receiver sensitivity. An inline EDFA is employed at a certain distance to amplify the attenuated pulse and increase the sensing range. Whereas, the cost-effective reference Brillouin ring laser is used for the receiver bandwidth reduction in the order of few MHz.

Chapter 6 is dedicated to the investigation of the proposed wavelength diversity BOTDR system, in order to overcome the input pump power limitation due to the nonlinear effects and therefore improve the SNR significantly. In addition, the proposed wavelength diversity BOTDR is combined with a Brillouin ring laser and a passive depolarizer for further improvement.

Chapter 7 introduces and demonstrates the simultaneous integration of LTE-RoF data transmission system and BOTDR sensing system over a single optical fibre. The LTE-RoF data system is composed of three modulation formats of QPSK, 16-QAM and 64-QAM, which is modulated using orthogonal frequency division multiplexing (OFDM). While, the distributed sensing system utilizes a BOTDR with a 5 m spatial resolution and 25 km single-mode silica fibre.

Finally, **Chapter 8** concludes this thesis by summarising all the research findings with some recommendations for future works that could bring the proposed wavelength diversity BOTDR system and integrated LTE-RoF data and BOTDR system to the next level.

Chapter 2
Light Scattering in Optical Fibre

2.1 Introduction

In general, the optical fibre core material is not completely homogeneous throughout the fibre length. When a light wave propagates along the fibre, a part of the light experiences the scattering effect due to core density fluctuations, impurities, thermal and acoustic vibrations. Therefore, the scattering effect is always present in optical fibres since no fibre is free from microscopic defects. The light scattering can be classified into two types (i) linear scattering and (ii) nonlinear scattering. The linear scattering refers to the case where the incident electric field does not modify the optical medium properties, which is the case when the input power below a certain nonlinear threshold level. Whereas, the nonlinear scattering modifies the optical medium properties, which is the case when the input power is above a certain nonlinear threshold [22]. This chapter briefly discusses the light scattering types in optical fibre with a special focus on Brillouin scattering mechanism.

2.2 Linear Scattering

In an optical fibre, three different types of scattering effects, Raleigh, Raman and Brillouin can be observed in the scattered light spectrum. The scattering can be categorized into two regimes, namely elastic and inelastic.

- **Elastic scattering**: the scattered photons maintain their energy; hence no frequency shift is observed corresponds to the input signal frequency.

- **Inelastic scattering:** the scattered photons results from the energy exchange with the material, which means photons lose/gain energy and undergo a frequency shift corresponds to the input signal frequency [23]. The spontaneous scattered light spectrum in a silica optical fibre at a pump wavelength of 1550 nm is illustrated in Figure **2.1** [24].

As shown in Figure **2.1**, the three scattered components, namely Rayleigh, Brillouin and Raman scattering occur in the optical fibre. The Raleigh scattering, which is an elastic scattering, originates from the non-propagating density fluctuations, hence it does not involve any frequency shift. Whereas the Brillouin and Raman, which are inelastic scattering, undergo an energy exchange between the photons and phonons within the fibre medium. If the energy transfers from input photons to phonons, the scattered photon frequency will be lower than the input photons and is denoted as Stokes scattering. On the other hand, if the energy transfers from the phonons to photons, the scattered photon frequency will be higher than the input photons and is denoted as anti-Stokes scattering. The three scattering effects are briefly discussed as follows:

- **Rayleigh scattering** occurs from the microscopic variations and unequal distribution of molecule densities over the fibre distance. The Rayleigh scattering

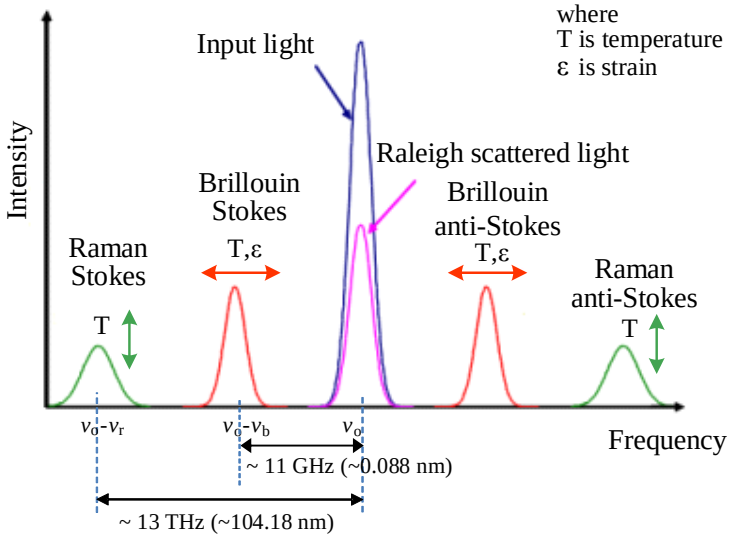

Figure 2.1. Spontaneous backscattered spectrum in silica optical fibre at a wavelength of 1550 nm

frequency is the same as the input light frequency, so-called elastic scattering. Therefore, Raleigh scattering phenomena does not have any frequency shift [25]. In 1871, the British Scientist Lord Rayleigh is firstly observed the Rayleigh scattering by the particles much smaller than the light wavelength. The Rayleigh scattering is a promising technique for the well-known device, optical time domain reflectometer (OTDR), which is used for measuring the fibre length, attenuation and damage detection over the fibre length. However, the Rayleigh scattering is not an effective mechanism to measure the strain and/or temperature.

- **Raman scattering** arises from the interaction between input light and molecular vibrations or phonons. The phonons involved in this process often called as optical phonons and generated by a thermal agitation [26]. The optical phonon vibrations are much higher than the acoustic phonons, which results in a scattered frequency shift of ~13 THz for a silica fibre. The scattered magnitude is ~30 dB weaker than the Rayleigh scattering. Raman scattering has a frequency shift from the input light, so-called inelastic scattering. The Raman scattering intensity linearly changes with the temperature, where the population density of the energy levels governed by the optical phonon distribution [6]. In contrast to Rayleigh scattering, the Raman scattering can be used for distributed temperature measurement.
- **Brillouin scattering** arises from the interaction of light with propagation density fluctuations or acoustic phonons. The interaction of input photons and acoustic phonons results in a frequency shift of Brillouin scattering, which depends on the acoustic velocity of the medium. The Brillouin scattering frequency shift is on the GHz scale (~11 GHz) [25]. In 1920, the French physicist Leon Brillouin investigated the light scattering at acoustic waves, this effect was named after him. In contrary to the Raman scattering, there are no vibrational modes of the

Table 2.1. Key parameters of spontaneous backscattered spectrum for silica fibre at 1550 nm [25, 27-29]

Parameter	**Brillouin**	**Raman**	**Rayleigh**
Frequency shift	~10-12 GHz	~13 THz	0
Spectral linewidth	~20-100 MHz	~5 THz	-
Scattered power weaker than Raleigh	~15 dB	~30 dB	-
Gain coefficient	$\sim 5\times10^{-11}$ m/W	7×10^{-14} m/W	
Measurable physical quantities	Strain and temperature	Temperature	Fibre loss (vibration)
Measurement target	Frequency and intensity	Intensity	Intensity (Phase)
Peak power change with temperature	~0.30%/^{o}C	~0.80%/^{o}C	-
Peak frequency change with temperature	~1.1 MHz/^{o}C	-	-
Peak power change with strain	$\sim -9\times10^{-4}$%/με	-	-
Peak frequency change with strain	~0.048 MHz/με	-	-

molecules but the density fluctuations of the medium is responsible for the Brillouin scattering effect.

Table **2.1** summarizes the key parameters of the spontaneous scattering of silica fibre at 1550 nm pump wavelength. For silica based fibres, the Brillouin frequency shift is in the order of 10-12 GHz (depending on the material doping concentration) and the Brillouin linewidth at full width at half maximum (FWHM) of typically 20-100 MHz, which is determined by the short acoustic phonon lifetime of ~10 ns. Whereas, the Raman scattering experiences a huge frequency shift of ~13 THz and linewidth of ~5 THz.

2.2.1 Theoretical Model of Spontaneous Brillouin Scattering

Brillouin scattering originates from the acoustic phonons in contrast to the Raman scattering which originates from optical phonons. The acoustic vibrations are present

everywhere within the optical medium. The phonon population distribution follows a Bose-Einstein distribution law [30],

$$N_{phonons} = \frac{1}{2} + \frac{1}{\left[\exp\left(\frac{hf}{kT}\right)\right] - 1} \tag{2.1}$$

where f is the phonon frequency, h is the Planck's constant, k is the Boltzmann constant and T is the temperature in Kelvin. The acoustic phonons can be expressed as density fluctuations which originate from the two independent thermodynamic variables, such as the pressure p and entropy S, and it can be expressed as [22],

$$\Delta\rho = \left(\frac{\partial\rho}{\partial p}\right)_s \Delta p + \left(\frac{\partial\rho}{\partial s}\right)_p \Delta s \tag{2.2}$$

where ρ is the material density. The first term on the right-hand side of the above equation (2.2) is due to the acoustic vibrations (adiabatic density fluctuations) and describe the spontaneous Brillouin scattering. The second term originates from the isobaric density fluctuations (entropy fluctuations) and gives rise to Rayleigh scattering. The entropy fluctuations are frozen in the medium, therefore, the photons are elastically scattered in Rayleigh scattering. Whereas, the Brillouin scattering is due to the interaction of optical waves and propagating acoustic vibrations. Hence, the Brillouin scattered photons have a frequency shift corresponds to the input pump signal frequency. The change of the material density in equation (2.2) includes a variation of the dielectric permittivity constant, $\in$ and it can be expressed as [31],

$$\Delta\in = \left(\frac{\partial\in}{\partial\rho}\right)_T \Delta\rho + \left(\frac{\partial\in}{\partial T}\right)_\rho \Delta T \tag{2.3}$$

The second term in the above equation (2.3) is considered negligible, as the density fluctuation influences are stronger than the temperature variations. Substituting the first term of equation (2.2), which is crucial for Brillouin scattering into the equation (2.3) and yields to,

$$\Delta \in = \left(\frac{\partial \in}{\partial \rho}\right)_T \left(\frac{\partial \rho}{\partial p}\right)_s \Delta p = \frac{\gamma_e}{\rho_o}\left(\frac{\partial \rho}{\partial p}\right)_s \Delta p \tag{2.4}$$

where the electrostrictive coefficient γ_e is assumed as,

$$\gamma_e = \rho_o \left(\frac{\partial \in}{\partial \rho}\right)_T \tag{2.5}$$

where ρ_o is the mean material density. The induced polarization, $\mathbf{P}$ for a dielectric material that is exposed to an electric field, E can be expressed as [32],

$$\mathbf{P} = \in_o \chi^{(1)} \mathbf{E} \tag{2.6}$$

where $\chi^{(1)}$ is the first order (linear) dielectric susceptibility, $\in_o$ is the vacuum dielectric permittivity. By the help of equation (2.4), one can calculate an additional contribution $\left(\mathbf{P}_{\text{add}}\right)$ to the polarization according to equation (2.6) [33],

$$\mathbf{P} = \in_o \chi^{(1)}.\mathbf{E} + \Delta \in .\mathbf{E} = \in_o \chi^{(1)}.\mathbf{E} + \mathbf{P}_{\text{add}} \tag{2.7}$$

where $\mathbf{P}_{\text{add}} = \Delta \in .\mathbf{E},$ is the additional polarization contribution. Substituting equation (2.4) into $\mathbf{P}_{\text{add}}$, we can get,

$$\mathbf{P}_{\text{add}} = \frac{\gamma_e}{\rho_o}\left(\frac{\partial \rho}{\partial p}\right)_s \Delta p.\mathbf{E} = \frac{\gamma_e}{\rho_o}\Delta \rho.\mathbf{E} \tag{2.8}$$

Any pressure wave p gives rise to material density change $(\Delta\rho)$, which obeys the wave propagation equation[1] [33],

$$\frac{\partial^2\rho}{\partial t^2}-\Gamma_B\nabla^2\frac{\partial\rho}{\partial t}-v_a^2\nabla^2\rho=0 \tag{2.9}$$

where v_a is the acoustic velocity, Γ_B is the acoustic damping coefficient, which describes the sound attenuation in the medium.

If the acoustic wave assumed as a monochromatic temporal behaviour, then the related density wave changes in the form of,

$$\Delta\rho=\frac{1}{2}\left[\mathrm{A}(z,t)e^{j(\omega_B t-k_B r)}+\mathrm{A}^*(z,t)e^{-j(\omega_B t-k_B r)}\right] \tag{2.10}$$

where A is the peak amplitude at fibre distance z and at a given point in time t, ω_B and k_B are the angular frequency and wave vector of the acoustic wave, respectively. In the same approach, the optical waves have to fulfil the optical wave equation [30]

$$\frac{\partial^2}{\partial z^2}\mathbf{E}-\frac{n^2}{c^2}\frac{\partial^2}{\partial t^2}\mathbf{E}=\mu_o\frac{\partial^2}{\partial t^2}\mathbf{P}_{\text{add}} \tag{2.11}$$

The monochromatic pump wave propagating along the fibre distance *z*, the associated electric field is expressed as [22],

$$\mathbf{E}(r,t)=e_p\frac{1}{2}\left[\mathrm{E}_p(z,t)e^{j(\omega_p t-k_p r)}+\mathrm{E}_p^*(z,t)e^{-j(\omega_p t-k_p r)}\right] \tag{2.12}$$

where ω_p is the angular frequency, k_p is the wave vector and e_p is the unitary vector of the polarization state of the input pump wave. In equation (2.12), the electric field distribution over the fibre distance is neglected, therefore, the plane wave expression is considered.

[1] This equation, which is well known in the field of acoustics, it can be easily derived from the Navier-Stokes equations for the case of a viscous and compressible fluid [34].

Bringing acoustics and optical waves together, replacing equations (2.10) and (2.12) into equation (2.11) and utilizing the equation (2.5) one can obtain [35],

$$\frac{\partial^2}{\partial z^2}\mathbf{E}-\frac{n^2}{c^2}\frac{\partial^2}{\partial t^2}\mathbf{E} \;=\; e_p\,\frac{\gamma_e}{4\rho_o}\Big[\left(\omega_p+\omega_B\right)^2 \mathrm{AE}_p e^{j\left(\omega_p+\omega_B\right)t-\left(k_p+k_B\right)r}+ \left(\omega_p-\omega_B\right)^2 \mathrm{A}^{*}\mathrm{E}_p e^{j\left(\omega_p-\omega_B\right)t-\left(k_p-k_B\right)r}\Big]+c.\,c \tag{2.13}$$

where $c.\,c$ is the complex conjugate. From the above equation, two spectral components are described the Stokes wave at a lower frequency $\omega_p-\omega_B$ and anti-Stokes wave at a higher frequency $\omega_p+\omega_B$ [25].

The spontaneous Brillouin scattering is classically described as an interaction between the input pump wave and the acoustic wave as a Bragg diffraction. The pump wave generates an acoustic wave through the process of electrostriction [36]. The acoustic wave modulates the material density, which induces a modulation of dielectric permittivity and can generate a periodic structure similar to Bragg Grating. The light wave scattered back by this moving diffraction grating and undergoes a frequency shift due to Doppler Effect [37]. The energy and momentum conservation for the Stokes wave is given by,

$$\omega_p=\omega_s+\omega_B \tag{2.14}$$

$$k_p=k_s+k_B \tag{2.15}$$

where ω_p, ω_s, ω_B are angular frequencies of input pump wave, Stokes wave and acoustic wave, respectively. The k_p, k_s, k_B are the wave vectors of pump wave, Stokes wave and acoustic wave, respectively. The respective wavelengths can be obtained as,

$$\left|k_p\right|=\frac{2\pi n}{\lambda_p},\qquad \left|k_s\right|=\frac{2\pi n}{\lambda_s},\quad \text{and}\qquad \left|k_B\right|=\frac{2\pi}{\lambda_B}=\frac{\omega_B}{v_a} \tag{2.16}$$

As shown in Figure **2.2**, the conservation of momentum with an angle θ between the pump and Stokes wave can be written as,

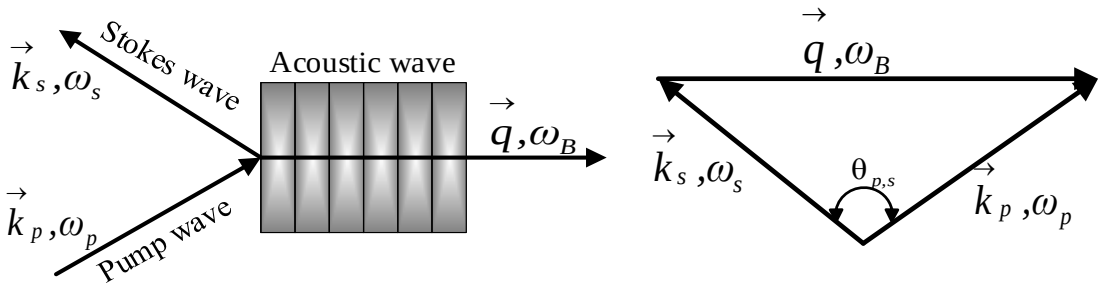

Figure 2.2. Stokes process of spontaneous Brillouin scattering in Bragg diffraction regime

$$|q| = |k_p| + |k_s| - 2|k_p||k_s|\cos(\theta_{p,s}) \tag{2.17}$$

where $\theta_{p,s}$ is the angle between the pump wave and Stokes wave as shown in Figure **2.2**. Using equation (2.16) and (2.17) as well as $|k_p| \approx |k_s|$, the angular frequency of the acoustic wave can be derived as [38],

$$\omega_B = 2v_a |k_p| \sin\left(\frac{\theta_{p,s}}{2}\right) \tag{2.18}$$

In a standard bulk medium, the scattering takes place in all the directions. In optical fibres, the scattering is essentially guided in a forward and backward direction. As per equation (2.18), the Brillouin frequency shift in forward direction (θ=0) vanishes, whereas, in the backward direction, θ=180 is at maximum. Therefore, the maximum Brillouin frequency shift v_B is calculated using a relation from the equation (2.16) $|k_p| = 2\pi n / \lambda_p$ as,

$$v_B = \frac{\omega_B}{2\pi} = \frac{2nv_a}{\lambda_p} \tag{2.19}$$

Using typical values of silica fibre, such as n =1.45, v_a =5960 m/s and λ_p =1550 nm, the Brillouin frequency shift v_B approximately ~11 GHz. The Stokes wave has the frequency

of $\nu_p - \nu_B$ and the Anti-stokes frequency is $\nu_p + \nu_B$. As mentioned earlier, the backward Brillouin scattering originates from the interaction of input pump wave and longitudinal acoustic waves. The equation (2.18) predicts that the Brillouin scattering occurs in only in backward direction. However, a small amount of Stokes light is guided towards a forward direction (parallel to the pump propagation), as the acoustic wave consists transverse wave nature [39]. This forward Brillouin scattering is called guided acoustic wave Brillouin scattering (GAWBS) [40]. However, the GAWBS phenomena, the scattered light is extremely weak and will not be considered further in this thesis.

2.2.2 Brillouin Linewidth

The Brillouin linewidth, $\Delta\nu_B$ is referred to as the linewidth (full width at half maximum (FWHM)) of the Brillouin gain spectrum when a monochromatic pump wave is used. The Brillouin linewidth depends on the acoustic wave damping coefficient, Γ_B . For the shorter acoustic lifetime, the linewidth will be larger, whereas, for the longer acoustic lifetime, the linewidth will be smaller.

The acoustic wave damping time or phonon lifetime, τ_a is inversely proportional to the damping coefficient, Γ_B and denotes the average acoustic phonon lifetime. The typical acoustic phonon lifetime for silica-based fibre is approximately ~10 ns [41]. The phonon lifetime highly depends on the acoustic wave frequency at a given pump wavelength. The Brillouin linewidth, $\Delta\nu_B$ can be expressed as [22],

$$\Delta\nu_B = \frac{\Gamma_B}{\pi} = \frac{1}{\pi\tau_a} \tag{2.20}$$

The further discussions of the relation between the Brillouin linewidth and acoustic lifetime can found in [42]. For a continuous wave pump source, the Brillouin gain spectrum has a Lorentzian shape and can be expressed as [43],

Table 2.2. Values to calculate the Brillouin gain coefficient for silica fibre

Parameter	**Symbol**	**Value**
Refractive index	n	1.45 [44]
Photo-elastic coefficient	p_{12}	0.29 [45]
Polarization factor (for standard single mode fibre)	γ_p	0.5 [46]
Light velocity	c	2×10^8 m/s
Pump wavelength	λ_p	1550 nm
Material density	ρ	2,200 kg/m^3 [47]
Acoustic velocity	v_a	5,960 m/s [47]
Brillouin linewidth (FWHM)	$\Delta\nu_B$	30 MHz

$$g(\nu) = g_B \frac{\left(\Delta\nu_B/2\right)^2}{\left(\nu-\nu_B\right)^2+\left(\Delta\nu_B/2\right)^2} \tag{2.21}$$

where g_B is Brillouin gain coefficient, $\Delta\nu_B$ is Brillouin linewidth at FWHM, ν_B is the Brillouin frequency shift. Furthermore, the Brillouin gain coefficient, g_B can be expressed as [46],

$$g_B = \frac{2\pi n^2 p_{12}^2 \gamma_p}{c\lambda_p^2 \rho v_a \Delta\nu_B} \tag{2.22}$$

where n is the refractive index, p_{12} is the photo-elastic coefficient of the silica fibre, γ_p is polarization factor, λ_p is the pump wavelength, ρ is the material density of the silica, v_a is the acoustic velocity and $\Delta\nu_B$ is the Brillouin linewidth at FWHM. The Brillouin gain coefficient gives the fractional increase in signal intensity per unit length, therefore it has the unit of m/W. Considering the values defined in Table 2.2, and using equation (2.22), the obtained Brillouin gain coefficient is, $g_B \approx 5\times10^{-11}$ m/W.

2.2.3 Spontaneous Raman Scattering

The Raman scattering was first discovered by an Indian scientist C. V. Raman in liquids and awarded a Noble Prize for Physics in 1930 [48]. Raman backscattering is an inelastic scattering, as the input pump signal transfers some of the photons to new frequencies [22]. The higher frequency optical phonons are present within the medium as vibrational modes. Therefore, the Raman frequency shift is much higher as ~ 13 THz from the input pump signal frequency. Moreover, the linewidth at FWHM of spontaneous Raman scattering is approximately ~5 THz and the optical phonon decay time is 150 fs. Figure **2.3** illustrates the process of Raleigh and Raman scattering in a silica fibre. In this process, the input photons at a frequency of hv_p (where h is a Plank's constant) undergoes an energy change either losing or gaining energy, therefore the Raman Stokes $(hv_p - hv_1)$ and anti-Stokes $(hv_p + hv_1)$ are generated respectively.

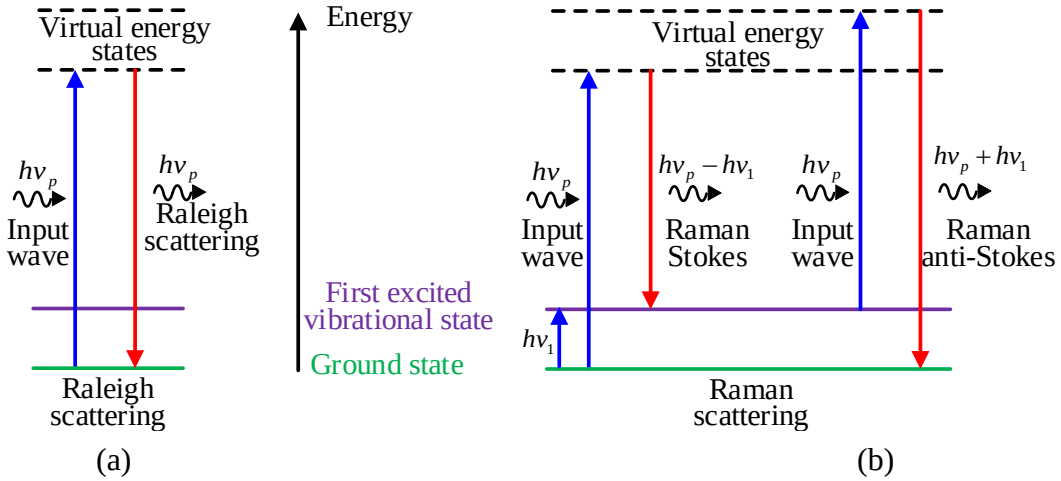

Figure 2.3. Diagram of molecular vibration energy levels for (a) Raleigh scattering (b) Raman Stokes and anti-Stokes scattering

2.3 Nonlinear Scattering

In contrast to linear or spontaneous scattering, nonlinear scattering modifies the material optical properties. There are two different nonlinear scattering effects in optical fibres, namely stimulated Brillouin scattering (SBS) and stimulated Raman scattering (SRS). The both SBS and SRS are inelastic scattering process associated with the vibrational excitation modes of the fibre [49]. At a sufficiently high input pump power the nonlinear scattering effect is observed. The following sections discuss the SBS and SRS and their threshold power with theoretical description.

2.3.1 Stimulated Brillouin Scattering

The spontaneous Brillouin scattering results from the interaction of input pump light with acoustic phonons and associated Doppler shift, while the acoustic phonon population is described by the Bose-Einstein law equation [50]. In this interaction either a phonon is created (anti-Stokes process) or annihilated (Stokes process) [51]. At a certain larger pump intensity, the spontaneous Brillouin scattering becomes a nonlinear process. The large intensity produces a fibre core compression through electrostriction process. The electrostriction phenomena produce much higher density fluctuations within the fibre material medium. Gradually, it increases the material disorder, which turns to modulate the linear refractive index to nonlinear medium, which is called electrostrictive nonlinearity [52]. If the input pump power is sufficiently high enough to generate SBS, then most of the power backscatter and pump power depletes rapidly.

2.3.1.1 Brillouin Threshold Power

Taking into consideration of the input pump wave and Stokes wave; the initial growth of Stokes intensity under the continuous wave can be written as [25],

$$\frac{dI_s}{dz} = g_B I_p I_s \tag{2.23}$$

where g_B is Brillouin gain coefficient (described in equation (2.22)), I_p and I_s are the intensities of pump and Stokes wave, respectively. Considering the fibre losses at Stokes frequency and counter-propagating nature of the Stokes wave, the equation (2.23) can be expressed as [25],

$$\frac{dI_s}{dz} = -g_B I_p I_s + \alpha_s I_s \tag{2.24}$$

Furthermore, the pump wave coupled equation can be written as,

$$\frac{dI_p}{dz} = -\frac{\omega_p}{\omega_s} g_B I_p I_s - \alpha_p I_p \tag{2.25}$$

where α_p is the fibre loss at the input pump frequency. For simplicity, we may consider $\omega_p \approx \omega_s$ and hence $\alpha_p \approx \alpha_s \equiv \alpha$ because of small Brillouin frequency shift from the input pump frequency. Now the coupled equations (2.24) and (2.25) can be expressed as,

$$\frac{dI_s}{dz} = -g_B I_p I_s + \alpha I_s \tag{2.26}$$

$$\frac{dI_p}{dz} = -g_B I_p I_s - \alpha I_p \tag{2.27}$$

The threshold power is described as, the maximum input pump power level at which the nonlinear effect starts. The threshold level is reached when the backscattered Stokes power equals the fibre output power [53].

In the case where the Stokes power is much smaller than the input pump power we may assume that the pump power is not depleted and thus the term $-g_B I_p I_s$ in equation (2.27) can be neglected and the resultant equation can be written as,

$$\frac{dI_p}{dz} = -\alpha I_p \tag{2.28}$$

The solution of the above equation (2.28) can be written as [54],

$$I_p(z) = I_p e^{-\alpha z} \tag{2.29}$$

where $I_p(z)$ and I_p are the pump intensity at fibre distance z and the input pump intensity, respectively. Using equations (2.26) and (2.29), we can have,

$$\frac{dI_s}{dz} = -g_B I_p e^{(-\alpha z)I_s} + \alpha I_s \tag{2.30}$$

The solution of above equation (2.30) can be written as [54],

$$I_s = I_s(L) e^{\left(g_B I_p L_{eff} - \alpha L\right)} \tag{2.31}$$

where L_{eff} is the effective fibre interaction length. Using equation (2.31) and (2.29), we can be written as,

$$P_s = P_s(L) e^{(-\alpha L)} e^{\frac{g_B P_p L_{eff}}{A_{eff}}} \tag{2.32}$$

and

$$P_p(L) = P_p e^{(-\alpha L)} \tag{2.33}$$

where the power is related to the intensities as, $P_s = A_{eff} I_s$ and $P_p = A_{eff} I_p$. The A_{eff} is the effective area of the fibre. The threshold power can be calculated from the equation (2.32) and (2.33), and it can be approximated as [55],

$$P_{th} \approx \frac{21 k_p A_{eff}}{g_B L_{eff}} \tag{2.34}$$

where the polarization factor k_p lies between the 1 and 2 depending on the relative polarization of the pump and Stokes wave [56]. The threshold power is just doubled if the polarization factor is equal to 2. The experimental analysis of Brillouin threshold measurement will be discussed in Chapter 4, Section 4.3.3.

2.3.2 Stimulated Raman Scattering

As mentioned earlier, the spontaneous Raman scattering originates from the interaction of input pump wave with molecular vibrations (optical phonons) of the medium. This is a weak process in comparison to Rayleigh scattering. If the input pump power is sufficiently high and the interference of pump wave and the Stokes wave is strong enough to stimulate the molecules to vibrate at Raman frequency, thus the scattering becomes a stimulated process. The critical pump power (threshold power) of stimulated Raman scattering (SRS) can be expressed as [31],

$$P_{th}^{SRS} \approx \frac{19A_{eff}}{g_R L_{eff}} \tag{2.35}$$

where g_R is the Raman gain coefficient, which is approximately, $g_R \approx 7\times10^{-14}$ m/W for single-mode silica fibre at 1550 nm pump wavelength [55]. The threshold power for SRS is much higher than the SBS. The SRS process is exploited in several applications, such as Raman fibre lasers [57] and Raman fibre amplifier [58]. The Raman fibre amplifier is extensively investigated in Brillouin based distributed sensors to enhance the sensing range significantly [59].

2.4 Summary

This chapter was dedicated to the theoretical analysis of the light scattering in optical fibre with a special focus on Brillouin scattering. The elastic and inelastic scattering was discussed including a spontaneous backscattered spectrum in silica optical fibre, which consists of Raleigh, Raman and Brillouin scattering. The Brillouin scattering originated from the interaction of photons and acoustic phonons, while the Raman scattering is due to the interaction of the photons and optical phonons. Thereafter, the detailed explanation was given for both linear and nonlinear scattering effects. The theoretical evaluation was

given for both Brillouin and Raman threshold. From equations (2.34) and (2.35), we can predict the Brillouin and Raman threshold level, which depends on the input pump power, affective area of the fibre and fibre length. Poletti *et al*. [153] defined the Brillouin threshold power is reached when the backscattered power is 1% of the input pump power. The Brillouin frequency shift linearly changes with physical parameters such as strain and temperature, while the Raman intensity varies with only temperature. Hence the measurement in Brillouin based distributed sensors is usually focused on the frequency measurement, i.e., to measure the strain and temperature induced Brillion frequency shift change. Whereas in Raman scattering based sensors, the measurement is based on the intensity measurement over a wide frequency range (THz). Moreover, the strength of the Brillouin scattering signal is much higher than the Raman scattering, hence better sensing performance and longer sensing range over tens of kilometres can be obtained. The Brillouin based sensors have proved to be superior practically compared to the Raman based sensors. Therefore, the research work in this thesis concerned on Brillouin based sensors. Following the theoretical analysis presented in this chapter, the next chapter will focus on the literature review of distributed fibre sensors to better understand the current state of the technology.

Chapter 3
Literature Review on Distributed Fibre Sensors

3.1 Introduction

Distributed fibre sensors can be found in a wide range of structural health monitoring applications. Compared to the point based optical fibre sensors such as fibre Bragg grating (FBG) [60, 61] and long-period Grating (LPG) [62, 63] sensors, the distributed fibre sensors offers distributed measurement capability of both strain and temperature over tens of kilometres [64]. As FBG and LPG sensors are point based sensors (discrete sensors), they are good at monitoring a specific location of interest. Several FBG sensors can be multiplex together, known as quasi-distributed fibre sensor with a strain and temperature sensitivities of 1.2 pm/με and 10 pm/^{o}C, respectively [65]. The LPG sensor offers high sensitivity to temperature (0.41 nm/^{o}C) compared with the FBG sensor; however, fabrication of both the FBG and LPG sensors requires expensive equipment such as excimer laser or CO_2 laser, which results in a relatively high cost for these types of sensors. Moreover, installing and multiplexing a number of FBG/LPG sensors makes the system more complex.

In Chapter 2, the light scattering in an optical fibre has been discussed with a special emphasis on Brillouin scattering. The scattering effect is the origin for the truly distributed fibre sensors and the scattering occurs all along the fibre length. Distributed fibre sensors offer an innovative technology for a spatially distributed measurement based on Raleigh, Brillouin and Raman scattering. By analysing the backscattered signal

frequency, intensity and phase, one can realise a distributed measurement of strain, temperature and vibration over tens of kilometres. In this chapter, various applications of distributed fibre sensors are discussed. Thereafter, the commonly used distributed fibre sensors are reviewed and their operating principles are discussed. Brillouin based distributed fibre sensors, such as Brillouin optical time domain reflectometry (BOTDR), Brillouin optical time domain analysis (BOTDA) and Brillouin optical correlation domain analysis (BOCDA) systems are discussed briefly and well-known techniques and achievements in these systems are summarized.

3.1.1 Applications of Distributed Fibre Sensors

Structural health monitoring is an increasingly important tool to improve the safety and maintainability of critical structures, avoiding the risks of catastrophic failures. Therefore, the engineers worldwide are continually trying to validate structural monitoring models to reduce the tragedies caused by structural failures. The structural monitoring can be managed to reduce the economic damage and improve citizen's safety from structure failure disasters. The scheduled and periodic inspections of most infrastructures are performed by manual and visual operations or point based sensors, which are generally time-consuming and costly procedures.

Distributed fibre sensors can be found applied to a wide range of applications for structural health monitoring, chemical processing industries and communications networks. The major applications for distributed sensors are listed below.

- Oil and gas pipelines: to detect the pipeline leakage and ensure pipeline safety and integrity. Successfully deployed to monitor the downhole well performance, which results in increasing recovery and reduced cost of production [66].
- Bridges, tunnels and buildings: to monitor the high-rise buildings and bridges/tunnels in order to understand the structural behaviour over time. Concrete piles can be

permanently monitor using installed fibre optic cable on the concrete pile or inserted into the pile bore during construction [67].

- Aeroplane monitoring: Distributed fibre sensor technology has the potential for continuous monitoring of an entire aircraft structure. The potential for integrating optic fibre cable into the aeroplane structure during the manufacturing process would enable to monitoring the structure during their whole life cycle, improving their safety, reliability, cost efficiency and hence extending their operational life [68].
- Fire security: to detect the real-time temperature profile of special hazard zones and industrial plants [69].
- Ground movement monitoring: landslides, settlements, cavities, embankments, and dams in order to observe the deformations and prevent social/economic damage [70, 71].
- Communication networks: for the monitoring of defects, such as rapid strain/temperature changes along the active transmission fibre cables, strain in submarine optical cables, earthquake damage and frozen fibre cables. During the cold climate conditions, water that enters a splice enclosure can freeze, crushing the fibre strands. When ice crush occurs, an emergency network repair is needed to avoid additional damage and downtime [72].
- Rail-track monitoring: extreme strain and/or temperature of rail-track leads to buckling, fractures and even derailment. An installed optical fibre along the rail-track web can monitor the health condition of the rail-track in real-time up to several tens of kilometres.

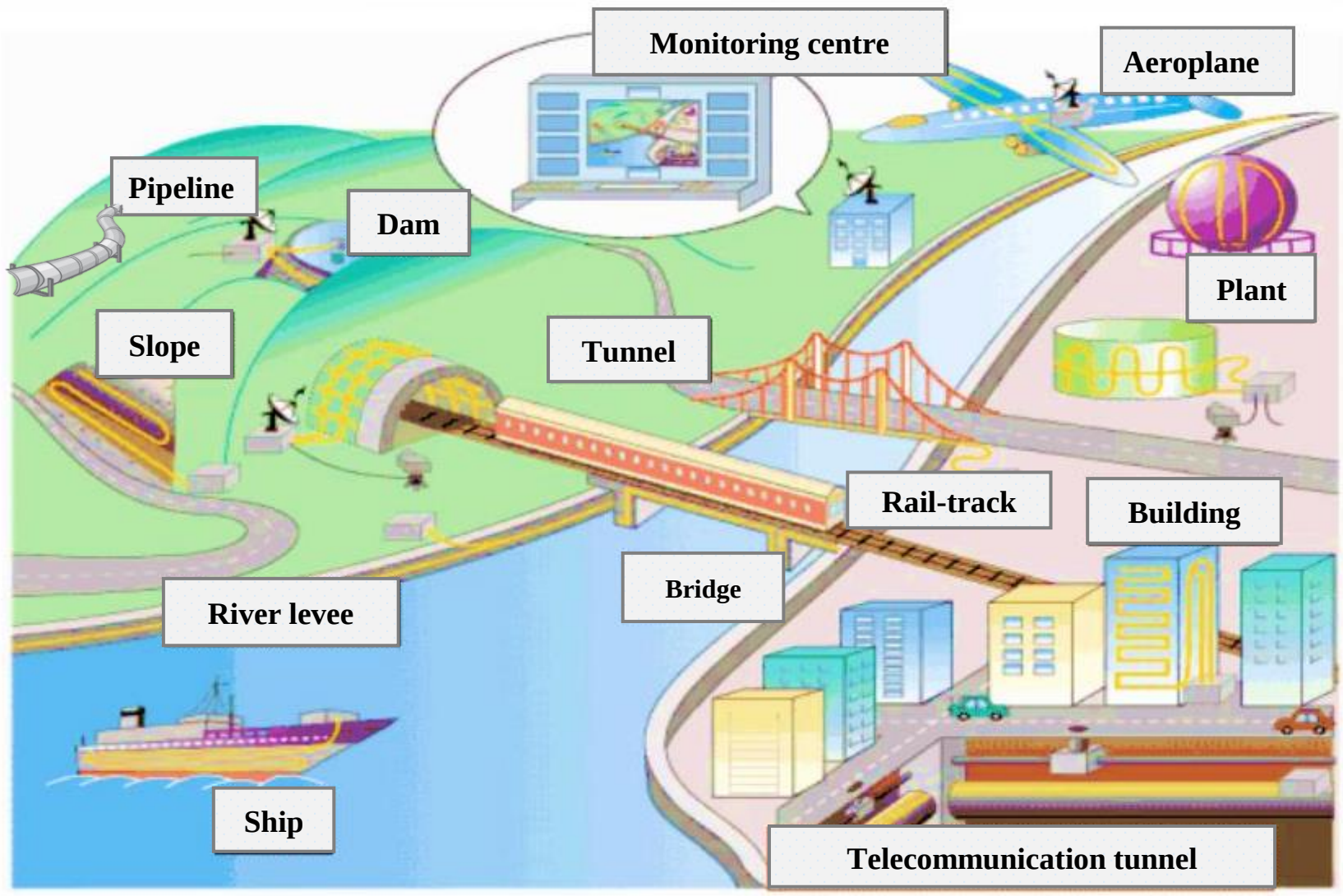

Figure 3.1. Various applications of distributed fibre sensors [1]

Figure 3.1 illustrates the various applications of distributed fibre sensors [1]. The use of distributed fibre sensors unlocks possibilities that have no equivalent in the conventional sensor systems. The various applications show that using an appropriate distributed sensor system, it is possible to obtain valuable data from large structures for the evaluation and management of the monitored structures. In the civil engineering community, structural health monitoring is a powerful tool for infrastructures management. The following sections will discuss the Raleigh, Raman, Brillouin based distributed fibre sensors with their fundamental principles.

3.2 Raleigh based Distributed Fibre Sensors

Optical time domain reflectometer (OTDR) is a widely investigated device based on Raleigh scattering for measuring loss distribution over the fibre distance. The OTDR was firstly developed by Barnoski *et al*. [74] to evaluate the fibre attenuation profile, fibre length and identify fault locations. This initial development ultimately evolved into the Brillouin and Raman based distributed fibre sensors for strain and temperature measurements. The schematic representation of an OTDR system and measured spectrum over the fibre distance is illustrated in Figure **3.2**.

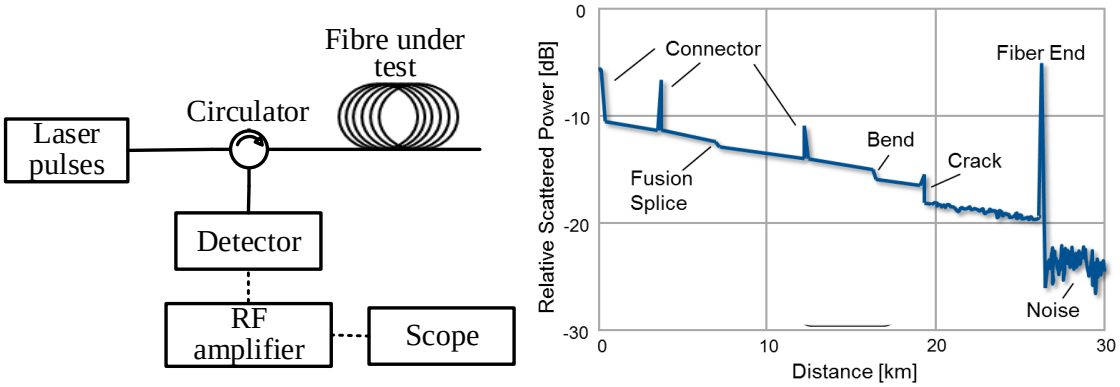

(a) (b)

Figure 3.2. (a) Schematic representation of OTDR technique (b) OTDR trace over the fibre under test [73]

In OTDR, a narrow optical pulse is launched into the fibre under test and the backscattered Raleigh signal is collected at the same end. The spatial information is measured by a classical time-of-flight method [75]. By measuring the pulse time difference between the starting and ending of the fibre, the fibre length can be estimated. Analysing the Raleigh scattered signal intensity over time (which can be related to distance along the fibre), the attention profile of the fibre, such as connector loss, splice loss, bend loss and reflections can be characterized as shown in Figure **3.2**(b).

Raleigh scattering is an elastic scattering and insensitive to strain and temperature changes. However, at least in principle, the Raleigh intensity slightly changes with temperature. In standard glass fibres, the dependence is very weak, hence resulting in an ineffective sensor [5]. In liquid-core fibre, the backscattered Raleigh signal intensity is relatively temperature dependent. In 1983, Hartog *et al*. [76] demonstrated a temperature measurement in liquid core fibres with an accuracy of $\pm 1^{o}$C and 1 m spatial resolution over 100 m fibre length. The obtained temperature sensitivity of 2.3×10^{-2} dB/^{o}C. However, liquid core fibres have potential difficulties of long-term durability and ineffective to format back the liquid core under cool temperatures. Moreover, for the practical applications, this sensor is limited by the special need of liquid core fibres.

Research on Raleigh scattering has been extended by analysing the phase information of the backscattered Raleigh signal, the acoustic signals can be detected. Hence, the phase-OTDR is a promising technique for distributed acoustic sensing (DAS). In 2013, Daley *et al*. [77] described the measurement of ‘‘echo’s baesd on analysing the backscattered Rayleigh signal phase information, which is φ-OTDR technique. Later, this technique demonstrated a field test of DAS for subsurface seismic monitoring. The seismic profile was recorded over the 1.5 km with a 1 m spatial resolution. In 2014, Masoudi *et al*. [78] demonstrated a distributed optical fibre audible frequency sensor along a 1 km sensing fibre with a 1 m spatial resolution. The sensing fibre composed of

two sections of standard silica single-mode fibre including a 3.5 m section that was attached to a polystyrene sheet and the acoustic perturbation was applied via a loud-speaker. The proposed φ-OTDR sensor detects acoustic signals within a frequency range of 200 Hz to 5000 Hz with a frequency resolution of 10 Hz and a spatial resolution of 1 m. However, improvements in DAS sensing range, sensitivity and spatial resolution are required for further φ-OTDR development.

3.3 Raman based Distributed Fibre Sensors

Raman based distributed fibre sensors have been widely investigated for temperature measurement, as the Raman intensity changes linearly with temperature variations. In 1985, Dakin *et al*. [79] demonstrated a Raman based distributed temperature sensor with a 200 m fibre with a temperature resolution of 10^{o}C. Raman based temperature sensors have a limited sensing range and their response time increases with the sensing distance at a required measurement resolution. This is because of the lower intensity nature of the Raman scattering and broad spectral linewidth (~5 THz), the received signal required a number of averages, because of lower signal-to-noise ratio, thus increases the measurement time to several minutes. The response time demonstrated by Ericson [80] is 4 min for a sensing range of 2 km with temperature resolution of ±2^{o}C and the spatial resolution of 1 m. If the sensing range is 4 km for the same temperature and spatial resolutions, the response time increases to 48 min. This is due to sensing range increases, then the required number of averages increases significantly. Tanner *et al*. [81] demonstrated a 60 s measurement time with 3^{o}C measurement uncertainty with a 3 m sensing fibre. In 2011, a multi-photon counting method [82, 83] was proposed to improve the spatial resolution in the order of centimetres (40 cm) with a 2 km of sensing fibre, 2^{o}C measurement accuracy and 5 min measurement time, which is a significant improvement in terms of spatial resolution. Currently, the commercial distributed Raman fibre sensors

provide 5 m spatial resolution up to 30 km sensing range with a measurement time up to few minutes. The promising applications include toxic pipelines monitoring, electrical transformers monitoring, and applications in the thermal and civil industry for long-term temperature monitoring.

The Raman scattering is sensitive to the temperature only, whereas, the Brillouin frequency changes linearly with both strain and temperature, which makes the simultaneous measurement. Moreover, the strong motivation for using Brillouin based distributed sensor over the Raman based distributed sensor are (i) the backscattered Brillouin signal magnitude higher than the Raman signal, therefore, better sensing performance and longer sensing range can be obtained; (ii) the small frequency difference between the Raleigh and Brillouin signal (~11 GHz), and its input pump allows to use low loss window of around 1550 nm and are compatable with an EDFA for amplification; (iii) the narrow linewidth of the Brillouin signal, thus the optical heterodyne detection can be recovered the signal resulting in more convenient signal processing. Therefore, since 1990's, the distributed fibre sensors research community has focused on the development of Brillouin based distributed fibre sensors.

3.4 Brillouin based Distributed Fibre Sensors

This section describes the time domain Brillouin based techniques and their operating principles. When a light wave propagates through an optical fibre, a small fraction of the light is backscattered due to the interaction between the input photons and acoustic phonons. Due to this interaction, the Brillouin scattering experiences a frequency shift, which is down-shifted (Stokes) and up-shifted (anti-Stokes) with respect to the input light frequency. The dependence of the Brillouin frequency and intensity along the fibre distance is the basis for the distributed strain and/or temperature sensing. For measuring distributed strain and/or temperature, two Brillouin-based techniques are widely used; the

Brillouin optical time domain reflectometry (BOTDR) based on spontaneous Brillouin scattering (SpBS) and Brillouin optical time domain analysis (BOTDA) based on stimulated Brillouin scattering (SBS). The BOTDR system features simple implementation schemes and only requires access to the single end of the sensing fibre. Whereas, the BOTDA system requires access to the both ends of the sensing fibre with complex system implementation [3, 4].

3.4.1 Brillouin Optical Time Domain Reflectometry (BOTDR)

Brillouin optical time domain reflectometry (BOTDR) is based on the spontaneous Brillouin signal (SpBS) and it was first proposed by a Kurashima *et al*. [84] in 1993. This method requires access to only one end of the sensing fibre. The BOTDR detection methods can be classified into two techniques, namely (i) direct detection [84] and (ii) heterodyne (coherent) detection [64].

In direct detection technique, the Brillouin signal must be optically separate from the Raleigh signal before its detection. The separation can be possible using a highly stable interferometer such as Fabry-Perot [85, 86], Mach-Zehnder [87] or narrow bandwidth fibre Bragg grating (FBG) filter [88], since the Brillouin frequency shift is relatively small (~11 GHz or ~0.088 nm).

In heterodyne detection, part of the input pump light with a narrow linewidth is employed as a reference signal (local oscillator), which allows an excellent electrical selection of the beat Brillouin signal [89]. This method comprises mixing of the backscattered signal with the local oscillator (LO) signal, which results in a beat Brillouin frequency within the photodetector bandwidth. The higher bandwidth (>12 GHz) photodetectors are commercially available, thanks to the photodetector developments. Since, the Brillouin signal is relatively weak, the direct detection method does not offer higher sensing range and measurement resolution. Whereas, the heterodyne detection

offers higher sensing range and better performance, since the LO signal significantly improves the receiver sensitivity [90, 91]. Therefore, the efficient detection technique in BOTDR system is heterodyne detection.

3.4.1.1 Operating Principle

The schematic representation of the heterodyne BOTDR system is illustrated in Figure 3.3. The major advantage of the BOTDR system, it requires access to the only one end of the sensing fibre with a simple implementation. A narrow linewidth laser source is split into two propagation paths, the upper path used to generate pump pulses and lower path is used for an LO signal. The electro-optic modulator (EOM) modulates the electrical pulses into optical pulses at a required pulse width. The pump light propagates through the circulator port 1 to 2, while port 3 collects the backscattered signal. A heterodyne detection technique is used, where LO signal mixed with a backscattered signal to get the beat Brillouin signal. Then, the signal is detected and analysed by an electrical spectrum analyser. Table **3.1** summarizes the Brillouin frequency shift (BFS) and its strain and temperature coefficients for silica single-mode fibre (SMF), graded-index multimode fibre (MMF), Germanium-doped photonic-crystal fibre (PCF), Erbium-doped fibre, Tellurite fibres, perfluorinated graded index-plastic optical fibre (PFGI-POF), Bismuth-oxide fibre, Chalcogenide fibres, Neodymium-doped fibre and Thulium-doped fibres.

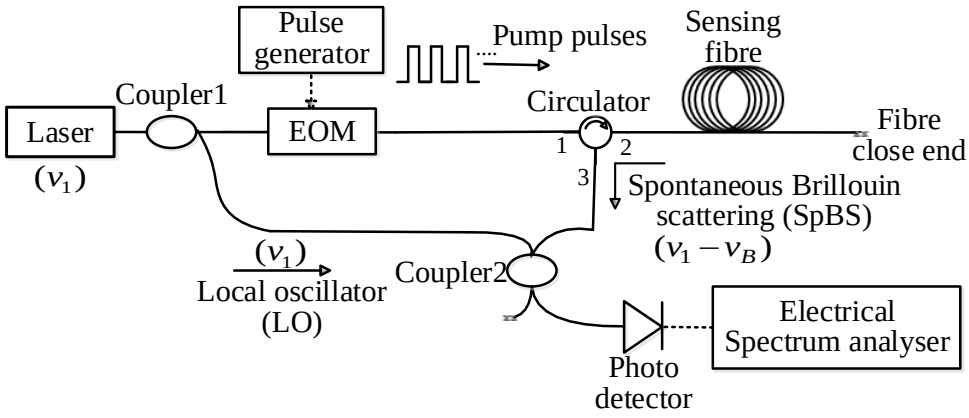

Figure 3.3. Schematic representation of heterodyne BOTDR system

Table 3.1. Brillouin frequency shift (BFS) and strain, temperature coefficients for different type of fibres

Fibre type	**Attenuation (dB/km) @1550 nm**	**BFS (GHz)**	**Strain coefficient (MHz/%)**	**Temperature coefficient (MHz/°C)**
Silica SMF [92]	~0.2	~10.85	+580	+1.18
Silica GI-MMF [93]	~0.4	~9.8	+421	+0.826
Ge-doped PCF [94]	~4.5	~10.93	+409	+0.82
Er-doped [95]	~30	~11.42	+479	+0.87
Tellurite [96]	~58.8	~7.95	-230	-1.14
PFGI-POF [97]	~150	~2.83	-122	-4.09
Bismuth-oxide [96]	~800	~8.83	-	-
Chalcogenide [98]	~840	~7.95	-	-
Nd-doped [99]	~270 dB/m	~10.82	+466	+0.73
Tm-doped [99]	~200 dB/m	~10.90	+433	+0.93

The most commonly used sensing fibre is standard single-mode silica fibre, as its low attenuation profile (~0.2 dB/km), commercially available standard fibre and comparably high sensitivity among other type of fibres.

The relation of Brillouin frequency shift and corresponding derivatives can be written as [34],

$$\nu_B = \frac{2n\nu_a}{\lambda_p} \tag{3.1}$$

$$\frac{\partial \nu_B}{\partial \varepsilon} = \frac{2}{\lambda_p}\left(\nu_a \frac{\partial n}{\partial \varepsilon} + n\frac{\partial \nu_a}{\partial \varepsilon}\right) = \nu_B C_\varepsilon, \tag{3.2}$$

$$\frac{\partial \nu_B}{\partial T} = \frac{2}{\lambda_p}\left(\nu_a \frac{\partial n}{\partial T} + n\frac{\partial \nu_B}{\partial T}\right) = \nu_B C_T, \tag{3.3}$$

where ν_B is the Brillouin frequency shift, n is the refractive index, ν_a is the acoustic velocity, C_ε and C_T are the strain and temperature coefficients, respectively. These coefficients depend on the fibre configuration and its material doping concentration [100]. The typical values of strain and temperature coefficients for silica fibre are 0.05 MHz/με and 1.1 MHz/°C, respectively [43, 86]. The Brillouin frequency shift influenced by both

refractive index and the acoustic velocity of the fibre and it changes linearly with the strain and temperature variations. However, it is the contribution from the variation of acoustic velocity that dominates the resultant Brillouin scattering. If the fibre strain remains constant, the change in Brillouin frequency shift can be directly transformed into a temperature change, alternatively, the change in Brillouin frequency shift provides a change in strain. Therefore, the BFS is able to detect both strain and temperature for a wide range of sensing applications. However, the change in Brillouin frequency shift $\left(\Delta \nu_B\right)$ and Brillouin power $\left(\Delta P_B\right)$ are both linearly dependent on the strain and temperature, this makes the discriminative measurement along the fibre is possible by using the following matrix [101],

$$\begin{bmatrix} \Delta \nu_B \\ \Delta P_B \end{bmatrix} = \begin{bmatrix} C_\varepsilon^{\nu_B} & C_T^{\nu_B} \\ C_\varepsilon^{P_B} & C_T^{P_B} \end{bmatrix} \begin{bmatrix} \Delta \varepsilon \\ \Delta T \end{bmatrix} \tag{3.4}$$

where $C_\varepsilon^{\nu_B}$ (0.05 MHz/με) and $C_T^{\nu_B}$ (1.1 MHz/^{o}C) are the strain and temperature coefficients of the Brillouin frequency shift [86], $C_\varepsilon^{P_B}$ (-9×10^{-4}%/με) and $C_T^{P_B}$ (0.30%/^{o}C) are the strain and temperature coefficients of the Brillouin power [85, 102], respectively for a silica SMF at 1550 nm pump wavelength. The matrix (3.4) can be yeild to the following equations,

$$\Delta \nu_B = C_\varepsilon^{\nu_B} \Delta \varepsilon + C_T^{\nu_B} \Delta T \tag{3.5}$$

$$\Delta P_B = C_\varepsilon^{P_B} \Delta \varepsilon + C_T^{P_B} \Delta T \tag{3.6}$$

The Brillouin frequency shift and Brillouin power coefficients of strain and temperature need to be measured precisely, where the Brillouin power change with strain is relatively very low compared with the temperature change [100]. The detailed description can be found in [101, 103]. The measurement distance, z_i can be determined using time domain

analysis from the position where the pulsed pump signal is launched to the position where the scattered signal is generated,

$$z_i = \frac{c.\,\Delta t}{2.\,n} \tag{3.7}$$

where *c* is the light velocity in vacuum, *n* is the refractive index and Δt is the time interval between the launching pulse and backscattered signal. It is important to mention that the intensity based measuremnt is somewhat not reliable, as the intensity fluctuations affected by several factors such as polarization noise, splice and bending losses.

In BOTDR system, the peak power distribution of the Brillouin scattering over the fibre distance is governed by the input pump power. Assuming that the input pump signal and backscattered Brillouin signal loss are equal, the backscattered Brillouin signal peak power distribution over the fibre distance can be expressed as [104],

$$P_B(L) = 0.5 P_p W \alpha_B S v_g e^{(-2\alpha_R L)} \tag{3.8}$$

where P_p is the input pump power, W is the pulse width or pulse duration, α_B and α_R are the Brillouin and Raleigh scattering coefficients, respectively, v_g is the group velocity and *L* is the fibre length. *S* is the backscattered capture fraction, which measures the amount of collected backscattered signal within the numerical aperture of the fibre and it is given by [104],

$$S = \frac{(NA)^2}{4n^2} \tag{3.9}$$

where *NA* is the numerical aperture of the fibre. Furthermore, the Brillouin scattering coefficient can be expressed as [105],

$$\alpha_B = \frac{8\pi^3 n^8 p^2 kT}{3\lambda_p^4 \rho v_a^2} \tag{3.10}$$

where p is the photoelastic coefficient (~0.29), k is the Boltzmann constant (1.38×10^{-23}J/K), T is the fibre temperature (298 K), λ_p is the pump wavelength (1550 nm), ρ is the material density (2200 kg/m^3) and v_a is the acoustic velocity (~5960 m/s). Using the above equation and values defined for silica fibre, the Brillouin scattering coefficient is approximately, $\alpha_B \cong 0.092$ km^{-1} at 1550 nm [105]. The logarithmic slope of the Brillouin power is equal to the double pass loss coefficient, which is ~0.4 dB/km.

3.4.1.2. Dynamic Range

The measurable one-way fibre loss range or dynamic range (DR) of the BOTDR system is defined as the longest sensing range can be reached at a required strain/temperature accuracies (or at a required SNR) is expressed as [28, 106],

$$DR = \frac{1}{2}\left\{P_p + R_B - L_c - P_d + \frac{SNRI}{2} - \frac{SNR_r}{2}\right\} \tag{3.11}$$

where P_p is the input pump power (dBm), R_B is the Brillouin backscattering factor (dB), L_c is the directional coupler loss (dB), P_d is the minimum detectable power of the receiver (dBm), $SNRI$ is the SNR improvement (averaging and other sophisticated techniques) (dB), SNR_r is the SNR required for strain/temperature measurement (dB). Furthermore, the Brillouin backscattering factor, R_B can be expressed as [106],

$$R_B = 10\log(0.5S\alpha_B cW) \tag{3.12}$$

where S is the backscattered capture fraction, α_B is the Brillouin scattering coefficient, c is the light velocity and W is the pulse width.

In order to give an idea of the dynamic range (measurable one-way fibre loss range) of the BOTDR system, typical values are substituted into equation (3.11). Adopting the typical values defined in [28], which were input pump power, P_p =18 dBm, Brillouin

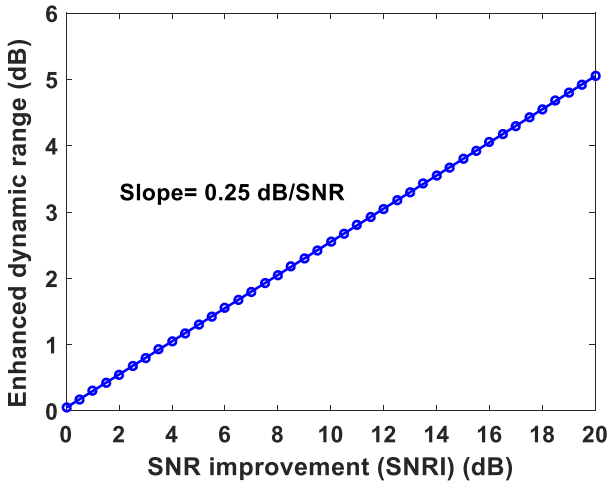

Figure 3.4. SNR improvement vs enhanced dynamic range

backscattering factor, R_B =-68 dB, pulse width 1 µs and the directional coupler loss, L_c =5 dB. The minimum detectable power, P_d by the receiver is assumed to be -62 dBm for a bandwidth of 1 MHz, which is a typical value for Ge-Avalanche photodiode. Assuming the required SNR for a 1°C temperature accuracy is, SNR_r = 25 dB and $SNRI$ =20 dB after the 4000 trace averages, the dynamic range estimated to be 10.2 dB at a spatial resolution of 100 m [35]. At the same set of conditions, theoretically evaluated the dynamic range improvement with an improved SNR using equation (3.11) and illustrated in Figure 3.4 and the obtained slope is 0.25 dB/SNR. Therefore, for each 1 dB SNR improvement, the dynamic range improvement is 0.25 dB, which corresponds to 1.25 km sensing range improvement (since the attenuation for silica SMF is 0.2 dB/km).

3.4.1.3. Spatial Resolution

Spatial resolution is the ability to resolve two adjacent sections of distinct Brillouin frequency induced by either strain or temperature. In other words, the spatial resolution is defined as the minimum distance over which the system is able to indicate the measurand value. The input pump pulse width determines the spatial resolution and it is described as [100],

$$\Delta z = \frac{(c/n)W}{2} \tag{3.13}$$

where c is the light speed in a vacuum and W is the pulse width. In order to improve the spatial resolution, one way to reduce the input pump pulse width. However, the pump pulse width cannot be shorter than the acoustic phonon lifetime τ_a, which is about 10 ns for the silica fibre [41, 107]. This is because acoustic phonons excited by such short pulse cannot generate Brillouin scattering efficiently. In addition, this further causes decrease in Brillouin gain and broaden the spectral linewidth. Therefore, the Brillouin peak frequency is difficult to determine accurately. In real-time measurement, the spatial resolution is determined by the rise time or fall time that corresponds to the 10% to 90% of the average power as shown in Figure 3.5. Rise time refers to the time it takes for the leading edge from its minimum to its maximum value, which is typically measured from 10% to 90% of the value. Conversely, fall time is the measurement of the time it takes for the signal power to move from the highest value to the lowest value. In distributed fibre sensor community, the spatial resolution is determined by the either rise time or fall time that can be converted into distance.

There is a strong trade-off between the spatial resolution and maximum sensing range. The spatial resolution is determined by the transmitted pulse width duration, whereas the maximum sensing range is defined by the strength of the backscattered Brillouin signal

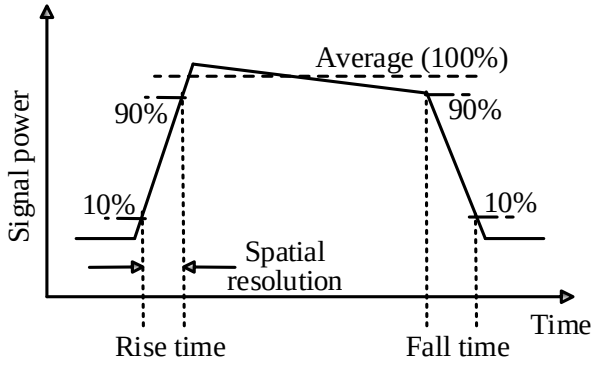

Figure 3.5. Evaluation method of spatial resolution

detected by the receiver. To achieve a better spatial resolution, the shortest possible pulse has to be launched into the sensing fibre. The short pulse contains less energy and can only cover a short fibre distance, which also makes the backscattered power is relatively low. This ultimately limits the sensing range of the system. Similarly, longer pulse width contribute to higher sensing range but compromise the spatial resolution.

In order to better understand the Brillouin power distribution at different injected pump powers and pulse widths (spatial resolution), a numerical simulation was performed using equations (3.8), (3.9), (3.10) and the values defined in Table 3.2. For the different input pump powers at a fixed pulse width of 100 ns, the Brillouin power distribution is shown in Figure 3.6. Figure 3.7 illustrates the Brillouin power distribution at a fixed input pump power and different pulse width of 10, 50 and 100 ns. If the pulse width reduces at a fixed input power of 100 mW, the Brillouin scattering power is relatively weak, thus reduces the sensing range.

Table 3.2. Parameter values used for Brillouin power distribution over the fibre distance [105, 108]

Parameter	**Symbol**	**Value**
Refractive index	n	1.46
Photoelastic coefficient	p	0.29
Boltzmann constant	k	1.38×10^{-23} J/K
Pump wavelength	λ_p	1550 nm
Material density	ρ	2200 kg/m^3
Acoustic velocity	v_a	5960 m/s
Backscattered capture fraction	S	0.024
Numerical aperture	NA	0.14
Group velocity	v_g	2×10^8 m/s
Fibre length	L	50 km

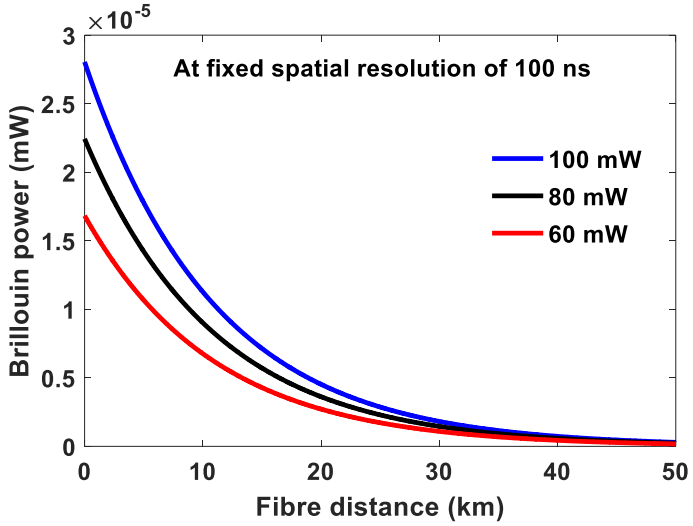

Figure 3.6. Brillouin power distribution at different pump powers and fixed pulse width of 100 ns (corresponds to 10 m spatial resolution)

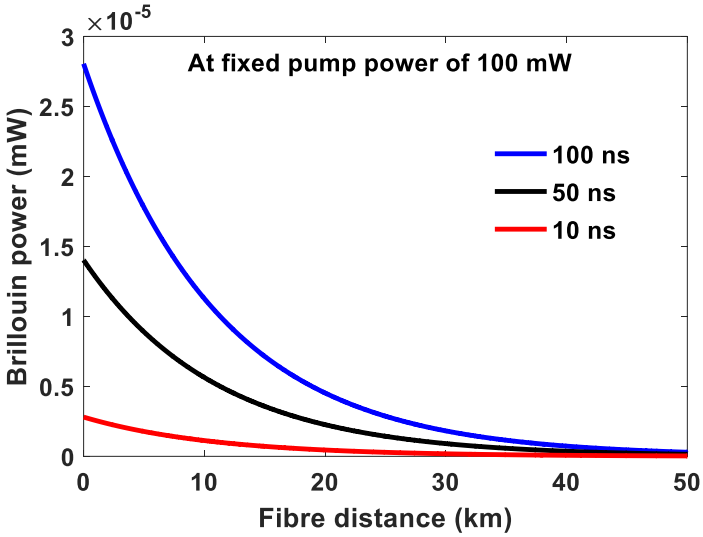

Figure 3.7. Brillouin power distribution at different pulse widths and fixed pump power of 100 mW

The first BOTDR system was proposed in 1993, which is based on the direct detection technique and separate a weak Brillouin signal from a strong Rayleigh scattering peak and Fresnel reflected light before the detection [84]. Thereafter, in 1994 [64] the same research group was demonstrated a heterodyne BOTDR system employing a local oscillator signal. The proposed heterodyne BOTDR system results demonstrated using a 30 km sensing fibre with 100 m spatial resolution and the strain and temperature resolutions are ±100 με, ±6^{o}C, respectively. The polarization noise is the dominant noise

source in heterodyne BOTDR system, hence restricted the strain and temperature resolutions [64]. Considering the polarization noise, T Kurashima *et al*. [109] was proposed a heterodyne BOTDR system by randomising the polarization state of the local oscillator signal. The experimental results were demonstrated using a 10 km sensing fibre with 1 m spatial resolution. The measurement errors without and with randomising the polarization state of the local oscillator signal are ±6 MHz and ±1.5 MHz, which corresponds to strain measurement errors of ±200 με and ±50 με, respectively. However, randomizing the local oscillator signal polarization state requires repeatable and accurate polarization controlling. Therefore, over the decade the fibre sensor research community has adopted a polarization scrambler, which significantly reduces the polarization noise [110, 111].

In 2000, H. Kee *et al*. [112] proposed a high spatial resolution (35 cm) BOTDR temperature sensor based on measuring the ratio of the SpBS signal intensity to the Rayleigh backscattered signal intensity, which was named the Landau-Placzek ratio. The time difference between the launched pulse signal and detected backscattered signal provides the distance measurement, while the SpBS signal intensity measures the temperature information. The pulse peak power of 4.5 W was launched at a 1550 nm wavelength with a 3.5 ns pulse width. The experimental results demonstrate a temperature resolution of ±4.3^{o}C and a spatial resolution of 35 cm with a 1 km sensing fibre.

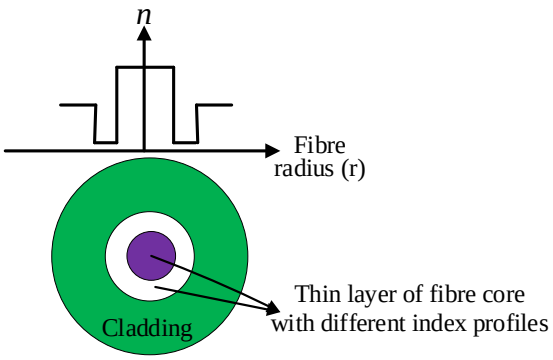

Figure 3.8. Cross sectrion of DSF and refractive index profile

In 2001, C. Lee *et al*. [113] proposed a simultaneous measurement of strain and temperature based on the dispersion-shifted fibre (DSF). The DSF has a compound composition structure in the fibre core, the two-peak structure in the Brillouin gain spectrum of the DSF arises from the different acoustic velocities, which are due to the different compositions or doping concentrations in the fibre core. The cross section image and fibre core refractive index profile is shown in Figure 3.8. The BFS of the two peaks

Table 3.3. Progress summary of BOTDR techniques

Technology	**Year**	**Sensing range (km)**	**Spatial resolution (m)**	**Temperature accuracy (ºC)**	**Strain accuracy (με)**
Proposal of BOTDR (Direct detection) [84]	1993	11.57	100	3	60
Heterodyne detection BOTDR [64]	1994	30	100	5	100
BOTDR based on randomising the polarization [109]	1996	10	1	not stated	50
Landau-Plazcek ratio BOTDR [112]	2000	1	0.35	4.3	not stated
Dispersion shifted fibre (DSF) based BOTDR [113]	2001	3.7	2	5	60
Double pulse BOTDR (DP-BOTDR) [114, 115]	2007	1	0.20	not stated	20
Optical switch based BOTDR [116]	2014	48.5	25	3.8	not stated
BOTDR using Raman amplifier [117]	2015	100	10	3	not stated
BOTDR based on differential Brillouin spectrum [118]	2016	7.8	0.40	not stated	not stated
Fast Fourier transform (FFT) and complementary coding BOTDR [119]	2017	10	2	0.37	7.4
Phase-shift pulse BOTDR (PSP-BOTDR) [120]	2017	0.5	0.20	not stated	not stated

(peak 1 and peak 2) has a same strain coefficient value (0.05 MHz/με) for both peak 1 and peak 2, whereas the temperature coefficient for peak 1 (0.918 MHz/^{o}C) and peak 2 (0.98 MHz/^{o}C) have different values. Therefore, this method allows simultaneous measurement of strain and temperature over the fibre distance. The experimental results demonstrated for a 3.7 km sensing fibre of DSF, a strain resolution of 60 με and a temperature resolution of 5^{o}C with a spatial resolution of 2 m are achieved simultaneously.

In 2007, S. Yoshiyuki *et al*. [114, 115] developed a double-pulse BOTDR (DP-BOTDR) with a spatial resolution of 20 cm and strain accuracy of ±20 με for a 1 km sensing fibre. The BFS distribution along the fibre distance was measured by a launching the double-pulse signal with a pulse width of 2 ns, a front-pulse to the rear-pulse time interval of 5 ns and peak pulse power of 32 dBm. Thereafter, several works have been done for spatial resolution improvement, such as BOTDR based on differential Brillouin spectrum [118], complementary coding BOTDR [119] and phase-shift pulse BOTDR (PSP-BOTDR) [120]. Over the decade, many research works have been proposed to improve the spatial resolution using pulse coding techniques. For example, F. Wang *et al*. [119] combined the fast Fourier transform (FFT) with a complementary coding technique and achieved a spatial resolution of 2 m with a 10 km sensing range. R. Shibata *et al*. [120] proposed a phase-shift pulse (PSP) coding in order to improve the spatial resolution of 20 cm. The well-known techniques in BOTDR system are summarized in Table **3.3**. However, the sensing performance, such as measurement accuracy and sensing range is still limited by the restricted input pump power.

The signal-to-noise ratio (SNR) determines the performance of the BOTDR system. The SNR is primarily governed by the injected pump power into the sensing fibre and the LO signal power. Increasing the injected pump power into the sensing fibre will improve the SNR but the level of the pump power is limited by the non-negligible nonlinear effects

in the sensing fibre, which comprises of SBS and modulation instability (MI) [121]. Therefore, the maximum injected pump power should be below the nonlinear threshold level in order to avoid the non-negligible nonlinear effects. If the pump power is above the nonlinear threshold, it will result in a rapid depletion of the pump power which in turn limits the sensing range. The nonlinear threshold will be described more in Chapter 4.

3.4.2 Brillouin Optical Time Domain Analysis (BOTDA)

Brillouin optical time domain analysis (BOTDA) is based on the stimulated Brillouin scattering (SBS), which utilises a counter propagating continuous wave coupled in at the another end of the same fibre. The BOTDA system requires access to both ends of the sensing fibre.

The schematic representation of the BOTDA system is shown in Figure 3.9. This method was first developed by a Horiguchi *et al*. [27] in 1989. The pump wave at the frequency v_1 is modulated with pulses using an EOM and injected into one end of the sensing fibre using a circulator. Whereas, a counter-propagating continuous wave (also known as a probe) at the frequency, $v_1 - v_B$ is injected at another end. The two optical isolators are placed after each laser to avoid any reflected optical signal coupling into the laser which could interfere with the laser operation. The input pump pulse propagation generates SpBS at a frequency of $v_1 - v_B$, and the SBS occurs only the fibre location where the counter propagating probe wave superimpose the SpBS signal. In order to

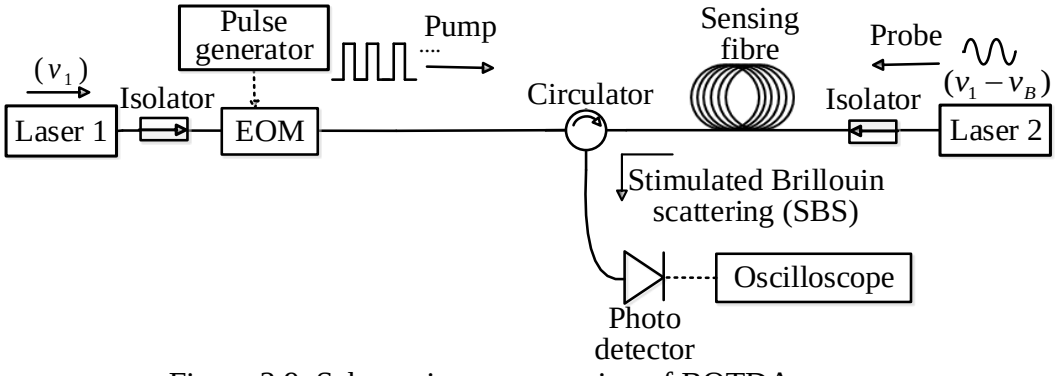

Figure 3.9. Schematic representation of BOTDA system

superimpose the two signals, the counter-propagating probe wave frequency must be same as the local Brillouin frequency, $(\nu_1 - \nu_B)$ along the fibre distance. The detection technique is similar to the standard OTDR system [75]. The SBS signal detected at the section where the pump pulse signal is launched and monitor as a function of time.

The major drawbacks of the basic configuration illustrated in Figure 3.9 are the use of two distinct laser sources to generate pump pulse and continuous wave probe. The system suffers from the frequency offsets of the two laser sources, as the stability of frequency and power of the two laser sources are difficult to achieve. Therefore, the most effective configuration was proposed by Thevenaz *et al*. [122] in 1998. This configuration utilizes the one laser source to generate both pump and probe wave. The probe wave is generated by a high bandwidth EOM, which modulates to generate optical sideband frequency shift same as the Brillouin frequency as shown in Figure 3.10. The single frequency laser source was split into two signals, pump and probe signal using a 50/50 coupler. The upper branch signal is modulated by EOM 1 at a Brillouin frequency of ν_B which gives rise to new frequency components called modulation sidebands as shown in Figure 3.10. The carrier frequency, ν_1 can be suppressed by tuning the DC bias of EOM 1. The polarization controller (PC) is employed at the input of each EOM to achieve the maximum optical power at the output of the EOMs. The pump wave propagation along the fibre, the energy transfer to the Stokes wave, then the lower sideband $\left(\nu_1 - \nu_B\right)$ experiences Brillouin gain. Whereas, the upper sideband $(\nu_1 + \nu_B)$ energy transfer to the pump wave, then the upper sideband experiences Brillouin loss.

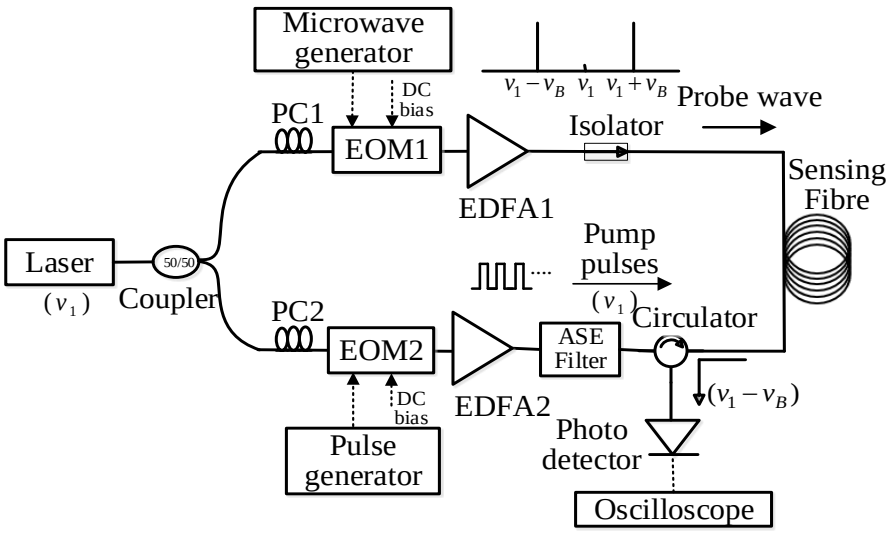

Figure 3.10. Experimental setup for modified BOTDA configuration

Numerous research works have been done for improving the BOTDA system performance. In order to improve the spatial resolution, Kishida *et al*. [123] proposed a pulse pre-pump BOTDA (PPP-BOTDA) [123] to overcome the spatial resolution limitation (~1 m), where 10 ns pulse followed by a 1 ns pulse to pre-excite the acoustic phonon and obtain a spatial resolution of ~10 cm. In 2007, a dark-pulse BOTDA [124] was proposed and 20 cm spatial resolution with a 1 km sensing range was demonstrated. Thereafter, in 2013 a phase-shift pulse BOTDA (PSP-BOTDA) [125] with a non-return-to-zero (NRZ) Golay codes was proposed, in which the first pulse (> 10 ns) to excite the acoustic phonon and followed by a second pulse (< 10 ns) with a phase shift, which determines the spatial resolution. Moreover, the improvement in SNR of 3 dB with increasing the Golay code length of 16-bit was demonstrated with a 10 cm spatial resolution. Considering the sensing range limitation, a distributed Raman amplifier was employed in BOTDA system [126] in order to extend the sensing range more than 120km with a spatial resolution of 3 m. In 2012, Y. Dong *et al*. [127] demonstrated a sensing range improvement by combining frequency-division multiplexing and in-line Erbium-doped fibre amplifiers (EDFAs). The sensing range of 150 km was achieved by dividing

Table 3.4. Progress summary of BOTDA techniques

Technology	**Year**	**Sensing range (km)**	**Spatial resolution (m)**	**Temperature accuracy (ºC)**	**Strain accuracy (με)**
Proposal of BOTDA [27]	1989	1.2	100	3	not stated
Brillouin loss BOTDA [128]	1993	32	5	1	not stated
Modified standard BOTDA [129]	1994	51	5	1	not stated
PPP-BOTDA [123]	2005	1.2	0.10	not stated	25
Dark-pulse BOTDA [124]	2007	1	0.2	not stated	20
Differential pulse-width pair BOTDA [130]	2008	1	0.15	not stated	not stated
Pulse coding BOTDA [131]	2010	50	1	2.2	44
Raman BOTDA [132]	2010	100	2	not stated	not stated
Pulse coding and pre-amplification BOTDA [126]	2011	120	3	3.1	60
Inline EDFA and frequency division multiplexing BOTDA [127]	2012	150	2	1.5	30
PSP-BOTDA [125]	2013	1	0.10	not stated	not stated
Distributed Brillouin amplification BOTDA [133]	2016	50	1	1.6	not stated
Gold coated multi-mode fibre based BOTDA [134]	2017	0.80	1	2	

the sensing fibres into two spans of 75 km. An in-line EDFAs are placed between the two spans, which is used to compensate the fibre loss. Using the differential pulse-width pair technique, a 100/120 ns pulse pair is used to get a 2-m spatial resolution and a measurement accuracy of 1.5ºC/30 με at the end of the sensing fibre. The well-known techniques of the BOTDA systems are summarized in Table 3.4.

3.4.3 Brillouin Optical Correlation Domain Analysis (BOCDA)

In conventional BOTDR and BOTDA systems, the accuracy of BFS measurement is degraded, when the pump pulse width is less than a 10 ns (corresponds to 1 m spatial resolution) [135]. Considering the spatial resolution limitation in BOTDR and BOTDA systems, in 1999, Hotate *et al*. [136] proposed a correlation-based technique, named as Brillouin optical correlation domain analysis (BOCDA) to overcome the limited spatial resolution. The SBS interaction of continuous wave pump and probe wave over the fibre distance is obtained by the controlling the phase between the two light waves. This way, the SBS interaction is confined to a certain position within the sensing fibre and its position is determined by monitoring the correlation peak.

The spatially distributed measurement is possible by sweeping the modulation frequency, f_m of the laser source. When the pump and probe waves are in phase, the Brillouin gain is maximized, otherwise, the Brillouin gain is significantly reduced. The intervals of the correlation peak, d_m and the spatial resolution, Δz can be expressed as [136],

$$d_m = \frac{v_g}{2 f_m} \tag{3.14}$$

$$\Delta z = \frac{v_g \Delta v_B}{2\pi m f_m^2} \qquad f_m < \Delta v_B/2 \tag{3.15}$$

where v_g is the group velocity in the fibre, Δv_B is the Brillouin linewidth and m is the modulation index.

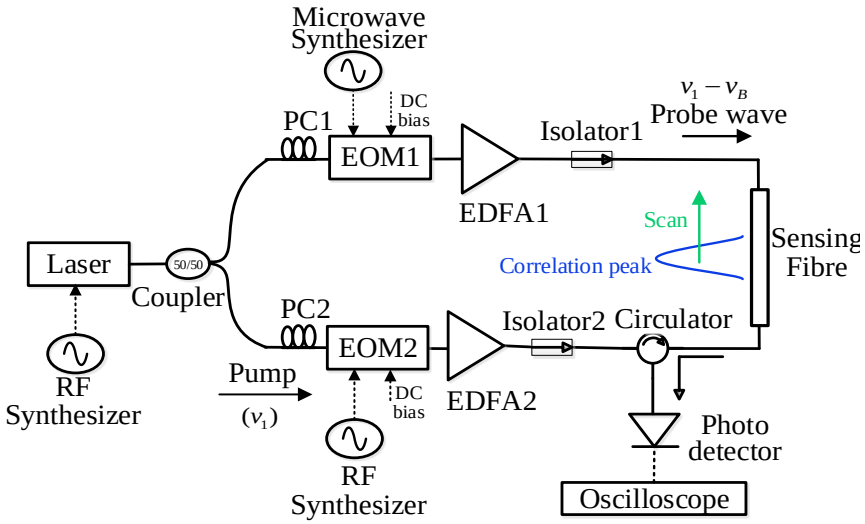

Figure 3.11. Experimental setup for Brillouin optical correlation domain analysis (BOCDA)

The experimental setup for Brillouin optical correlation domain analysis (BOCDA) is shown in Figure 3.11. The frequency modulated continuous wave is sent through a coupler. The upper branch is modulated in order to generate lower sideband frequency, $\nu_1 - \nu_B$. Whereas, the lower branch signal at a frequency, ν_1 is modulated at a lower frequency using an RF synthesizer. The signal from the RF synthesizer is used as a reference signal for the lock-in amplifier in order to detect the amplified probe wave.

Table 3.5. Progress summary of BOCDA techniques

Technology	**Year**	**Sensing range (m)**	**Spatial resolution (m)**	**Temperature accuracy (°C)**	**Strain accuracy (με)**
Proposal of BOCDA [136]	1999	7	0.65	not stated	not stated
Modified standard BOCDA [137]	2001	8	0.04	not stated	70
Differential measurement BOCDA [138]	2012	50	0.02	not stated	not stated
Multiple correlation peak BOCDA [139]	2017	10150	0.05	not stated	70

The Brillouin gain spectrum is obtained by the sweeping the probe frequency. Table 3.5 summarizes the well-known techniques and achievements to date. Recently, multiple correlation peak BOCDA [139] has been investigated with a 5 cm spatial resolution and 10.15 km sensing range, which is significant improvement in both spatial resolution and sensing range.

3.5 Summary

In this chapter, the various applications of the distributed fibre sensors are discussed. The major applications can be found in oil/gas pipeline monitoring, bridges, tunnels and building monitoring, geotechnical engineering and rail-track monitoring. Thereafter, the operating principles of Raleigh, Raman and Brillouin based distributed fibre sensors are discussed. The Brillouin scattering is the most effective technique compared to the Raleigh and Raman based techniques. Brillouin scattering can be applied for simultaneous strain and temperature monitoring over the tens of kilometres sensing fibre. Therefore, for the rail-track condition monitoring application, Brillouin based distributed fibre sensor is most effective sensing system. Brillouin based distributed fibre sensors, such as BOTDR, BOTDA and BOCDA systems are discussed with their operating principle. The well-known techniques and achievements are summarized. Significant work has been in order to improve the spatial resolution of BOTDR and BOTDA systems. However, the sensing performance such as strain/temperature measurement accuracy and sensing range are still limited by the restricted input pump power. This is considered in this thesis. Since this chapter focuses on the literature review of distributed fibre sensors, the experimental demonstration of BOTDR and BOTDA system will be presented in the following chapter.

Chapter 4
Experimental Demonstration of BOTDR and BOTDA Systems

4.1 Introduction

In this chapter, the conventional Brillouin optical time domain reflectometry (BOTDR) and Brillouin optical time domain analysis (BOTDA) systems are investigated experimentally. In order to better understand the individual device performance, the major devices such as distributed-feedback (DFB) laser and Mach-Zehnder modulator (MZM) have been characterized. An experimental testbed for BOTDR and BOTDA systems were developed and optimised at Photonics Research Laboratory, Northumbria University. The Brillouin gain spectrum (BGS) has been analysed for different strain and temperature variations. The impact of the strain and temperature on Brillouin frequency shift (BFS) is evaluated. Thereafter, the main noise sources, which limits the performance of the BOTDR system are identified. A simple, low-cost passive depolarizer is employed in local oscillator path to suppress the polarization noise and its operating principle was described. Finally, the different key factor effects on BOTDR system performance, such as a number of trace averages, Brillouin linewidth and sweep frequency step is evaluated experimentally and compared with the theoretical analysis.

4.2 Device Characterization

In this section, the characterization of DFB laser and MZM are discussed. The characterization gives the better understanding of the individual device performance.

4.2.1 DFB Laser LI Curve

The measurement setup for measuring DFB laser (Emcore, 1754C) LI curve is shown in Figure 4.1. The DFB laser is connected to the stable DC bias current source (Hewlett Packard, 6177C) and temperature controller (Thorlabs, TED200C), where the operating temperature was set at 25^{o}C. Varying the bias current between 20 mA to 120 mA, as the threshold is at 18 mA, the peak output optical power is measured using optical spectrum analyser (OSA, Yokogawa-AQ6370D). The measured LI curve illustrated in Figure 4.2. The centre wavelength at 60 mA bias current is 1550.10 nm.

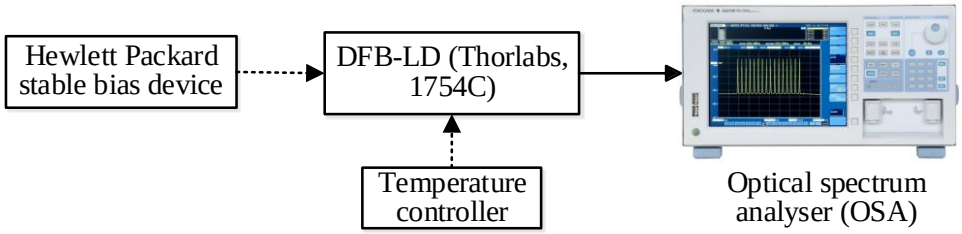

Figure 4.1. Setup for DFB laser LI curve and relative intensity noise (RIN) measurement

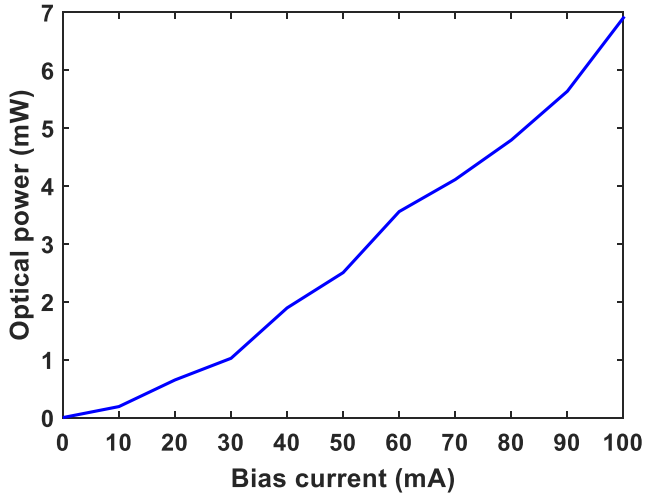

Figure 4.2. Measured LI curve of DFB laser

4.2.2 DFB Laser RIN Measurement

The relative intensity noise (RIN) describes the random fluctuations in the optical power of the laser, which mainly comes from the intrinsic optical phase and frequency

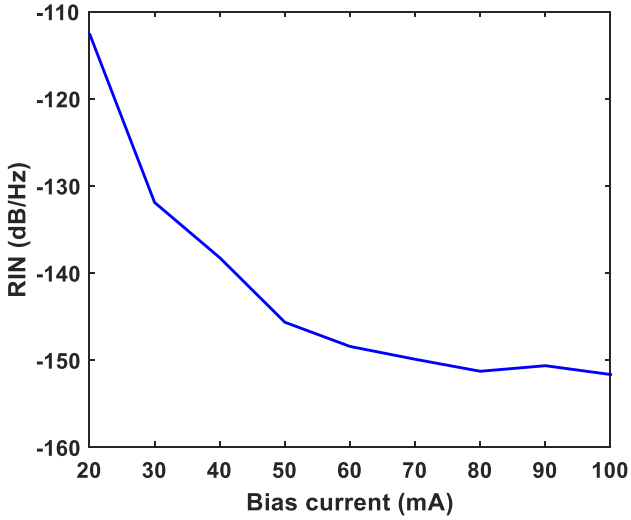

Figure 4.3. Measured RIN for various bias currents

fluctuations caused by the spontaneous emission. The RIN measurement is necessary to understand the noise level of the DFB laser output. The optical signal-to-noise ratio (OSNR) is measured at each bias current using the OSA, where the measured OSNR is used for the RIN calculation. The equivalent model for RIN calculation derived from the Keysight technologies as follows [140],

$$RIN(\text{dB/Hz}) = 10\log(k_p) + 20\log(\lambda) - OSNR_{1nm} - 174.8 \quad (4.1)$$

where k_p is the polarization coefficient (~1), λ is the centre wavelength, $OSNR_{1nm}$ is the OSNR measured at 1 nm scale. The measured RIN for corresponding bias current is shown in Figure 4.3, which decreases with the increase in bias current. The calculations performed using equation (**4.1**) and agreed well with other RIN measurements based on electrical spectrum analyser and oscilloscope techniques [140]. The decreasing pattern in RIN occurs because as the bias current increases, stimulated emission becomes the dominant output, thus spontaneous emission dependent phase noise depletes.

4.2.3 DFB Laser Linewidth Measurement

The characterization of laser linewidth is important, as the spectral linewidth of the Brillouin signal is almost constant with larger amplitude when the laser linewidth less

than the 3 MHz, otherwise, the spectral linewidth increases sharply [141]. The fundamental laser linewidth originates from the random phase fluctuations caused by the spontaneous emission within the laser cavity [142, 143]. For measuring the narrow linewidth, conventional Grating based OSAs does not offer the high measurement resolution. Typically, the Grating based OSAs gives the maximum resolution of 0.02 nm (2.5 GHz), which cannot be measure the linewidth in the range of MHz. Recently, the high-resolution OSAs are developed based on the Brillouin scattering, named as a Brillouin-optical spectrum analyser (BOSA) with a resolution of 0.08 pm (10 MHz) [14]. Even with the BOSA, unable to achieve the required measurement resolution either. L. Mercer [144], proposed a delayed self-heterodyne detection technique, which is capable of measuring the narrow linewidth spectrums in the electrical domain [145].

The experimental setup for the delayed self-heterodyne technique is illustrated in Figure 4.4. The DFB laser is operated at a stable 80 mA bias current and 25^{o}C operating temperature. The laser output is split into two propagation paths using 80/20 coupler, the upper branch used for the frequency shift and the lower branch signal used as a reference signal. The upper branch signal is fed into the intensity MZM (Photline, MXAN-LN-20), which drives at a frequency of 150 MHz using an RF signal generator (Agilent, E8247C). A 5 km fibre is used for a time delay, which must be longer than the laser coherence

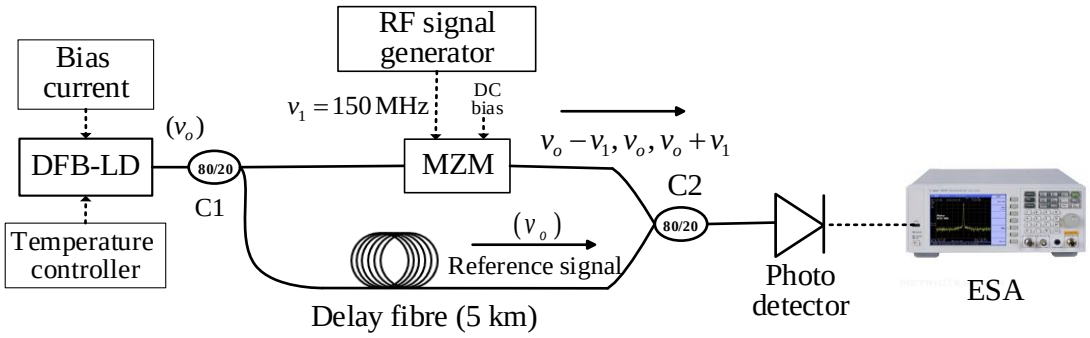

Figure 4.4. Setup for laser linewidth measurement using delayed self-heterodyne technique

(DFB-LD= distributed-feedback laser diode, C=coupler, MZM= Mach-Zehnder modulator, ESA= electrical spectrum analyser)

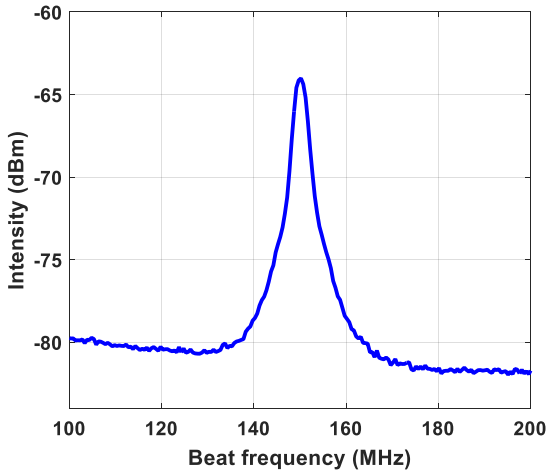

Figure 4.5. Measured beat spectrum using delayed self-heterodyne technique

length. The coherence length is the propagation distance over which a coherent wave maintains a specified degree of coherence. If the time delay difference between the two optical paths smaller than the laser coherence time, the phase between two optical signals interference becomes more significant, as a result the ripples appear in the beat spectrum. If the time delay longer than the laser coherence time, the phase between two optical signals are completely uncorrelated and the resultant beat spectrum strictly becomes Lorentzian shape without any ripples [146]. The measured beat spectrum is shown in Figure 4.5. As one can see, the linewidth at -3 dB is 1.94 MHz, which is close to DFB (Emcore, 1754C) laser specifications of 2 MHz.

4.2.4 Mach-Zehnder Modulator (MZM)

The Mach-Zehnder modulator has been widely investigated since 1980's as a potential electro-optic modulator in fibre optic research community. The schematic diagram of Lithium Niobate ($LiNbO_3$) intensity modulator is illustrated in Figure 4.6 [147]. The input waveguide is split into two waveguide paths and integrated into a $LiNbO_3$ substrate. The electrodes are positioned at one arm to ensure effective electric field generation in the waveguide region. In order to operate the intensity modulator, we should apply an RF

voltage (modulation voltage) and a bias voltage (DC voltage). The ideal transfer function of an MZM is described as [148],

$$P_o = \frac{P_{in}\alpha}{2}\left[1+\cos\left(\frac{V_{bias}}{V_\pi}\pi\right)\right] \tag{4.2}$$

where P_o and P_{in} are the output and input optical power, V_{bias} is the bias voltage, V_π is a half-wave voltage of the applied bias and α is the insertion loss of the modulator. The equivalent transfer function curve is illustrated in Figure 4.7 [149].

The MZM (Photline, MXAN-LN-20) is characterized by varying the bias voltage and measured the relative optical output power. The measured transfer function curve is shown in Figure 4.8. The quadrature point is found at 3.75 V.

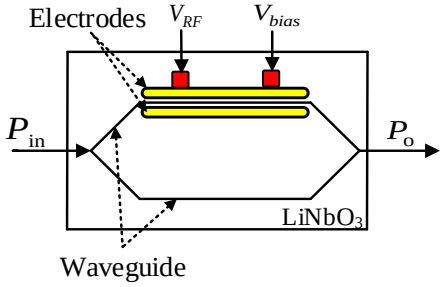

Figure 4.6. Schematic diagram of intensity MZM modulator

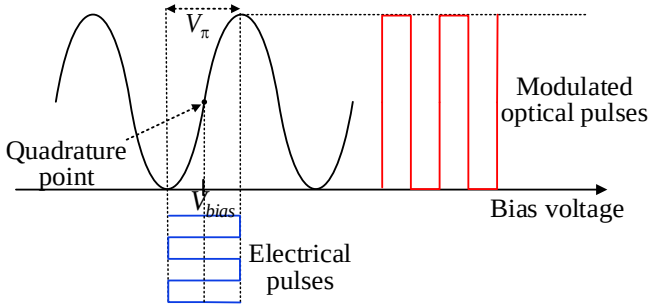

Figure 4.7. Transfer function of intensity MZM modulator

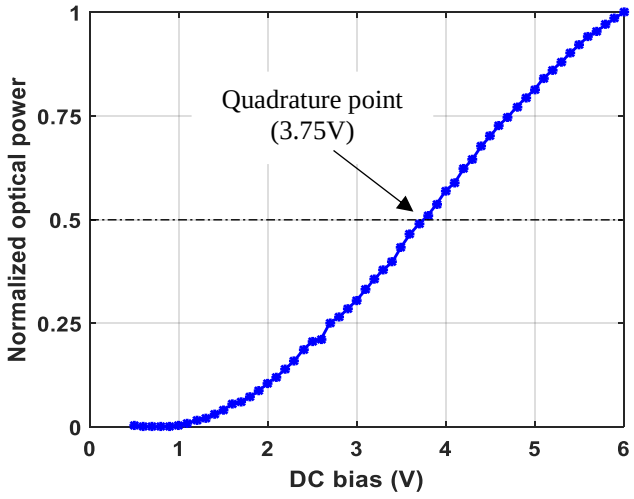

Figure 4.8. Measured transfer function curve of intensity MZM (MXAN-LN-20) modulator

4.3 Measurement of Brillouin Gain Spectrum

In this section, the Brillouin gain spectrum (BGS) using the BOTDR system has been analysed for different strain and temperature variations. The impact of strain and temperature on Brillouin frequency shift (BFS), ν_B is evaluated. The obtained strain and temperature coefficients of the sensing fibre will be used for the calibrating the distributed measurement.

The experimental setup for BGS measurement is illustrated in Figure 4.9. A DFB laser at 1550.1 nm is used as a light source. The laser output was split into two propagation paths, using 50/50 coupler 1, the upper path signal is used for the pump and the lower path is used for the reference or local oscillator (LO) signal. The pump signal is amplified by an erbium-doped fibre amplifier (EDFA, Calmar, AMP-PM-16) up to 16 dBm. Thereafter, a band-pass filter is used to remove the amplified spontaneous emission (ASE) from the EDFA to ensure accurate measurement. The variable optical attenuator (VOA) is used to adjust the required optical pump power. Thereafter, the pump signal passes through the circulator port 1 to 2, while port 3 collect the backscattered signal from the sensing fibre. Using 80/20 coupler 2, the LO signal beat with the backscattered signal,

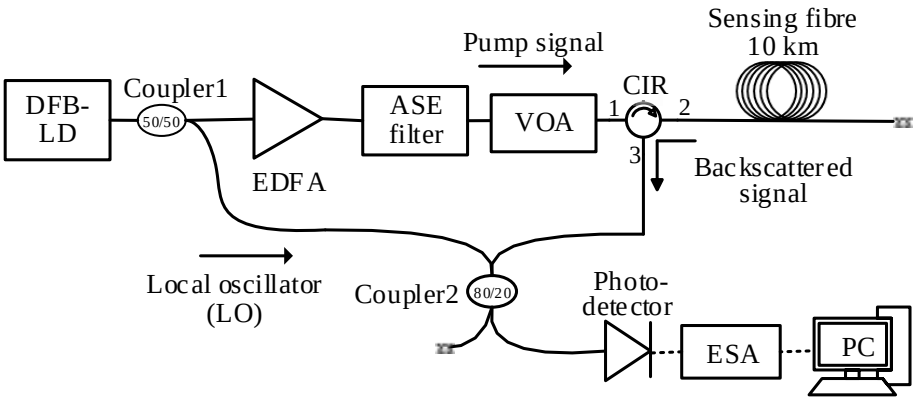

Figure 4.9. Experimental setup for Brillouin gain spectrum measurement

(DFB-LD= distributed-feedback laser diode, EDFA=erbium-doped fibre amplifier, ASE=amplified spontaneous emission, VOA=variable optical attenuator, CIR=circulator, ESA=electrical spectrum analyser)

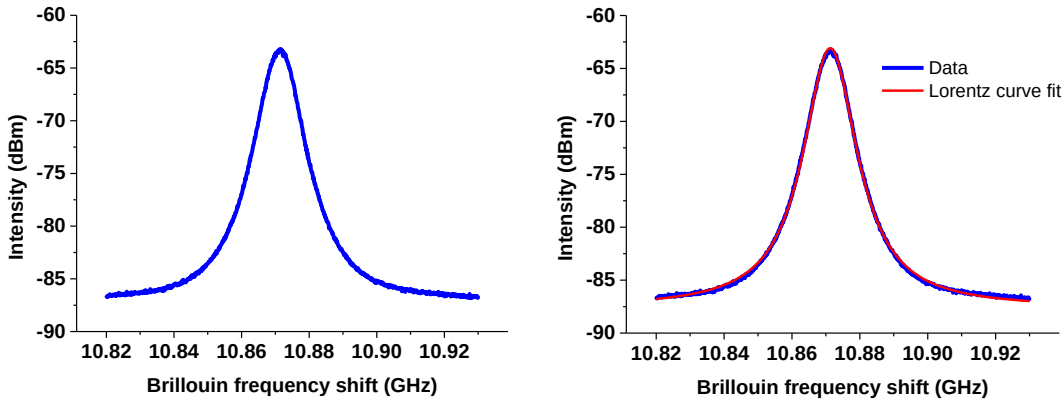

(a) (b)

Figure 4.10. (a) Measured Brillouin gain spectrum (b) Lorentzian curve fitting to the measured Brillouin gain spectrum

then the beat Brillouin signal is detected by a photodetector (Newport, D8-ir) and the BGS is visualized using an electrical spectrum analyser (Agilent, N9020A). Using 10 km sensing fibre, the measured BGS at ambient room temperature (~25^{o}C) and at strain free is shown in Figure 4.10(a). The measured BGS raw data were fitted by a Lorentzian curve fitting. The Lorentzian fitted curve to the measured BGS is illustrated in Figure 4.10(b). Therefore, we can be able to measure the peak BFS, ν_B (10.871 GHz), Brillouin linewidth (26 MHz, measured at full width at half maximum (FWHM)) and peak power (-63 dBm) simultaneously.

4.3.1 Strain Effects on Brillouin Gain Spectrum

A translation stage was developed for applying different strains on the sensing fibre. A 100 m fibre was wrapped between two cylindrical rods placed on the translation stage. The different strains were applied on the sensing fibre and the resulting spectra are shown in Figure 4.11(a). Each measured spectrum is fitted with a Lorentz curve. The linear dependence between the applied strain and the measured BFS is obtained with a slope of 0.051±0.0008 MHz/με [150]. The slope error was found to be 0.0008 MHz as shown in Figure 4.11(b).

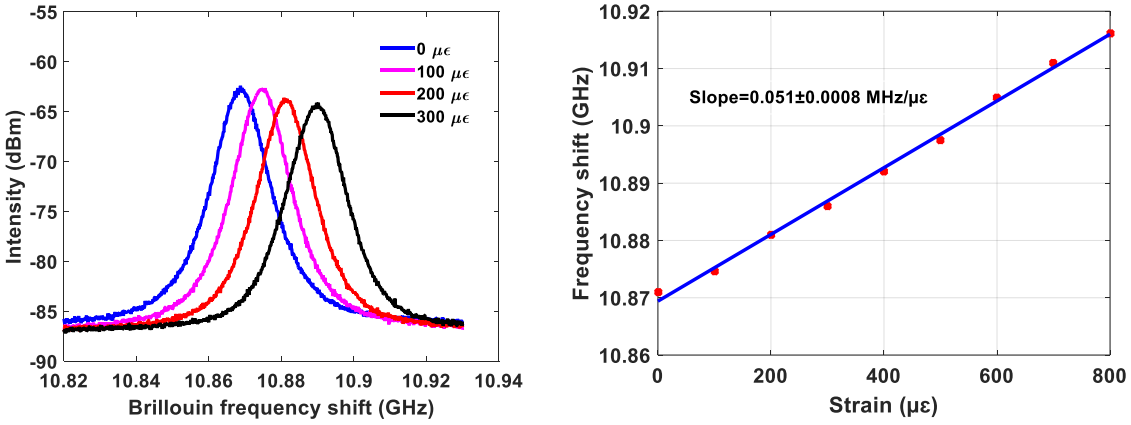

(a) (b)

Figure 4.11. (a) Measured Brillouin gain spectrums (b) Linear fitting to the measured Brillouin frequency shift (BFS) for various strains

4.3.2 Temperature Effects on Brillouin Gain Spectrum

The sensing fibre was placed in a temperature oven (Carbolite-PF60) and subject to various temperatures. The measured corresponding BGS at different temperatures are illustrated in Figure 4.12(a). The peak BFS of each measured spectrum was obtained after the Lorentz curve fitting. The linear dependence between the temperatures and measured BFS is obtained with a slope of 1.07±0.013 MHz/^{o}C [150]. The slope error was found to be 0.013 MHz, as shown in Figure 4.12(b). The obtained strain and temperature coefficients and BFS are summarized in Table 4.1.

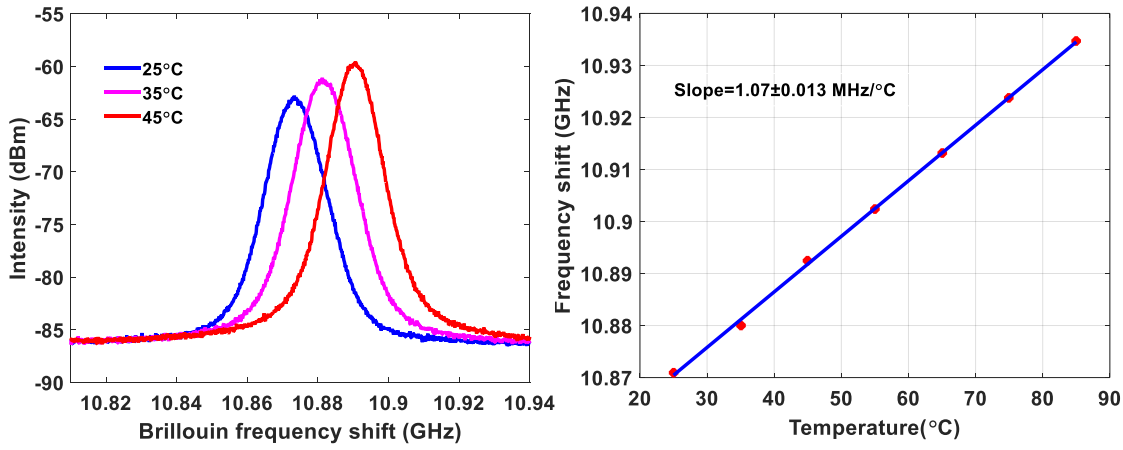

(a) (b)

Figure 4.12. (a) Measured Brillouin gain spectrums (b) Linear fitting to the measured Brillouin frequency shift (BFS) for various temperatures

Table 4.1. Measured Brillouin gain spectrum (BGS) parameters

Parameter	**Value**
Brillouin frequency shift	10.871 GHz
Linewidth (@FWHM)	26 MHz
Strain coefficient	0.05±0.0008 MHz/με
Temperature coefficient	1.07±0.013 MHz/^{o}C

4.3.3 Brillouin Threshold Measurement

The Brillouin threshold measurement is essential to avoid the nonlinear effects of the sensing fibre. The maximum input pump power into the sensing fibre is limited by the non-negligible nonlinearities, particularly stimulated Brillouin signal (SBS) and modulation instability (MI). If the input pump power is above the Brillouin threshold level, which experiences a rapid pump power depletion thus limits the sensing range. Therefore, it is important to measure the Brillouin threshold of the sensing fibre in order to avoid the nonlinear effects. The Brillouin threshold defined as, where the spontaneous scattering evolves into SBS. The Brillouin threshold can be numerically calculated using the following equation [151],

$$P_{th}^{SBS} \approx \frac{21 k_p A_{eff}}{g_B L_{eff}} \tag{4.3}$$

where A_{eff} is the effective core area (mode field area) of the fibre, k_p is the polarization constant, which lies between the 1 and 2 depending on relative polarization of the pump and Brillouin signal [56], g_B is the peak Brillouin gain coefficient and L_{eff} is the effective interaction length, which can be expressed as [151],

$$L_{eff} = \frac{(1-e^{-\alpha L})}{\alpha} \tag{4.4}$$

where α is the fibre attenuation coefficient (0.046 km^{-1} for silica fibre at 1550 nm) [152] and L is the actual fibre length. The nonlinear interactions in an optical fibre depends on

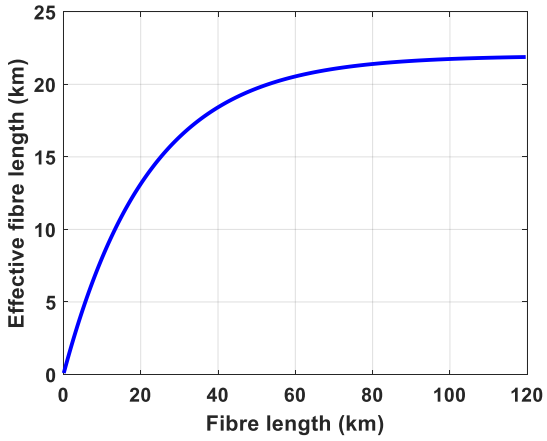

Figure 4.13. Effective fibre length vs actual fibre length

the fibre cross-sectional area and fibre length. As the signal transmission through the fibre length, the power decreases because of attenuation. Therefore, the most nonlinear effects happen at the starting of the fibre span and reduces as the signal propagates. However, in practice, that assumes as the power is constant over a certain fibre length, which is called effective fibre length, L_{eff} . Using equation (4.4), the effective fibre length calculated theoretically with the actual fibre length and illustrated in Figure 4.13. The pump power attenuation along the fibre distance makes the effective length should be less than the actual fibre length and tend to be constant for a longer length of fibres.

Furthermore, the peak Brillouin gain coefficient can be expressed as [46],

$$g_B = \frac{2\pi n^2 p_{12}^2 \gamma}{c\lambda_p^{\,2} \rho v_a \Delta v_B} \tag{4.5}$$

where *n* is the refractive index, (1.46) [44], p_{12} is the photo-elastic coefficient of silica fibre (0.29) [45], γ is the polarization factor (1 for standard silica fibre) [46], λ_p is the pump wavelength (1550 nm), ρ is the material density of the silica (2,200 kg/m^3) [47], v_a is the acoustic velocity (~5960 m/s) [47] and Δv_B is the Brillouin linewidth at FWHM (~30 MHz). The Brillouin gain coefficient gives the fractional increase in signal intensity

per unit length; therefore, it has the dimension of m/W. Using equation (4.5) and the above mentioned values, the obtained Brillouin gain coefficient, $g_B \cong 5\times10^{-11}$ m/W. In order to verify the Brillouin threshold experimentally, different pump powers are injected into the optical fibre. Figure 4.14(a) shows a backscattered spectrum for different pump powers using a 10 km fibre. Using a polynomial fit, the Brillouin threshold is determined when the backscattered power is 1% of the injected pump power. As shown in Figure 4.14(b), the Brillouin threshold for 10 km fibre is found as 12.7 dBm. There are two different definitions of Brillouin threshold, which were (i) Poletti *et al*. [153] defined the Brillouin threshold is reached when the backscattered power is 1% of the input pump power, (ii) the Brillouin threshold is reached when the backscattered power equals to the power at end of the same fibre [53].

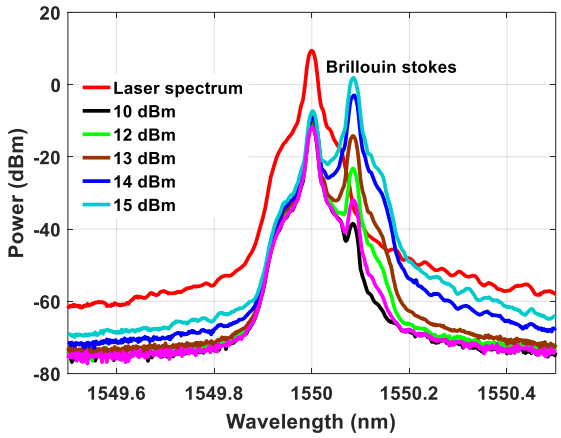

(a)

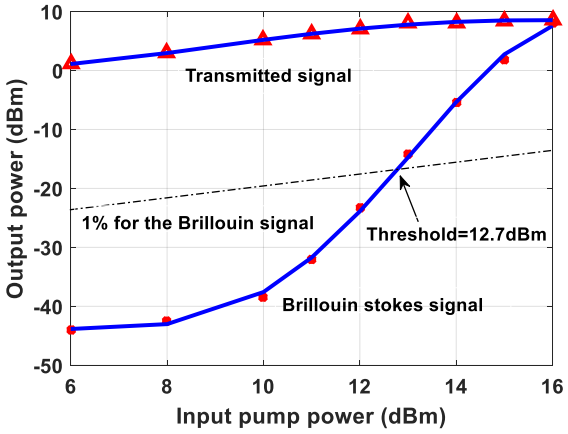

(b)

Figure 4.14. Backscattered spectrums for different input pump powers
(b) Brillouin threshold measurement for a 10 km fibre

4.4 Experimental Analysis of BOTDR System

The experimental setup of BOTDR system is illustrated in Figure 4.15. The DFB laser output is split into two propagation paths using coupler 1. The upper branch is modulated with an MZM, driven by a pulse generator, which modulates the electrical pulses into optical pulses. The polarization controller (PC) is employed at the input of the MZM to obtain the maximum optical power at the output of the MZM. Subsequently, the output signal is amplified by an EDFA. A band-pass filter is used to eliminate the ASE noise from the EDFA as shown in Figure 4.16. The peak power and pulse width of the pump signal are 18 dBm and 100 ns, respectively. The 100 ns pulse width corresponds to

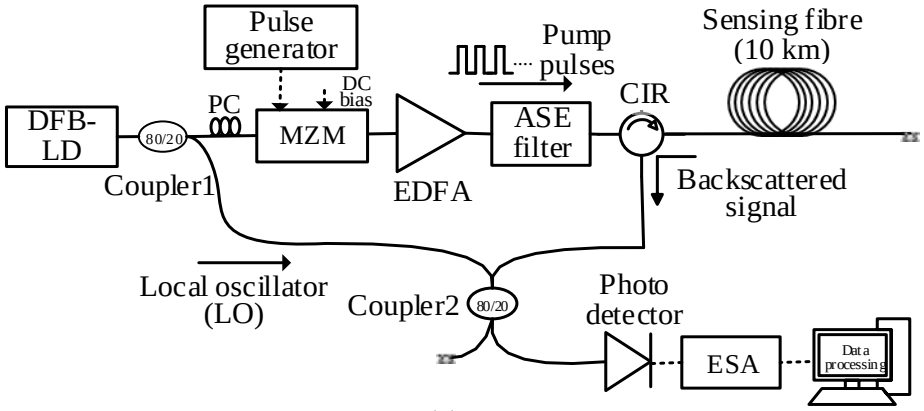

(a)

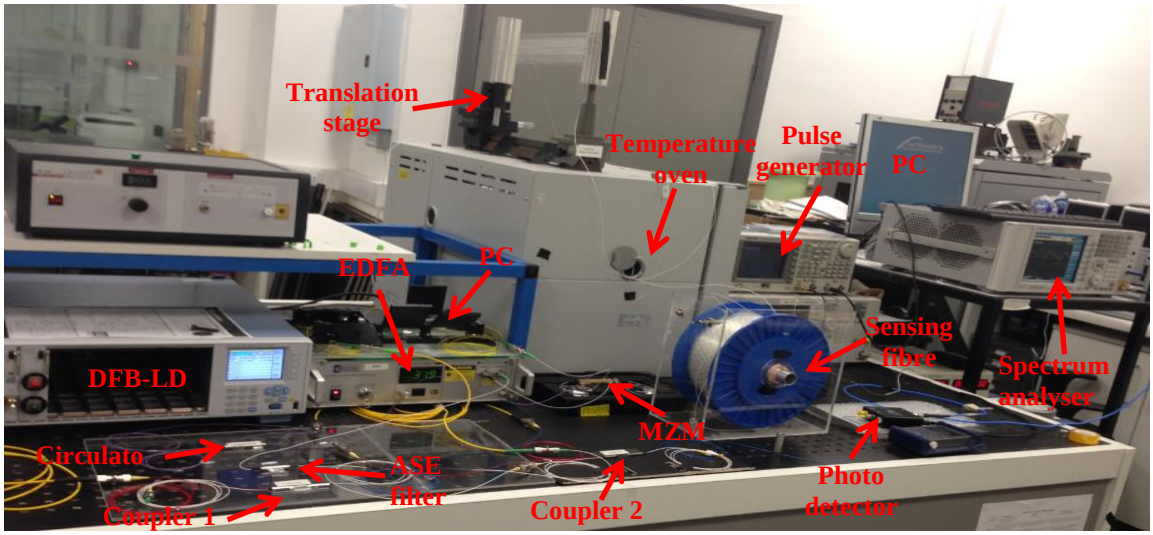

(b)

Figure 4.15. (a) Experimental block diagram (b) experimental test-bed of BOTDR system at Northumbria's Photonics Research Laboratory

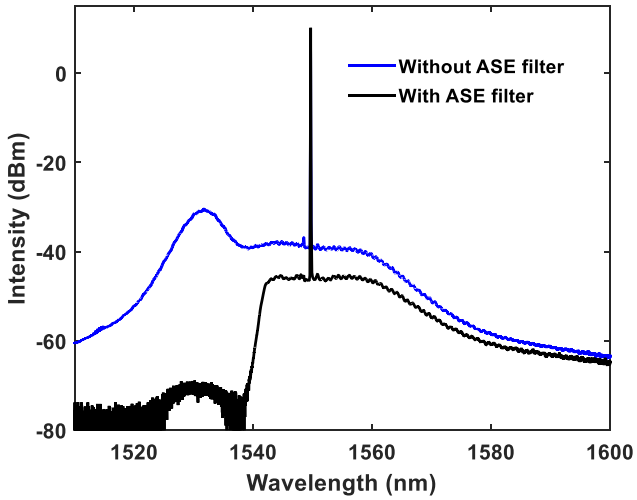

Figure 4.16. Spectrums with and without ASE filter

10 m spatial resolution. The backscattered signal beat with the LO signal and detected by a photodetector (PD) and analysed by an electrical spectrum analyser (ESA) in a zero-span mode.

A 10 km single-mode silica fibre is used as a sensing fibre. The peak Brillouin frequency (10.84 GHz) power trace is obtained with 1000 trace averages and illustrated in Figure 4.17(a). LabView has been developed to control and automate the ESA (Agilent- N9020A) to sweep the Brillouin frequencies and data collection. In order to obtain a three-dimensional spectral mapping, the frequencies are swept from 10.8 GHz to 10.9 GHz with a frequency step of 1 MHz and 1000 trace averages. The three-dimensional Brillouin spectrum obtained at room temperature (~25^{o}C) and strain-free is shown in Figure 4.17(b). A 100 m fibre kept in the oven at a 5 km distance and set a 65^{o}C temperature within the oven, while the rest of the fibre was at room temperature (~25^{o}C). Figure 4.18(a) shows the 65^{o}C temperature induced BFS at 5 km distance. Figure 4.18(b) is the top view of the Brillouin gain spectrum, the 65^{o}C temperature induced shift is found to be 44.25 MHz. The expected BFS value for 40^{o}C temperature change is 42.8 MHz (1.07 MHz/^{o}C). Therefore, the calculated error is 1.45 MHz, which corresponds to the temperature error of 1.35^{o}C. The temperature measurement error is about 3.4% of the

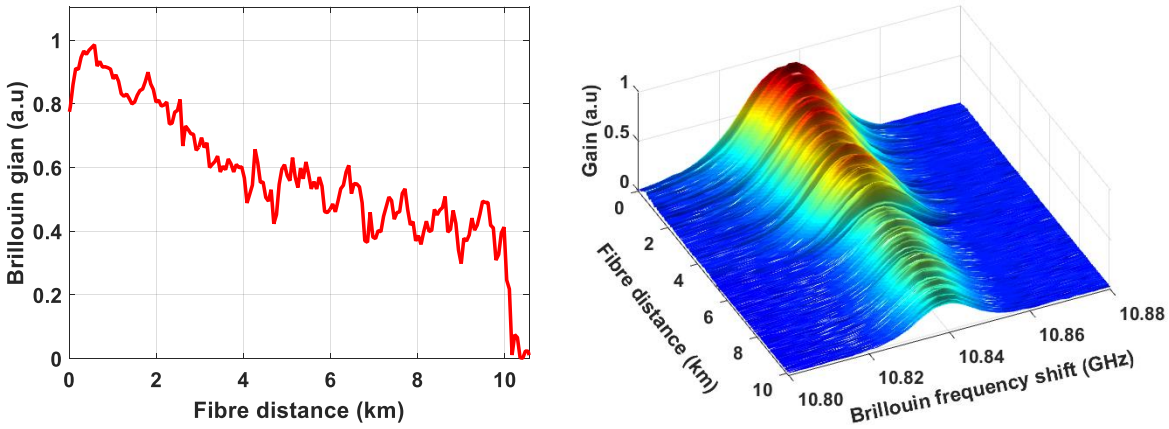

(a) (b)

Figure 4.17. (a) Peak Brillouin frequency power trace over the fibre distance (b) obtained three-dimensional spectral mapping

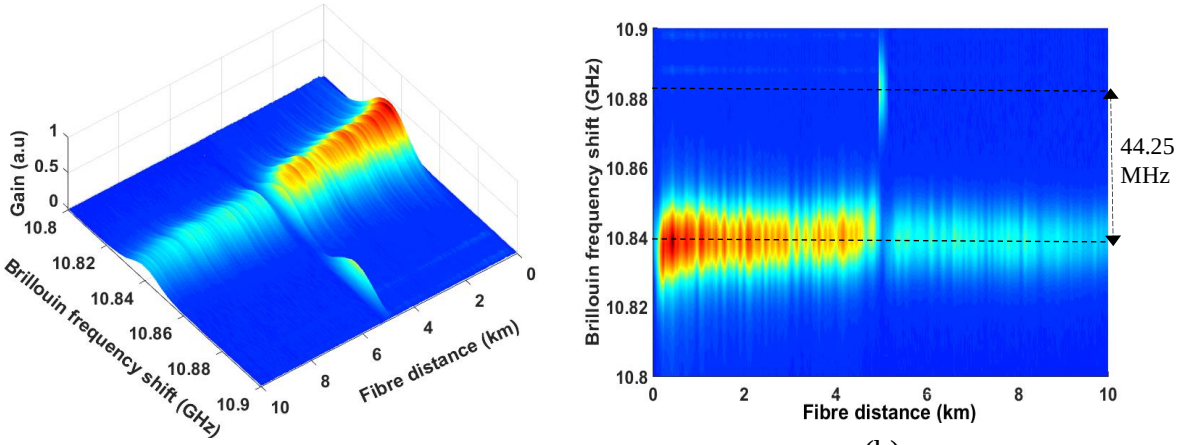

(a) (b)

Figure 4.18. Three-dimensional spectral mapping of 100 m heated section at 5 km distance (a) temperature induced frequency shift (b) top view

expected value. However, for temperature monitoring of the rail-track requires higher sensing range and much more accurate measurement even less than the 1% error, in order to avoid the false alarms [154, 155].

Polarization noise is one of the major noises source in BOTDR system, which significantly influences the beat signal amplitude fluctuations as shown in Figure 4.18. The measurement accuracy significantly reduces by the polarization noise. When the polarization state of the LO signal and detected Brillouin signal are identical to each other, the beat signal intensity would be at its maximum, whereas when the polarization states

are orthogonal to each other, the beat signal intensity would be at a minimum [156]. The polarization noise cannot be reduced by simple averaging.

In order to minimize the polarization induced signal fluctuations, several techniques have been proposed. Song *et al*. [157] used a polarization controller (PC) in LO path to generate two orthogonal polarizations periodically. However, randomizing the LO signal polarization states requires repeatable and accurate polarization controlling. Another widely used technique is a polarization scrambler, which scrambles the polarization states of the LO signal, and covers all polarization states equally [110, 111]. However, polarization scrambler is an active device, which induces additional noise to the system and is an expensive device. In addition, a complicated design is needed to make sure that the scrambled polarization states can cover all polarization states equally [158]. Therefore, in this research work a simple, low-cost passive depolarizer is employed to suppress the polarization noise significantly.

4.4.1 Operating Principle of Passive Depolarizer Technique

In heterodyne BOTDR system, the polarization state of both Brillouin signal and LO signal should be identical to each other, in order to reduce the beat signal fluctuations. Typically, the polarization state of the LO signal is stable, due to the small length of the fibre path and stable environment. Deventer *et al.* [156] confirmed that the polarization state of the backscattered Brillouin signal changes randomly along the fibre distance and is unpredictable. Due to the core nonuniform density and core size, the polarization state is not uniform along the fibre distance. The Brillouin signal over the fibre distance is given by [157],

$$E_B(z) = E_{Bx}(z)e_x + E_{By}(z)e_y \tag{4.6}$$

The Brillouin signal polarization state changes randomly in x and y directions along the fibre distance, z. If the polarization state of the LO signal maintains only in x or y

direction, only part of the Brillouin signal is maximized which leads to beat signal fluctuations. Therefore, the polarization of the LO signal is split into two orthogonal polarization states and described as [157],

$$E_{\mathrm{LO}}(t) = E_{\mathrm{LO}}(t)e_x + E_{\mathrm{LO}}(t+\Delta t)e_y \tag{4.7}$$

where Δt is the time delay between the two orthogonal polarization states. When the LO signal beats with the Brillouin signal, the resultant beat signal can be expressed as [158],

$$I_{\mathrm{beat}} = (E_{Bx} + E_{By})\, E_{\mathrm{LO}} \tag{4.8}$$

The LO signal distributes in two orthogonal polarization states, thus the beat signal fluctuations induced by the polarization noise can be eliminated effectively.

The schematic representation of the passive depolarizer is illustrated in Figure **4.19**. The polarization beam splitter (PBS) is used to split the input light polarization, which are orthogonal to each other. These two signals are coupled back through a polarization beam combiner (PBC). A polarization maintaining fibre (PMF) of 5 km is used as a delay fibre at one arm. In our experiments, the laser linewidth is 2 MHz, which corresponds to coherence length of 47.7 m [159]. Therefore, the delay fibre should be more than 47.7 m in order to eliminate the fixed phase relationship. Due to availability of only 5 km PMF pool in our laboratory, we used the delay fibre of 5 km. The time delay between the two orthogonal polarization signals eliminates the fixed phase relationship between them, when they are recombined using PBC. In this passive configuration, the LO signal is

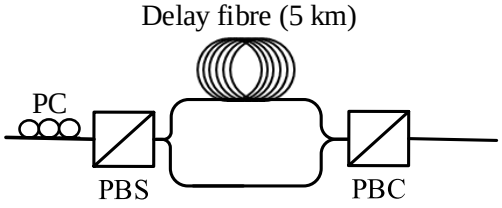

Figure 4.19. Schematic representation of passive depolarizer

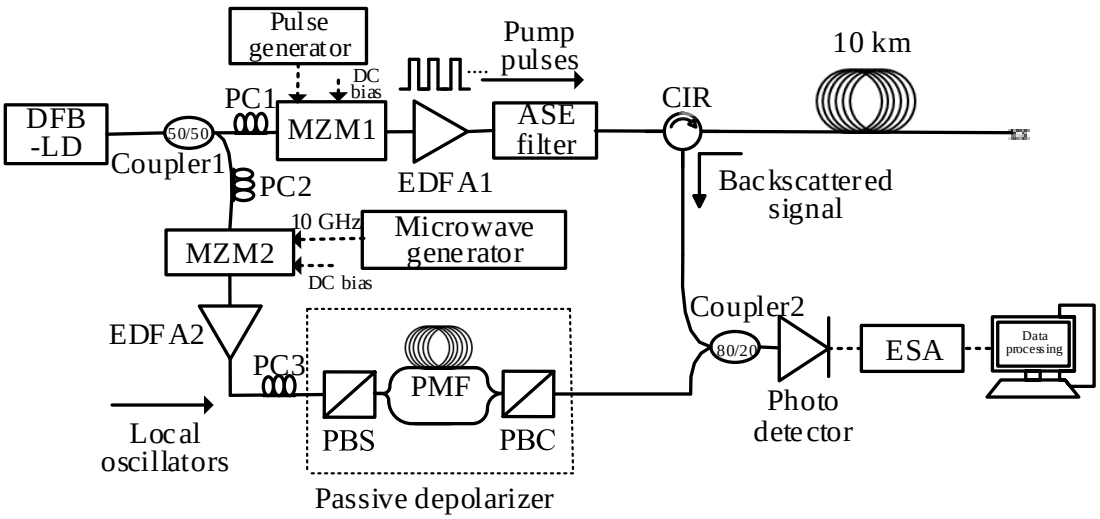

Figure 4.20. Experimental setup of modified BOTDR system

(DFB= distributed-feedback laser, PC= polarization controller, MZM=Mach-Zehnder modulator, EDFA=erbium doped fibre amplifier, ASE=amplified spontaneous emission, PBS=polarization beam splitter, PMF=polarization maintaining fibre, CIR=circulator, ESA=electrical spectrum analyser)

Table 4.2. System Parameters

Component	**Parameter**	**Value**
DFB laser	Linewidth	2 MHz
	Centre wavelength	1550.1 nm
	Output power	5 dBm
MZM 1 (FOCI 2.5)	Bandwidth	2.5 GHz
Pulse generator	Pulse width	100 ns
	Pulse amplitude	$4V_{pp}$
EDFA 1 (CALMAR, AMP-PM-16)	Gain	35 dB
	Noise figure	<5.5 dB (typ)
EDFA 2 (OptoSci, EDFA-1)	Gain	28 dB
	Noise figure	<5 dB (typ)
ASE filter (HJ Optronics)	Pass-band	1545-1565 nm
MZM 2 (Photline, MXAN-LN-20)	Bandwidth	20 GHz
	Modulation frequency	10 GHz
Microwave generator (Agilent, E8247C)	Bandwidth	20 GHz
Polarization maintaining fibre (Thorlabs, PM1550-HP)	Length	5 km
Photodetector (Thorlab, D400FC)	Bandwidth	1 GHz

composed of two orthogonal polarization signals, which significantly eliminates the beat signal fluctuations [160, 161].

The modified experimental setup of employing passive depolarizer in BOTDR system is illustrated in Figure 4.20. The system specifications are shown in Table 4.2. The pump signal is injected into the sensing fibre, which generates SpBS and detected at the same end. The backscattered SpBS signal beat with the LO signal, the resultant electrical beat signal having a frequency of about ~11 GHz, which requires the PD bandwidth higher than 11 GHz. The use of higher bandwidth PD will result in a higher noise equivalent power (NEP), which reduces the system accuracy. In addition, higher bandwidth electronic devices are needed for electrical signal processing. To avoid the use of such high bandwidth devices, an intensity MZM is often employed in LO path, while the sideband frequency shift is controlled by the RF microwave generator. Therefore, we employed an MZM in LO path to down-convert the backscattered Brillouin frequency. The LO signal is then modulated by the MZM 2, whose frequency is downshifted and upshifted by 10 GHz from the original frequency with two sidebands. Thereafter, the LO signal is fed into the passive depolarizer to suppress the polarization noise. The peak power before the depolarizer and after depolarizer is 5.2 dBm and 3.4 dBm, respectively. Therefore, the insertion loss of the depolarizer is 1.8 dB.

The polarization noise suppression using a depolarizer is confirmed experimentally. The peak Brillouin frequency power traces obtained with depolarizer and without

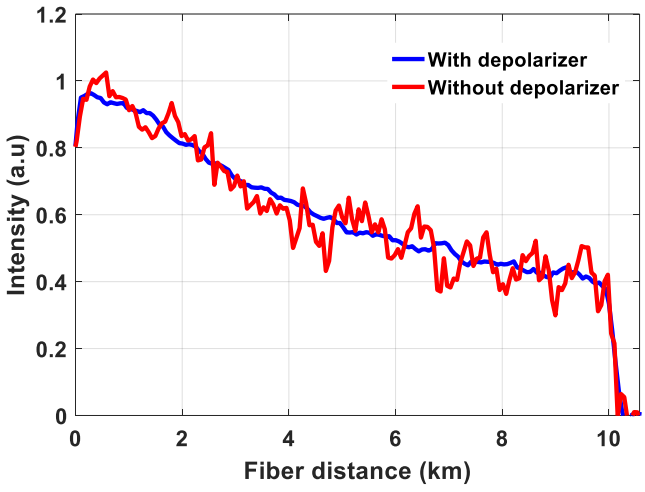

Figure 4.21. Peak Brillouin traces with depolarizer and without depolarizer

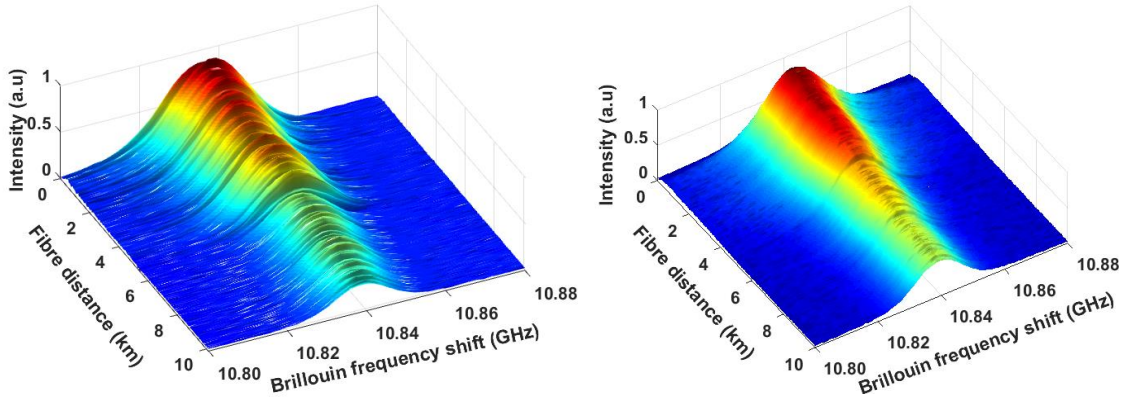

(a) (b)

Figure 4.22. Three-dimensional Brillouin gain spectral distribution (a) without depolarizer (b) with depolarizer

depolarizer is illustrated in Figure 4.21. For both the cases, 1000 trace averages are used. The three-dimensional spectral mapping with and without depolarizer is illustrated in Figure 4.22. The signal fluctuations induced by the polarization noise has been reduced significantly using a depolarizer. The 10 km sensing fibre composed of 5 km-3 km-2 km fibre pools, therefore from Figure 4.22(b), we can observe connection losses at 5 km and 8 km distance.

4.5 Experimental Demonstration of BOTDA System

In this section, the Brillouin optical time domain analysis (BOTDA) system, which is based on stimulated Brillouin scattering (SBS) is investigated experimentally. In BOTDA system, the launching pump power is limited by the presence of non-negligible nonlinearities in the sensing fibre, typically modulation instability (MI) and self-phase modulation (SPM) [162]. Therefore, the maximum pump power launched into the sensing fibre is limited to about 20 to 22 dBm [163, 164]. Above this power, the nonlinear effects reduce the system performance. Moreover, the counter-propagating probe power is also strictly limited to ~6 dBm by pump depletion [165].

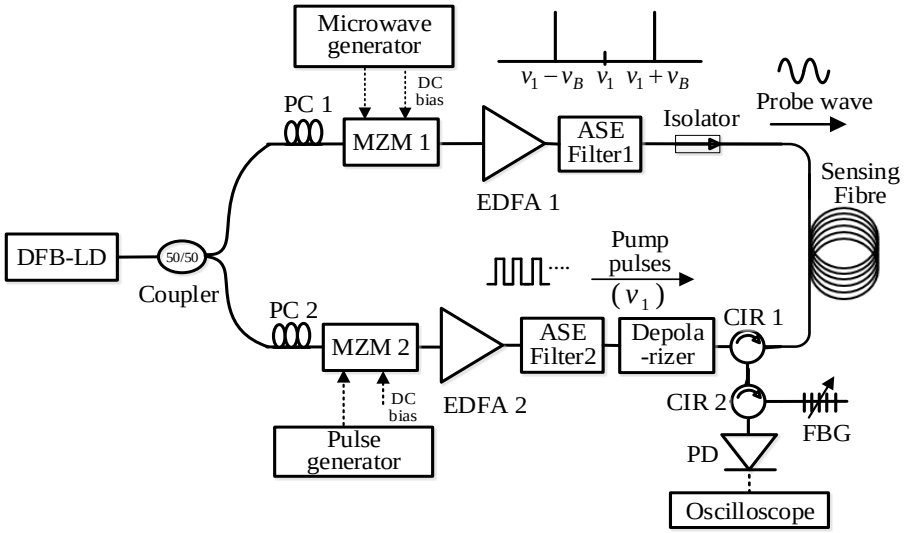

Figure 4.23. Experimental setup of BOTDA system

(DFB-LD= distributed feedback laser diode, PC=polarization controller MZM= Mach-Zehnder modulator, EDFA= erbium-doped fibre amplifier, ASE= amplified spontaneous emission, CIR=circulator, FBG= fibre Bragg grating, PD= photodetector)

The experimental setup of BOTDA system is illustrated in Figure 4.23. A DFB laser at 1550.1 nm was used as a light source. The output power of the DFB-LD is 5 dBm and split into two signals, namely, pump and probe signal using a 50/50 coupler. The PC was employed at the input of the MZM for obtaining the maximum optical power at the output of the MZMs. An MZM 2 which modulates the electrical pulses into optical pulses using a pulse generator. MZM 1 modulates the input signal at a frequency of sensing fibre BFS (10.88 GHz) in a carrier suppression mode, driven by an external microwave signal generator. Subsequently, the probe and pump signals are amplified by an erbium-doped fibre amplifier (EDFA). Adjusting the output power of the EDFAs, pump and probe powers are separately optimised at the sensing fibre input. The peak power of 20 dBm and the counter-propagating CW power, 6 dBm sent to the 50 km sensing fibre. The pulse width is set at 20 ns, corresponding to 2 m spatial resolution. The received backscattered signal is sent to the fibre Bragg grating (FBG) in order to remove the unwanted upper sidebands of the probe waves, Raleigh and Raman scattering components. The Brillouin signal is then detected by a photodetector (PD) and analysed using an oscilloscope.

4.5.1 Results Discussion

In SBS process, the pump energy transfer from a higher frequency to lower frequency components. Therefore, a part of the pump energy transfer to the probe signal lower sideband while they are counter-propagating each other within the fibre medium. This will lead to a pump power depletion. However, when we use two probe waves at a frequency of $\nu_1 - \nu_B$ and $\nu_1 + \nu_B$, the pump energy transfer to the lower frequency, it can be compensated by an energy transfer from the higher frequency probe to the pump. At the receiver, the higher frequency probe wave can be filtered out using an FBG.

Firstly, the MZM 1 has been characterize in order to generate a probe wave, which is same as the Brillouin frequency ($\nu_1 - \nu_B$) as shown in Figure 4.25. Adjusting the DC bias

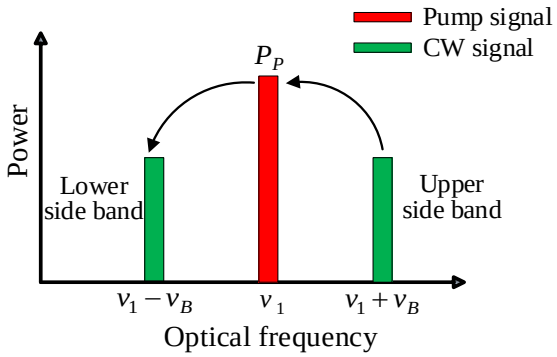

Figure 4.24. Schematic diagram of energy transfer process using two sidebands

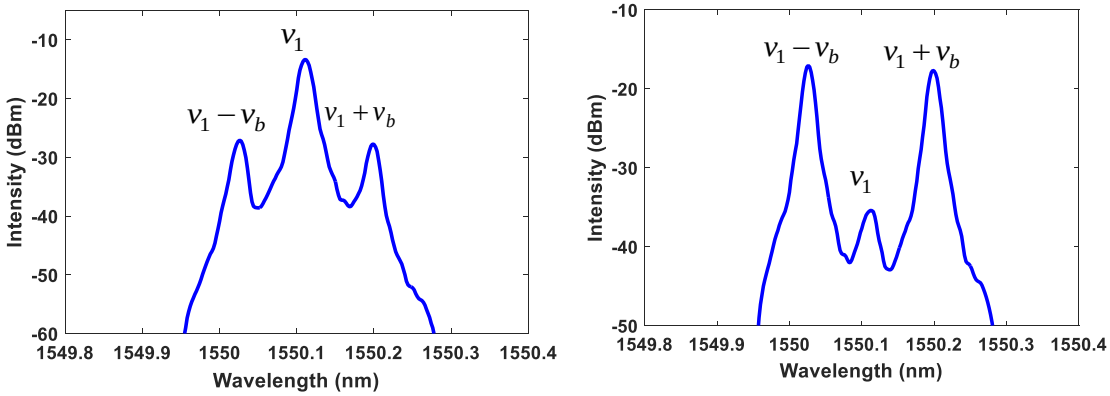

(a) (b)

Figure 4.25. The MZM output spectrum (a) DC bias at quadrature point (3.7 V) (b) DC bias at minimum biasing point (0.3 V)

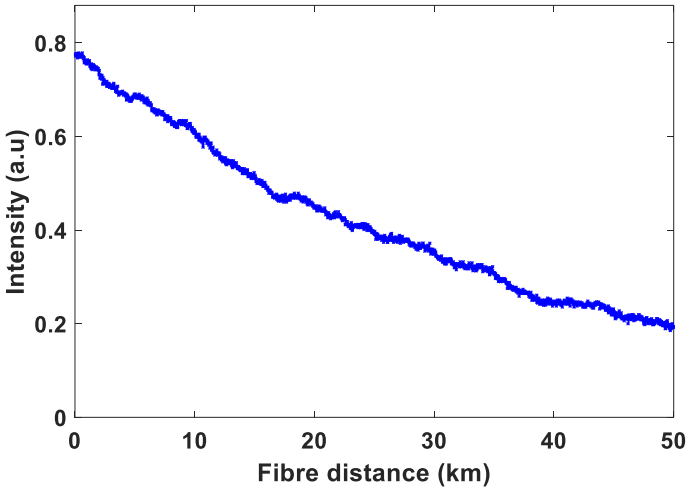

Figure 4.26. The peak Brillouin power trace over the fibre distance

of the MZM, the carrier signal can be suppressed as shown in Figure 4.25(b). The upper sideband ($\nu_1 + \nu_B$) helps to avoid the pump depletion as described in Figure 4.24. The time domain trace at peak Brillouin frequency (10.881 GHz) over the 50 km fibre distance is obtained and illustrated in Figure 4.26. In order to obtain a three-dimensional spectral mapping, the frequencies were swept from 10.83 GHz to 10.93 GHz, with a frequency step of 1 MHz with 1000 trace averages. The obtained Brillouin gain spectral distribution over the fibre length is shown in Figure 4.27. Using the Lorentz curve fitting to the measured raw BGS data, the BFS distribution along the 50 km sensing fibre is obtained and shown in Figure 4.27 inset.

A 4 m fibre at end of the sensing fibre was placed into the temperature oven, while the rest of the fibre at ambient room temperature (25^{o}C) and strain free. The temperature was set at 50^{o}C within the oven. The BFS distribution of the sensing fibre is shown in Figure 4.28. The 2 m spatial resolution has been obtained as shown in Figure 4.28.

The BOTDA system requires access to both ends of the sensing fibre with complex system implementation. After, careful discussions with Network Rail R&D team at Photonics Research Laboratory, Northumbria University, the most appropriate and convenient system for rail-track monitoring is BOTDR. This is because of single-end

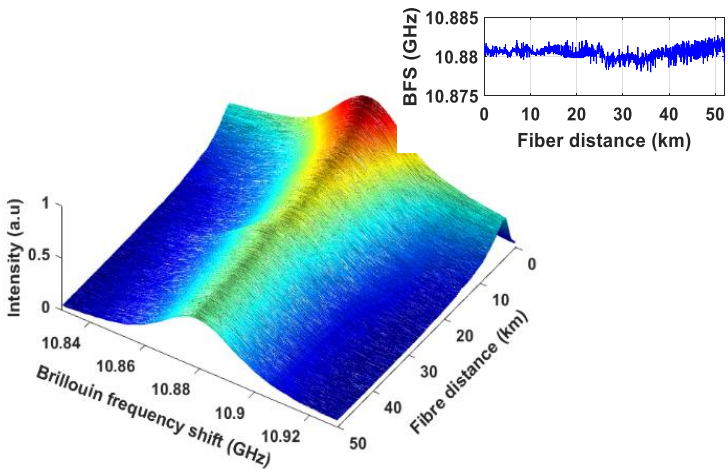

Figure 4.27. Brillouin gain spectrum over sensing fibre distance. inset: BFS distribution along the fibre distance

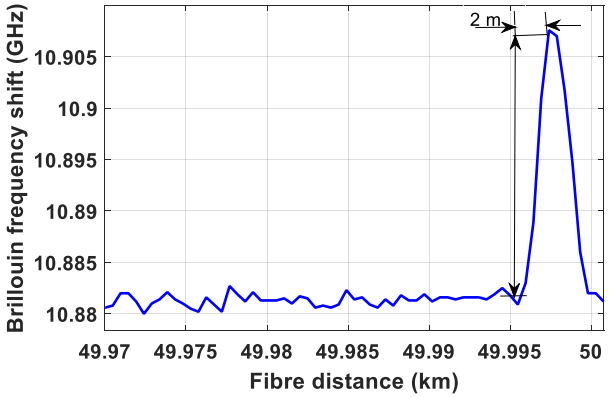

Figure 4.28. Brillouin frequency shift distribution under temperature effect on 4 m fibre at end of the sensing fibre (50 km)

access to the sensing fibre and easy integration of BOTDR system with existing data transmission fibre link. Therefore, the present research is focused on the optimisation and improvement of BOTDR system.

4.6 Evaluation of BOTDR Measurement Uncertainty

This section describes the theoretical and experimental evaluation of BOTDR measurement uncertainty. The key effects, such as the number of trace averages, Brillouin linewidth and sweep frequency step on BOTDR system measurement uncertainty is evaluated experimentally and compared with the theoretical analysis. In 2013, M. Soto *et*

al. [162] proposed an analytical expression and evaluated measurement uncertainty for a BOTDA system. Interestingly, no one evaluated the BOTDR measurement uncertainty in such a manner. Therefore, in order to better understand the impact of different factors (number of trace averages, Brillouin linewidth and sweep frequency step) have on BFS a series of experiments and analysis are considered.

4.6.1 Noise Impact on Brillouin Gain Spectrum

The major noise sources come from the laser are phase noise (also known as laser linewidth) and relative intensity noise (RIN). The laser linewidth is governed by the deviation of the laser light spectrum from a specified peak frequency. Whereas, the RIN is defined as the deviations of a laser output power, even at the constant DC current supply. These deviations originate from the spontaneous emission, which is completely random process within the laser cavity. In a distributed fibre sensor system, a highly coherent narrow linewidth laser source is essential for optimum sensing performance [166]. The commercial DFB laser sources have a -3 dB linewidth of usually a few MHz. In 2013, Yun-Qi *et al*. [166] investigated the influence of the laser linewidth on the performance of BOTDR system, which describes the finding that the linewidth of backscattered BGS is almost constant when the laser linewidth is less than the 3 MHz. Otherwise, the BGS linewidth broadens significantly when the laser linewidth greater than the 3 MHz. Therefore, for a better sensing performance, a narrow linewidth (< 3 MHz) laser source is essential. The effect of RIN can be minimised by selecting an appropriate averaging process [141].

Apart from the laser noise sources, the main noise sources in BOTDR system are polarization noise, ASE noise, thermal and shot noise. The polarization noise and ASE noise can be avoided using either polarization scrambler (PS) [167] or passive depolarizer

and ASE filter, respectively. The mean square of the thermal noise $\left(\langle i_{\text{th}}^2 \rangle\right)$ and the shot noise $\left(\langle i_{\text{sh}}^2 \rangle\right)$ can be expressed as [168],

$$\langle i_{\text{th}}^2 \rangle = \frac{4kTB}{R_L} \tag{4.9}$$

$$\langle i_{\text{sh}}^2 \rangle = 2qR_D BP_B(t)P_{LO} \tag{4.10}$$

where k is the Boltzmann constant, T is the photodetector operating temperature in Kelvin, B is the bandwidth of the photodetector, R_L is the load resistance and q is the elementary charge. It is important to mention that, the major shot noise comes from the LO signal power, as detected Brillouin power much weaker than the LO signal power. As a result, the Brillouin power, $P_B(t)$ can be negligible in equation (**4**.**10**).

Therefore, the total electrical noise power can be expressed as,

$$\begin{aligned}\sigma^2 &= \langle i_{\text{th}}^2 \rangle + \langle i_{\text{sh}}^2 \rangle + < i_{\text{E-noise}}^2 > \\ &= \frac{4kTB}{R_L} + 2qR_D BP_{LO} + < i_{\text{E-noise}}^2 >\end{aligned} \tag{4.11}$$

The term $< i_{\text{E-noise}}^2 >$ is the total noise power from the electronic devices, for instance, electrical spectrum analyser.

In BOTDR systems, the received photocurrent can be expressed as [169],

$$I_{ph} = 2R_D\sqrt{P_B(t)P_{LO}}\,\cos(v_B - v_{LO})t\cos\theta(t) \tag{4.12}$$

where R_D is the photodetector responsivity, $P_B(t)$ is the peak Brillouin signal power at time t, P_{LO} is the peak LO signal power, $v_B - v_{LO}$ is the frequency difference between the Brillouin signal and LO signal, θ denotes the polarization difference of the Brillouin signal and LO signal.

Furthermore, the SNR of the BOTDR system can be expressed as [170],

$$\mathrm{SNR}(t) = \frac{2R_D^2 \cos^2(\theta) P_B(t) P_{LO} \sqrt{N_{\mathrm{avg}}}}{(4kTB / R_L) + (2qR_D P_{LO}\, B) + \cos^2(\theta) + < i_{\mathrm{E-noise}}^2 >} \tag{4.13}$$

Assuming the polarization states of both Brillouin signal and LO signal are identical to each other (θ=0, a passive depolarizer is used throughout this research), and sufficient trace averages are used (N_{avg}>1000), then the SNR can be modified as,

$$\mathrm{SNR}(t) = \frac{2R_D^2 P_B(t) P_{LO}}{(4kTB / R_L) + (2qR_D P_{LO}\, B) + < i_{\mathrm{E-noise}}^2 >} \tag{4.14}$$

The backscattered signal power is relatively weak and the power before the photodetector is usually low [171]. Therefore, it is important to mention, at the detection the major noise source or dominant noise source is thermal noise, as the shot noise contribution is considerably small. The quantification of local BGS is important in order to estimate the strain and temperature measurement accuracy and resolutions. The extracted BGS at one fibre location is shown in Figure 4.29. The peak BFS, intensity and Brillouin linewidth are estimated by the curve fitting procedure. In general, the most commonly used curve fittings are Lorentz, Voigt and quadrature least-square fitting [127]. The estimation accuracy of peak BFS leads to better measurement accuracy. However, the measurement accuracy depends on the noise of the measured BGS, Brillouin linewidth, number of trace averages and sweep frequency step. In [162], an

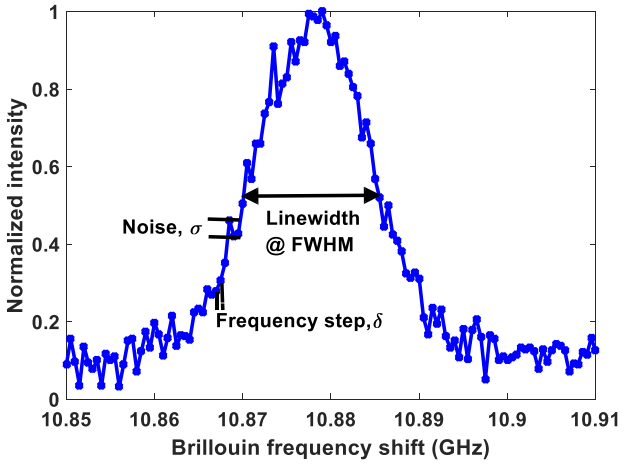

Figure 4.29. The extracted BGS at one fibre location

analytical expression was developed for estimation of the BFS uncertainty for the first time. The estimated BFS uncertainty can be expressed as [162],

$$\sigma_v(z) = \frac{1}{\mathrm{SNR}(z)} \sqrt{0.75.\delta.\Delta\nu_B} \tag{4.15}$$

where $\mathrm{SNR}(z)$ is the signal-to-noise ratio at distance z, δ is the sweep frequency step and $\Delta\nu_B$ is the Brillouin linewidth at FWHM. This expression is subject to quadrature curve fitting and the sweep frequency step much less than the Brillouin linewidth, i.e., $\delta << \Delta\nu_B$. The detailed derivation of equation (4.15) can be found in [162]. For a 10 km sensing fibre, while using quadrature curve fitting, the BFS uncertainty is validated both theoretically and experimentally using the different factors.

The measured SNR over the fibre distance for different input pump powers is shown in Figure 4.30. For an optimised input power of 18 dBm, the obtained SNR at end of the sensing fibre is 9.1 dB. For the input power of 16 dBm and 14 dBm, the measured SNR at end of the sensing fibre is 6.5 dB and 1.95 dB, respectively. Moreover, the measured BGS linewidth (FWHM) at end of the sensing fibre is 32.1 MHz. For a reliable comparison, the optimised input pump power (18 dBm) (has the best SNR and below the

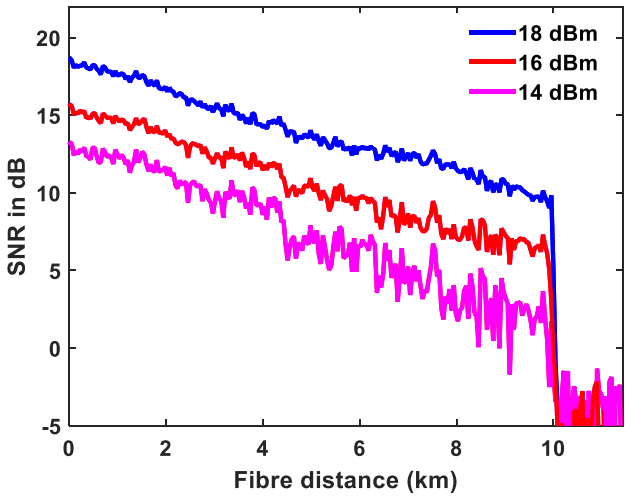

Figure 4.30. The measured SNR over the 10 km fibre distance for various input pump powers (14, 16 and 18 dBm)

threshold level), which has an SNR value of 9.1 dB and the linewidth of 32.1 MHz is used for all the theoretical measurement analysis.

4.6.2 The Different Key Factors Impact on BFS Uncertainty

The different key factor effects on BOTDR measurement accuracy, such as a number of trace averages, Brillouin linewidth and sweep frequency step is evaluated experimentally and compared with the theoretical analysis. The experimental setup of BOTDR system for evaluation of BFS uncertainty is shown in Figure **4.31**.

Firstly, the effect of number of trace averages on BFS uncertainty is evaluated. The number of trace averages dependence on the BFS uncertainty described as [162],

$$\sigma_v(z) = \frac{1}{\sqrt{N_{\text{avg}}}} \tag{4.16}$$

where N_{avg} is the number of trace averages, which follows an SNR proportional to the $\sqrt{N_{\text{avg}}}$. The BFS uncertainty is estimated along the 10 km sensing fibre with different trace averages. Using an 18 dBm input pump power, 100 ns pulse width and a sweep frequency step of 1 MHz, the three-dimensional BGS constructed for different trace averages. The BFS profile along the fibre distance is obtained with a quadrature curve

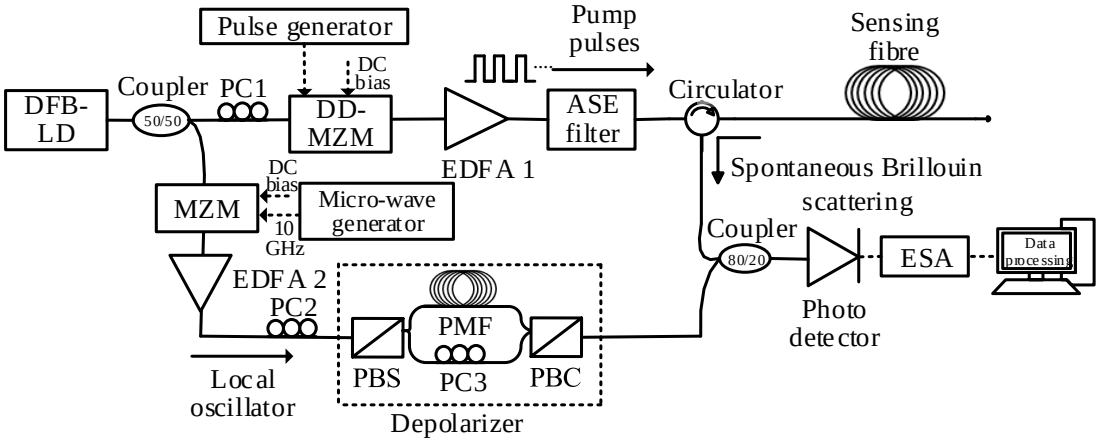

Figure 4.31. Experimental setup of BOTDR system for BFS uncertainty evaluation (DFB=distributed-feedback laser, PC= polarization controller, MZM=Mach-Zehnder modulator, EDFA=erbium doped fibre amplifier, DD-MZM=dual drive-MZM, ASE=amplified spontaneous emission, PBS=polarization beam splitter, PBC=polarization beam combiner, PMF=polarization maintaining fibre, ESA=electrical spectrum analyser)

fitting and illustrated in Figure 4.32(a). Calculating the standard deviations of the measured BFS, the BFS uncertainty can be estimated over the fibre distance [162]. Moreover, the linear curve fitting was used for the measured data and illustrated in Figure 4.32(b). As shown in Figure 4.32(b), the BFS uncertainty at the end of the 10 km fibre is 1.17 MHz for 50 averages and 0.25 MHz for 1000 averages. The theoretical BFS uncertainty is analysed using equations (4.15) and (**4.16**) for different trace averages and

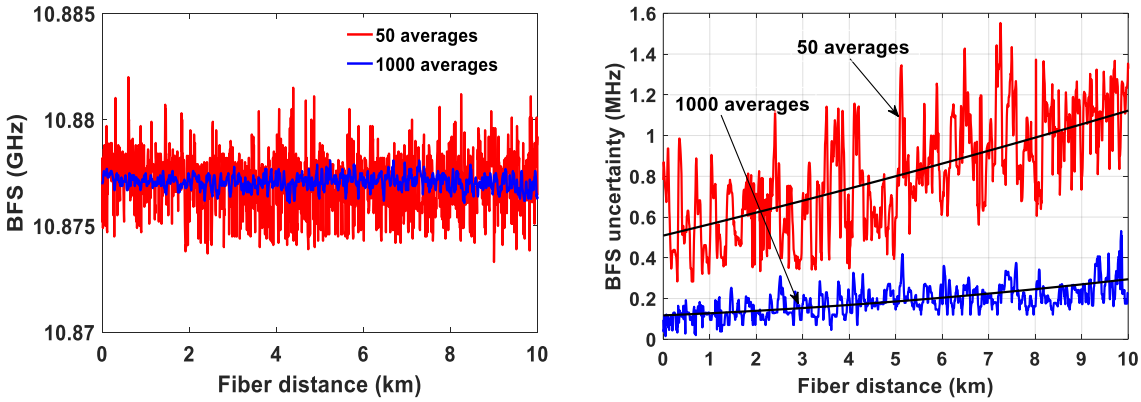

(a) (b)

Figure 4.32. (a) The BFS distribution over the fibre distance and (b) standard deviations of 50 and 1000 trace averages

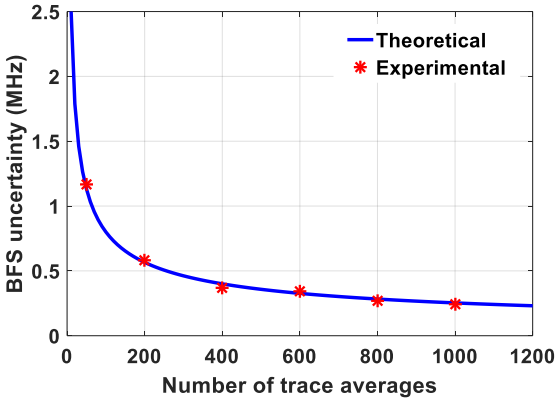

Figure 4.33. The measured BFS uncertainty at end of the sensing fibre.

(The theoretical analysis performed using equation (**4.15**), with $\Delta\nu_B$ =32.1 MHz, δ =1 MHz and the SNR is used same as the experimental value (9.1 dB))

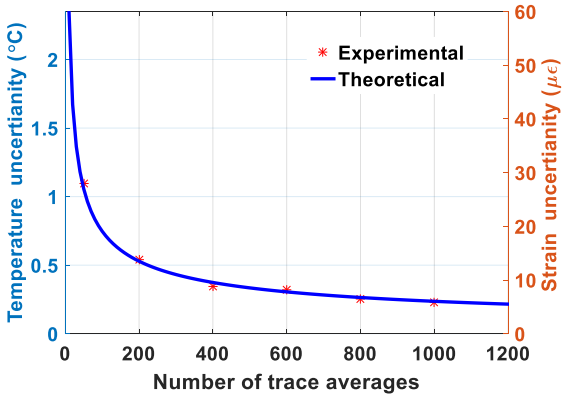

Figure 4.34. The calibrated strain and temperature uncertainty at end of the 10 km sensing fibre for different trace averages.

(The calibrated strain and temperature coefficient of the fibre is 0.05 MHz/με and 1.07 MHz/^{o}C, respectively)

compared with the experimental values, as shown in Figure **4.33**. The measured BFS uncertainty is calibrated with sensing fibre strain (0.05 MHz/με) and temperature (1.07MHz/^{o}C) coefficients to estimate the strain and temperature uncertainties for different trace averages and shown in Figure 4.34.

Thereafter, the BGS linewidth, $\Delta\nu_B$ impact on BFS uncertainty is evaluated theoretically (using equation (4.15)) and experimentally as shown in Figure **4.35**. In the experiment, the BGS linewidth is changed with different pulse widths, as the spatial resolution is changed then the local BGS linewidth varies accordingly [172]. For various spatial resolutions, the same SNR (9.1 dB) is compensated for all the measurements with varying the input pump power for a valid comparison. For three-dimensional spectral mapping, the sweep frequency step is 1 MHz and 1000 trace averages are used. The curve fitting is performed for each individual measurement and calculated standard deviations of measured BFS along the fibre distance. As shown in Figure **4.35**, the BFS uncertainty at end of the sensing fibre is calculated and compared with theoretical values at a same

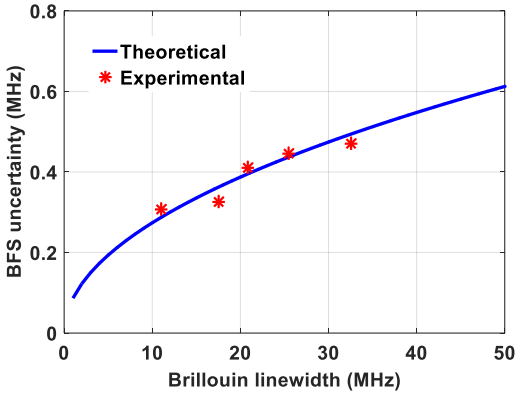

Figure 4.35. The measured BFS uncertainty at the end of the sensing fibre with 1000 trace averages and SNR=9.1 dB. (The theoretical analysis performed using equation (**4.15**) with δ =1 and SNR=9.1 dB)

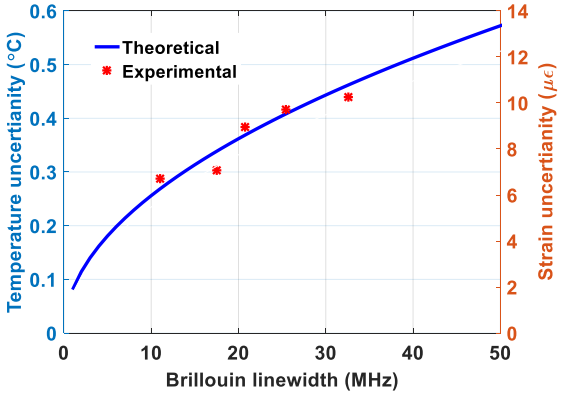

Figure 4.36. The calibrated strain and temperature uncertainty at end of the 10 km sensing fibre for different BGS linewidth. (The calibrated strain and temperature coefficient of the fibre is 0.05 MHz/με and 1.07 MHz/^{o}C, respectively)

set of conditions. The calibrated strain and temperature uncertainties at end of the sensing fibre are illustrated in Figure 4.36.

Finally, in order to evaluate the impact of the sweep frequency step δ, the Brillouin spectral profile over the fibre distance is obtained with different sweep frequency steps at a fixed trace averages of 1000 and linewidth of $\Delta\nu_B$ =32.1 MHz. The theoretical curve as shown in Figure **4.37** is calculated using equation (4.15) with $\Delta\nu_B$ =32.1 MHz and SNR=9.1 dB. The measured BFS uncertainty at the end of the sensing fibre for different sweep frequency step is shown in Figure **4.37**. The small sweep frequency step minimizes the BFS uncertainty as more data points are involved in the curve fitting procedure. As shown in Figure **4.37**, the frequency step increases the BFS uncertainty grows following a $\sqrt{\delta}$, relationship, which is in good agreement with theoretical analysis, $\sigma_\nu(z)=\sqrt{\delta}$ as per equation (4.15). The calibrated strain and temperature uncertainties at the end of the sensing fibre are illustrated in Figure 4.38.

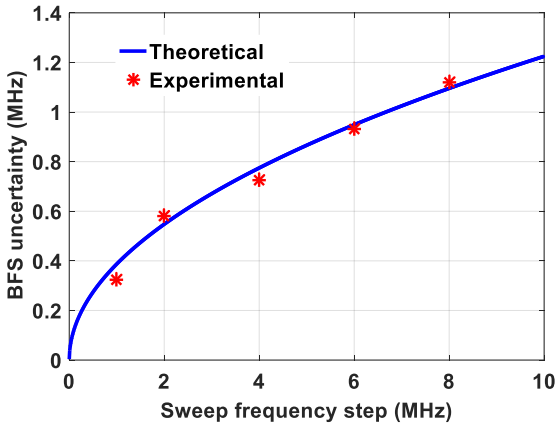

Figure 4.37. The measured BFS uncertainty at the end of the sensing fibre with 1000 trace averages and SNR=9.1 dB. (The theoretical analysis performed using equation (**4.15**) with $\Delta\nu_B$ =32.1 MHz and SNR=9.1 dB)

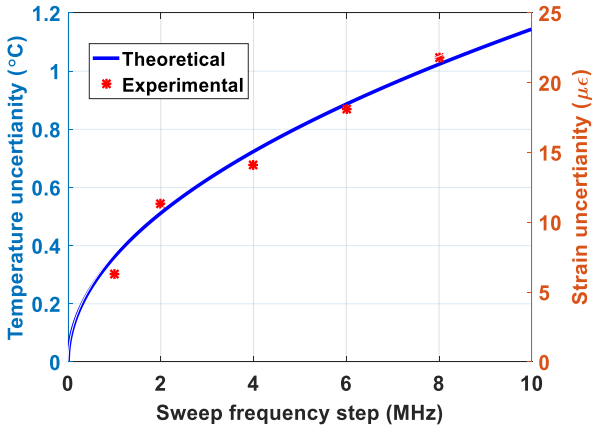

Figure 4.38. The calibrated strain and temperature uncertainty at end of the 10 km sensing fibre for different sweep frequency step. (The calibrated strain and temperature coefficient of the fibre is 0.05 MHz/με and 1.07 MHz/°C, respectively)

4.7 Factors Limiting the Performance of BOTDR System

The previous section discusses the different key factors, such as a number of trace averages, Brillouin linewidth and sweep frequency step impact on the BFS uncertainty. This section describes the several aspects which limits the BOTDR system performance. The fundamental limitations of the BOTDR system, such as noise sources, non-negligible nonlinear effects (which limits the input pump power), fibre loss and weak backscattered Brillouin signal. The fibre loss makes further decreases the Brillouin signal intensity. In order to compensate the fibre loss and strengthen the Brillion signal, high pump power has to be launched. However, increasing the pump power alone cannot compensate the fibre loss, due to fibre nonlinear effects that put a threshold on input pump power.

4.7.1 Major Noise Sources

The undesirable noise sources degrade the sensor system performance. Typically, the noise sources are a combination of the optical and electrical noise. The electrical noise associated with the detection system at the receiver, such as thermal noise, shot noise and noise from the electronic devices (RF amplifier, spectrum analyser). The optical noise sources are relative intensity noise (RIN), polarization noise, and amplified spontaneous emission (ASE) noise[2]. Among the all noise sources, the dominant noise source is polarization noise, which significantly influences the Brillouin signal intensity fluctuations. EDFAs are often employed in Brillouin based sensors to get the required launching pump power into the sensing fibre. Typically, the ASE noise bandwidth is ~5 nm which generates noise signals through various mixing processes, for instance with pump and Raleigh signals, ASE beat with itself (ASE-ASE) and with the LO signal (ASE-

[2] The ASE noise occurs only when the optical amplifiers are used in the system

LO). Apart from for the RIN, the optical noise sources cannot be reduced by the simply signal averaging.

4.7.2 Power Depletion due to Attenuation

If only the fibre attenuation is considered, then the pump pulse propagating along the fibre will be attenuated by a factor of α. Due to the requirement of optical amplification in the sensor system and make use of low loss window, the pump wavelength is usually optimised for the 1550 nm (third window) wavelength. For a single-mode silica fibre, the attenuation is about 0.2 dB/km at a 1550 nm wavelength. However, operating at this optimised low loss window and the round trip fibre loss (~0.4 dB/km) is unavoidable. For instance, using a 50 km sensing fibre, the Brillouin signal is reduced by a 20 dB. The strength of the backscattered Brillouin signal depends on the injected pump power. For a longer fibre distance, the Brillouin signal is difficult to detect by the receiver. In order to increase the Brillouin signal power, a higher pump power has to be coupled into the fibre. However, we cannot indefinitely increase the pump power above the certain nonlinear threshold level. The following section briefly explains the sensing fibre nonlinear effects originates from the higher injected pump power.

4.7.3 The Key Nonlinear Effects in Sensing Fibre

In Brillouin based distributed fibre sensors, the strength of the backscattered signal is proportional to the input pump pulse energy. The pulse energy depends on the pulse width, but the desired spatial resolution limits the pulse width. The maximum launched pump pulse power is governed by the onset of non-negligible nonlinear effects. The nonlinear effects act to distort the pump pulse spectral profile along the fibre distance. The potential nonlinear effects in BOTDR system are stimulated Brillouin signal (SBS), stimulated Raman scattering (SRS), and self-phase modulation (SPM). The SBS and SRS effects result in a rapid depletion of the pump power, thus limiting the sensing

performance [162]. In order to avoid such nonlinear effects, the pump power should be below the certain nonlinear threshold. Among all the nonlinearities, the SBS has the lowest threshold value. Generally, within the distributed fibre sensor community, the SBS threshold is defined as the point when the backscattered Brillouin peak power equals to the power at the output of the fibre [25]. The threshold power for SBS and SRS can be expressed as [25],

$$P_{th}^{SBS} \approx \frac{21k_p A_{eff}}{g_B L_{eff}} \tag{4.17}$$

$$P_{th}^{SRS} \approx \frac{16k_p A_{eff}}{g_R L_{eff}} \tag{4.18}$$

where A_{eff} is the effective core area (mode field area) of the fibre, k_p is the polarization constant, g_B is the Brillouin gain coefficient, L_{eff} is the effective interaction length. The Brillouin and Raman gain coefficients are 5×10^{-11} m/W [46] and 7×10^{-14} m/W [173] at a 1550 nm pump wavelength, respectively. The calculated Brillouin gain coefficient is subject to when the laser linewidth is smaller than the Brillouin linewidth [174]. The SBS and SRS threshold is approximately 40 mW to 60 mW (16-18 dBm) and ~400 to 600 mW (26-27.8 dBm), respectively [162, 175, 176]. Therefore, the lowest nonlinear threshold is SBS, which limits the maximum input pump power in BOTDR system.

In order to better understand the SBS nonlinearity of the sensing fibre, an experimental analysis has been performed. Figure 4.39 illustrates the measured peak Brillouin frequency power distribution along the 25 km fibre distance for different input pump powers. In the case of input pump power, 18 dBm (blue line in Figure 4.39), which is below the SBS critical power, it is possible to observe the exponential power distribution all along the fibre distance. However, as the pump power increases to 20 dBm (red line in Figure 4.39), the signal power decreasing rate is significantly faster than that of 18dBm

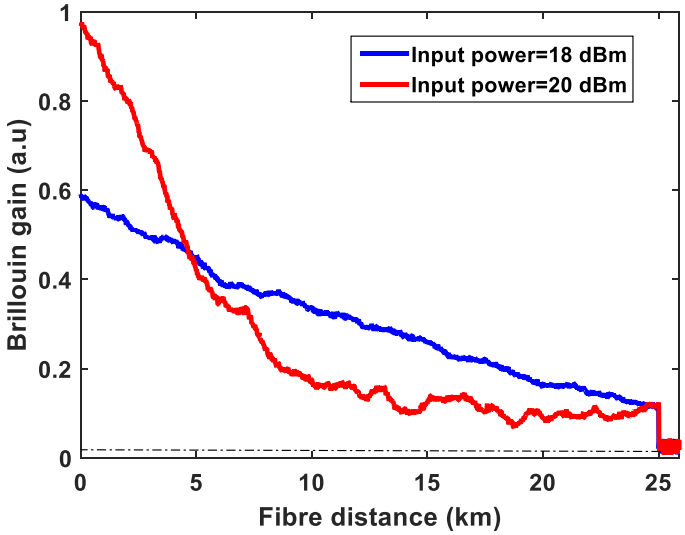

Figure 4.39. Measured peak Brillouin power traces for different pump powers in BOTDR system

case, which is due to pump depletion induced by the SBS nonlinearity. The high gain at the starting of the fibre has nothing to do with the sensing range. In this case, the pump power transfers most of its power to the Brillouin signal, as a result the Brillouin signal has a high gain at the starting of the fibre. We obtained a maximum gain until 5 km fibre distance because of the high input pump of 20 dBm than the 18 dBm case. Indeed, it should be the low gain after the 5 km, which significantly affect the sensing range. Therefore, increasing the input pump power in the conventional BOTDR system above the certain nonlinear threshold cannot enhance the sensing performance.

After the SBS, another nonlinear effect limits the maximum pump power is modulation instability (MI). The MI or sideband instability leading to the generation of new sideband spectrums and eventually breakup the pump waveform into a train of pulses. The MI originates from the Kerr effect and anomalous dispersion within the fibre [177]. The MI is the main nonlinear parameter, which limits the maximum pump power in the BOTDA system, where the SBS nonlinearity is compensated by a counter-propagating continuous wave. Increasing the input pump power above the MI threshold,

the sensing system performance degrades significantly. The threshold level of MI is described as [121],

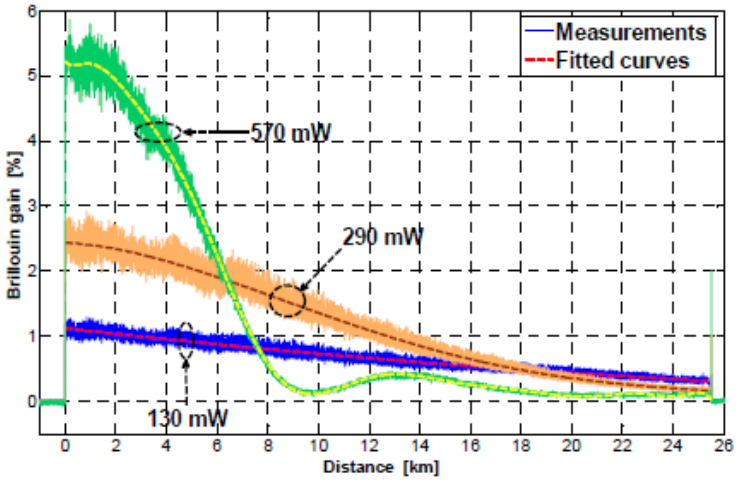

Figure 4.40. Peak Brillouin gain distribution over 25 km fibre for different input pump powers in BOTDA system [121]

$$P_{th}^{MI} = \frac{4}{2\gamma L_{eff}} \tag{4.19}$$

where γ is the fibre nonlinear coefficient, which is approximately 1.8 W^{-1}/km for standard single-mode silica fibre. M. Alem *et al*. [121, 165] investigated the BOTDA system MI threshold for a 25 km fibre, the obtained value is about 100 mW to 130 mW. Figure 4.40 shows the Brillouin peak power distribution in BOTDA along the 25 km fibre for three different input pump powers. For the case of the lowest input power of 130 mW, it is possible to observe the natural exponential power decay by the fibre attenuation. However, as the pump power increases, the Brillouin power distribution changes rapidly due to the onset of MI.

Another nonlinear effect in the sensing fibre is SPM. SPM is induced by the pulse phase change due to the refractive index dependence on the optical intensity. The SPM induces the pulse spectral broadening, as a function of effective fibre length and optical intensity. At a 1550 nm pump wavelength, the Raleigh and Brillouin spectral lines are

relatively close (~11 GHz), therefore the spectral broadening exceeding ~11 GHz is undesirable. The SPM threshold can be expressed as [25, 178],

$$P_{th}^{SPM} \approx \frac{\varphi_{\max}}{\gamma L_{eff}} \tag{4.20}$$

where $\varphi_{\max}$ is the maximum pulse phase shift, γ is the nonlinear coefficient and can be expressed as [178],

$$\gamma = \frac{2\pi n_2}{\lambda_p A_{eff}} \tag{4.21}$$

where n_2 is the nonlinear refractive index and λ_p is the pump wavelength. The Brillouin linewidth broadening is proportional to the maximum phase shift. Considering the values of n_2 =2.2×10^{-20} m^2/W, A_{eff} =80 μm^2 and λ_p =1550 nm, the nonlinear coefficient, γ is equivalent to ~1.1 W^{-1}/km [178] and for a 50 km sensing fibre and pulse width greater than 30 ns, the SPM threshold power is more than 1.5 W. Therefore, in Brillouin based distributed fibre sensor system, the nonlinear threshold level, which limits the maximum pump is SBS (16-18 dBm) for BOTDR and MI (20-22 dBm) for a BOTDA system.

4.6 Summary

In this chapter, the BOTDR and BOTDA systems experimental investigation was presented and the major noise sources are discussed. The devices such as DFB laser and MZM are characterized. The strain and temperature effects on the Brillouin spectrum have been analysed. The obtained strain and temperature coefficients of the sensing fibre are 0.051 MHz/με and 1.07 MHz/^{o}C, respectively. Thereafter, a passive depolarizer is employed in order to suppress the polarization noise and its operating principle was discussed. The BOTDR and BOTDA systems are investigated experimentally using a passive depolarizer. Furthermore, the different key factor effects such as, number of trace

averages, Brillouin linewidth and sweep frequency step on BFS uncertainty is experimentally evaluated and compared with the theoretical analysis. Finally, the key nonlinear effects, which limits the sensing performance of BOTDR and BOTDA systems are discussed. We found that the lowest nonlinear threshold in BOTDR system is SBS, which limits the maximum input pump power of 16-18 dBm. Whereas, the lowest nonlinear threshold in BOTDA system is MI, which is nearly 20-22 dBm. Therefore, we need to find out the novel solution to overcome this restricted pump power. Since this chapter presents the experimental analysis of the BOTDR and BOTDA system and their limitations, the next chapter will focus on the optimisation techniques to improve the sensing performance for the BOTDR system.

Chapter 5

Optimisation of BOTDR system

5.1 Introduction

The previous chapter is solely dedicated to the experimental investigation of the conventional BOTDR system and its limitations. The primary constructed heterodyne BOTDR system at the University of Northumbria was reconfigured and optimised to improve the sensing performance. As a further improvement to the BOTDR system, this chapter describes a few techniques that have been employed in the conventional BOTDR system. The improvement techniques include, (i) employing a balanced photodetector in order to detect the weak Brillouin signal; (ii) cost-effective Brillouin ring laser for receiver bandwidth reduction; and (iii) inline EDFA for sensing range improvement.

5.2 Employing a Balanced Photodetector

The balanced photodetector (B-PD) consists of two well-matched photodiodes with a high transimpeadance amplifier (TIA). The B-PD output generate an voltage proportional

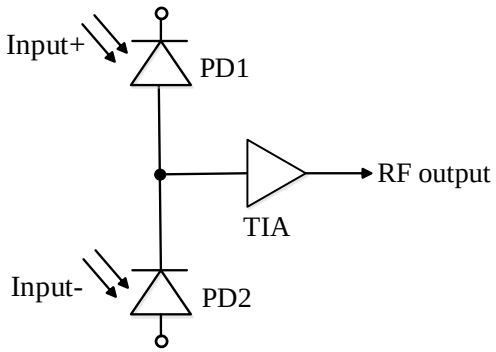

Figure 5.1. Functional block diagram of B-PD with transimpeadance amplifier

Figure 5.2. Thorlabs B-PD, PDB470C

to the difference between the two photocurrents from the two photodiodes, i.e., the difference between two optical inputs. For example, the higher voltage level after PD1 output is V_s and PD2 output is $-V_s$. Therefore, the voltage difference between the PD1 and PD2 is $V_s-(-V_s)=2V_s$, which is double the input voltage level. The functional block diagram of B-PD and Thorlabs B-PD (PDB470C, bandwidth: 400 MHz) are shown in Figure **5.1** and Figure 5.2, respectively. The two input optical signals (input+ and input-) are fed into the corresponding PD and the obtained photocurrents are subtracted. Eventually, the remaining current difference is amplified through the transimpeadance amplifier, while the subtraction resulting in the cancellation of common mode noise. The detected signal is normally doubled compared to the single PD of equal responsivity. The specifications of the Thorlabs B-PD (PDB470C) are listed in Table **5.1**.

The experimental setup of employing B-PD in BOTDR is shown in Figure 5.3. The upper branch signal is used for the pump and the lower branch signal is used for the LO signal. The PC is employed at the input of each MZM to achieve the maximum optical power at the output of the MZMs. The upper branch modulated with an MZM 1, which modulates the electrical pulses into optical pulses. Subsequently, the output signal is amplified by an erbium-doped fibre amplifier (EDFA). The amplified spontaneous emission (ASE) filter is used to eliminate the ASE noise from the EDFA. The LO signal

Table 5.1. Specifications of the Thorlabs B-PD (PDB470C)

Parameter	**Value**
Detector type	InGaAs
Operating wavelength	1200-1700 nm
Responsivity	0.95 A/W @1550 nm
Damage threshold power	10 mW
Bandwidth (3 dB)	400 MHz
Transimpeadance gain	10×10^3 A/W
Noise equivalent power (NEP)	8 pW/$\sqrt{\text{Hz}}$

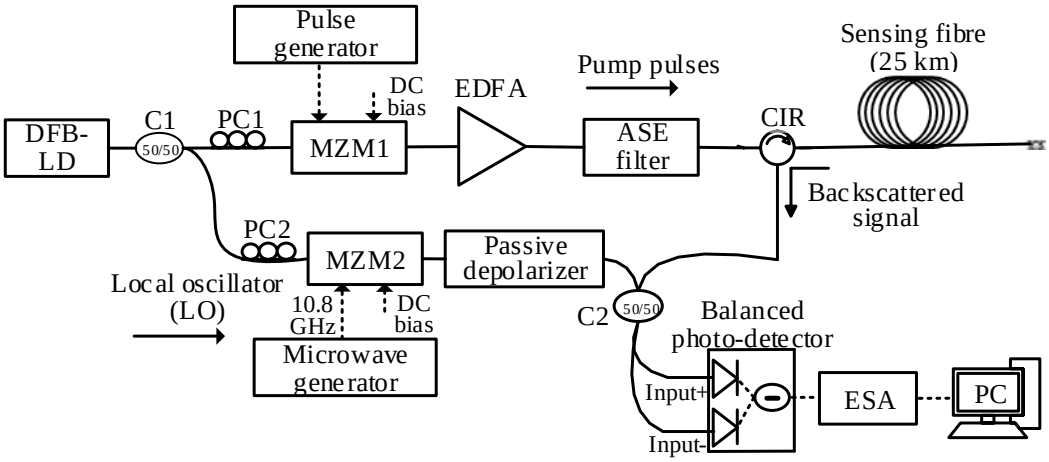

Figure 5.3. Experimental setup of BOTDR system employing balanced photodetector

(DFB-LD= distributed-feedback laser diode, C=coupler, MZM=Mach-Zehnder modulator, EDFA=erbium doped fibre amplifier, ASE=amplified spontaneous emission, CIR=circulator, ESA=electrical spectrum analyser)

is then modulated by the MZM 2, whose frequency is downshifted and upshifted by the 10.8 GHz from the original frequency with two sidebands in order to reduce the receiver bandwidth. Then, the MZM 2 output is sent through the passive depolarizer, for the polarization noise suppression. The two output signals from coupler 2 is fed into the positive and negative ports of the B-PD. The Brillouin gain spectrum (BGS) using a single PD and B-PD are shown in Figure 5.4. In both the cases, the input pump power and pulse width are same as 18 dBm and 100 ns, respectively.

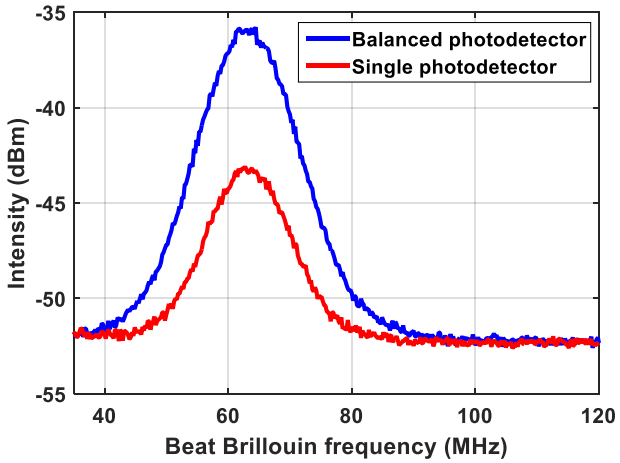

Figure 5.4. The Brillouin gain spectrums of single PD and B-PD

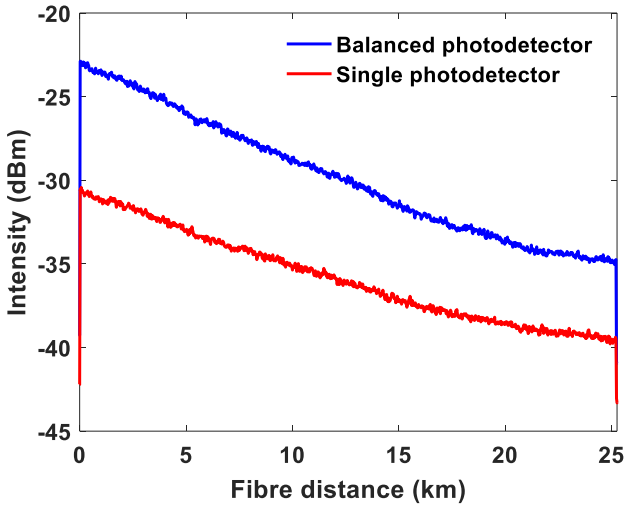

Figure 5.5. Peak Brillouin frequency traces along the fibre distance with single PD and B-PD

The noise floor (in the obscene of Brillouin gain) is found to be -53 dBm in both the cases. However, the Brillouin gain amplifies approximately doubled using B-PD. At a peak Brillouin frequency, the time domain traces are measured in both the cases using 25 km fibre and illustrated in Figure 5.5.

5.3 Employing a Brillouin Ring Laser

In heterodyne BOTDR system, the backscattered Brillouin signal beats with the LO signal. The resultant electrical beat signal has a frequency of about ~11 GHz (for silica-based fibres), which requires the bandwidth of a PD higher than the 11 GHz. The use of higher bandwidth PD will result in a higher noise equivalent power (NEP), which reduces the system accuracy [179]. In addition, the higher bandwidth electronic devices are needed for electrical signal processing. To avoid the use of such high bandwidth devices, an intensity MZM (as shown in Figure 5.3) is often employed in the LO path, while the modulated sideband frequency shift is controlled by the high bandwidth RF microwave generator. In this technique, the modulator needs to be precisely controlled and the system is more complicated. D. Iida *et al*. [180] proposed a simple, cost-effective Brillouin ring laser (BRL) and employed in the LO path instead of using expensive MZM and high

bandwidth microwave generator. Therefore, the receiver bandwidth can be reduced significantly in a cost-effective way.

The schematic representation of the BOTDR system using a BRL in LO path is illustrated in Figure 5.6.The laser signal at a frequency of ν_1 is divided into two propagation paths using a coupler 1, in which the upper path is used for the pulsed pump signal, whereas the lower path is used for the LO signal composed with a BRL [181]. An EDFA is used to pump the high peak power above the SBS threshold to obtain sufficient SBS power from the BRL fibre of 10 km. The obtained SBS output signal has a frequency of $\nu_1 - \nu_{B-LO}$. This Brillouin frequency depends on the core material doping concentration [100]. The measured BRL Brillouin gain spectrum (BGS) has a peak frequency of 10.77GHz with a narrow linewidth (full width at half maximum (FWHM)) of 5.2 MHz as shown in Figure 5.7. The measured BRL optical spectrum is illustrated in Figure 5.7 inset. The BRL peak power can be easily controlled using an EDFA. The detected beat Brillouin frequency is down-shifted in the order of few MHz, i.e., $\nu_B - \nu_{B-LO}$. For instance, if the sensing fibre BFS is, ν_B =10.88 GHz and the BRL's BFS is, ν_{B-LO} =10.77 GHz, the resultant electrical beat frequency is, $\nu_B - \nu_{B-LO}$ =110 MHz.

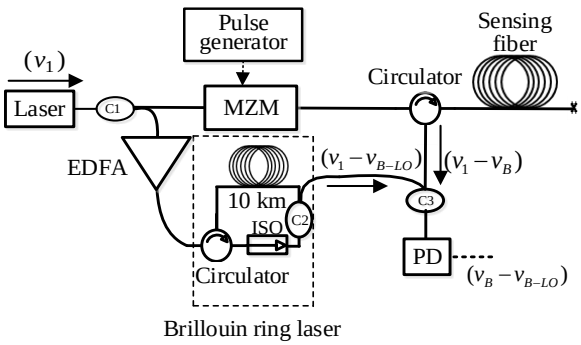

Figure 5.6. Schematic representation of Brillouin ring laser based BOTDR

(C=coupler, EDFA=erbium doped fibre amplifier, MZM=Mach-Zehnder modulator, ISO=isolator, PD=photodetector)

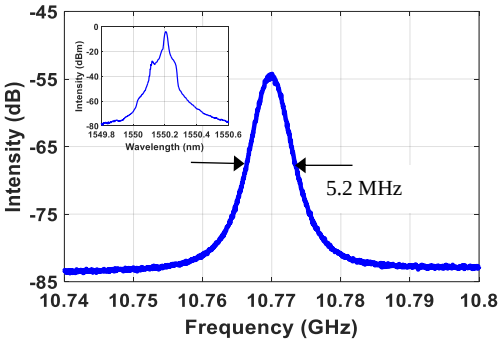

Figure 5.7. The measured Brillouin gain spectrum of Brillouin ring laser (BRL). (inset: Measured optical spectrum of BRL output)

The measured peak Brillouin frequency (at 110 MHz) power traces are illustrated in Figure 5.8. For a reliable comparison, in both cases, the input pump power and pulse width are set same as 18 dBm and 100 ns (corresponds to 10 m spatial resolution), respectively. From Figure 5.8, no improvement in Brillouin intensity over the fibre distance using the BRL. The reason of employing BRL in LO path is for system simplification. The three-dimensional spectral mapping where the frequencies were swept from 60 to 160 MHz with a step of 1 MHz and 2000 trace averages are illustrated in Figure 5.9. In this configuration, the BRL is composed with a simple implementation, and the bandwidth of PD and electronic devices can be reduced significantly.

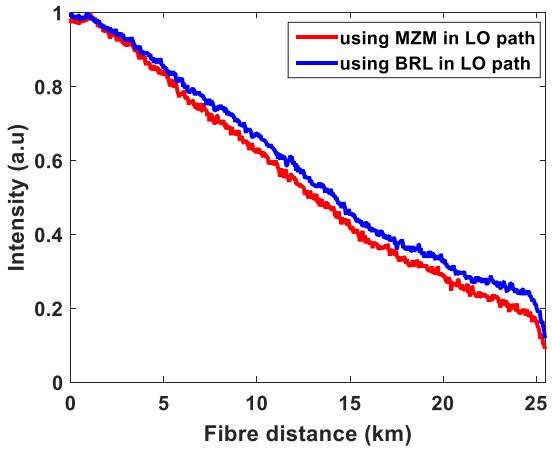

Figure 5.8. Peak Brillouin gain traces along the fibre distance using MZM and BRL in LO path

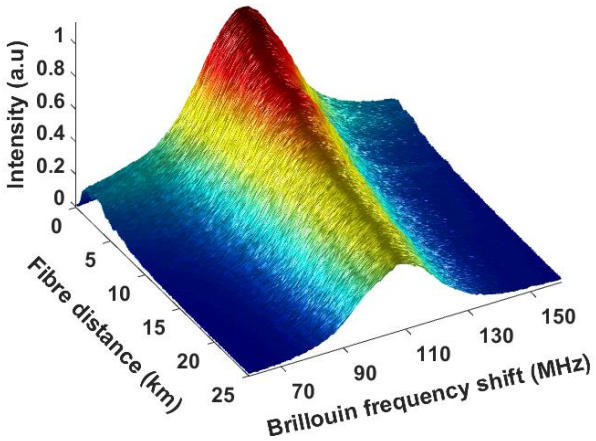

Figure 5.9. Three-dimensional Brillouin gain spectrum using BRL

5.4 Sensing Range Improvement using Inline-EDFA

One of the technique to improve the sensing range is by increasing the input pump power to compensate the unavoidable fibre loss. Moreover, maximizing the input pump power improves the SNR, thus improved measurement accuracy and sensing range. However, non-negligible nonlinear effects limits the maximum pump power. The nonlinear effects result in a rapid depletion of the pump power, thus limiting the sensing range [182]. There is a strong trade-off between the spatial resolution and sensing range. The spatial resolution is determined by the transmitted pulse width duration, whereas the dynamic range can be described as the strength of the backscattered Brillouin signal, which can be measured at a required SNR. To achieve a better spatial resolution, the shortest possible pulse has to be launched into the sensing fibre. The short pulse contains less energy and can only cover a short fibre distance, which also makes the backscattered power is relatively low. This ultimately limits the dynamic range of the system. Similarly, longer pulse width contributes to higher SNR and dynamic range, but compromise the spatial resolutions. Furthermore, due to the fibre nonlinear effects, the fibre loss and spatial resolution cannot be compensated by increasing the pulse power above the nonlinear threshold [127]. Considering this limitation, we propose to employ an inline EDFA in the BOTDR system at a certain distance to amplify the attenuated pulse. This amplification will increase the dynamic range without sacrificing the spatial resolution.

The experimental setup for the BOTDR using an inline EDFA is shown in Figure 5.10 [170]. A passive depolarizer is employed to suppress polarization noise. The BRL is used for simple, cost-effective receiver bandwidth reduction. The input pump power is 18 dBm and pulse width of 50 ns, which corresponds to 5 m spatial resolution. The sensing fibre composed of two 25 km fibre spools, where, an inline EDFA (EDFA 3) is employed at a 25 km distance. After the port 3 of circulator 2, the attenuated pulse amplified using an

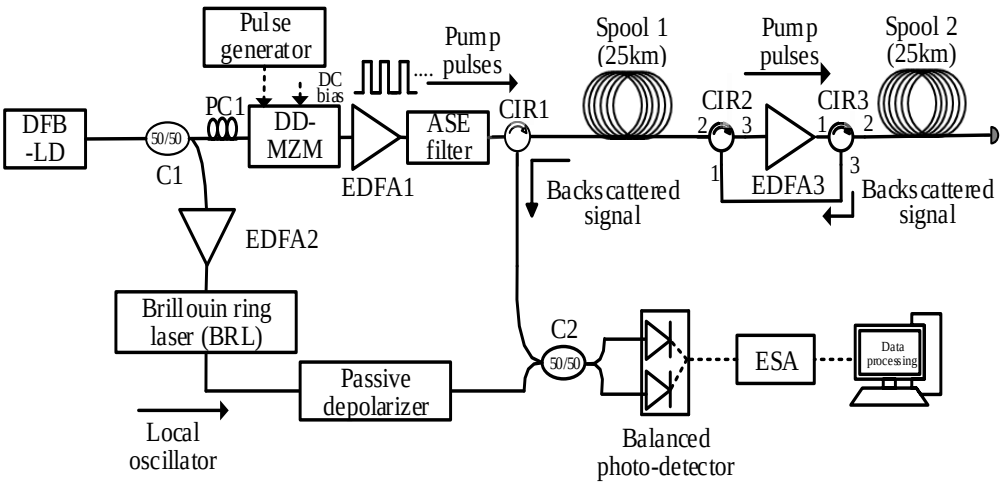

Figure 5.10. Experimental setup of BOTDR using inline EDFA

(DFB-LD= distributed-feedback laser diode, PC= polarization controller, MZM=Mach-Zehnder modulator, DD-MZM=dual drive-MZM, EDFA=erbium-doped fibre amplifier, ASE=amplified spontaneous emission, PBS=polarization beam splitter, PMF=polarization maintaining fibre, CIR=circulator, ESA=electrical spectrum analyzer, ISO=isolator)

EDFA 3 and the backscattered signal is diverted through port 3 of circulator 3 to port 1 of circulator 2. We can employ an inline EDFAs more than one in the system. However, the noise figure (typically 5 to 7 dB) increases significantly by the number of EDFAs, which reduces the SNR, thus decreases the strain and temperature measurement accuracy.

Figure 5.11 shows measurement results of the peak Brillouin frequency power traces obtained with an inline EDFA (blue curve) and without an inline EDFA (black curve). For both cases, 2000 trace averages were used. From Figure 5.11, using the conventional

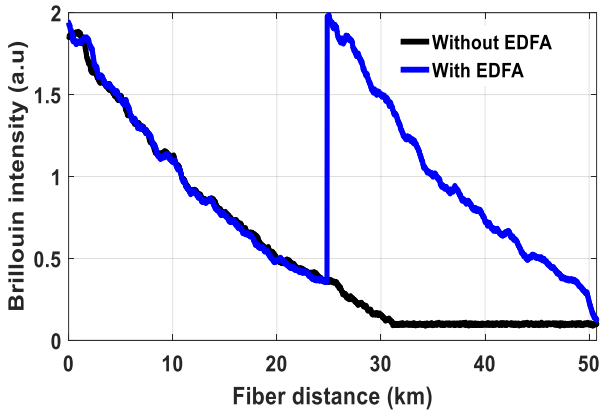

Figure 5.11. Peak Brillouin power traces over the fibre distance with EDFA and without EDFA

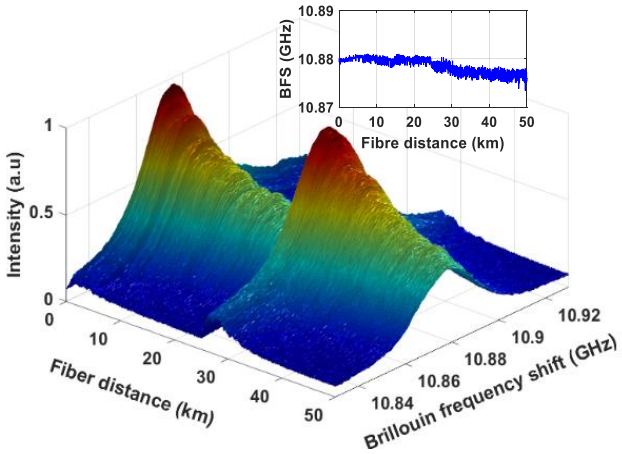

Figure 5.12. Three-dimensional distribution of Brillouin spectrum over fibre distance using inline EDFA. (inset: BFS distribution over fibre distance)

BOTDR (without inline EDFA), the intensity distribution over the fibre distance was observed until approximately 32 km. However, employing an inline EDFA at end of the 25 km, the pump power was amplified to its initial power level. In order to obtain a three-dimensional spectral mapping, the frequencies were swept with a step of 1 MHz and 2000 trace averages and illustrated in Figure 5.12. The inset in Figure 5.12 is the measured BFS distribution profile over the sensing fibre distance.

By calculating the standard deviation of the measured BFS at each fibre location, the BFS error along the fibre distance can be obtained as shown in Figure 5.13. In order to find the local average BFS error value, polynomial fit has been used for measured data.

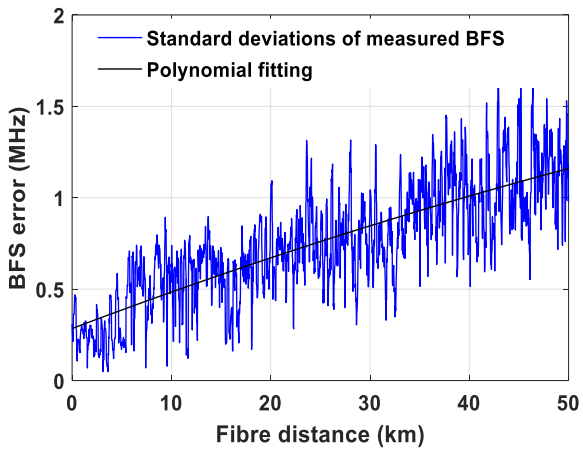

Figure 5.13. BFS error over the 50 km fibre distance with inline EDFA

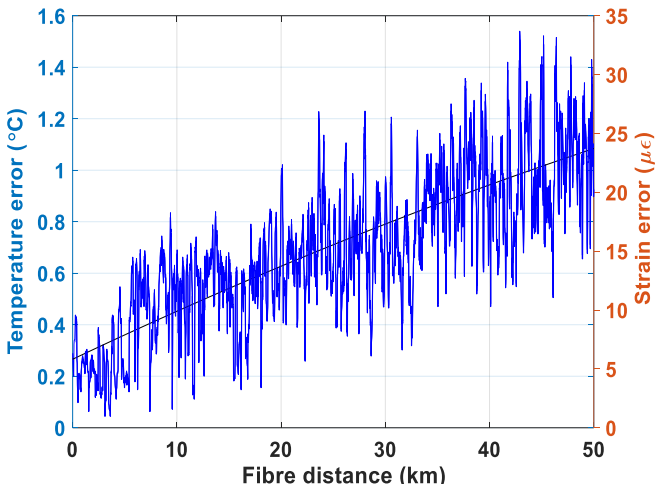

Figure 5.14. The calibrated strain and temperature errors over the 50 km fibre length with inline EDFA

From the Figure 5.13, at the far end of the sensing fibre, the BFS error is 1.16 MHz. For strain and temperature estimation errors, the calibrated strain and temperature errors are illustrated in Figure 5.14. Therefore, at the far end of the sensing fibre, the accuracy of strain measurement is 23 με (the calibrated strain coefficient of the fibre is 0.05 MHz/με). The accuracy of temperature measurement is 1.08 ºC (the calibrated temperature coefficient is 1.07 MHz/ºC) [183].

5.5 Summary

Different optimisation techniques for performance improvement of BOTDR including (i) employing balanced photodetector (ii) cost-effective Brillouin ring laser and (iii) inline EDFA are demonstrated. This chapter is divided into three main sections; the first section demonstrated the use of a balanced photodetector, which significantly amplifies the detected Brillouin power. The noise floor is found to be same as -53 dBm in both the cases of single PD and balanced PD. The detected Brillouin signal amplifies approximately doubled using balanced PD. On the other hand, a cost-effective, low complexity Brillouin ring laser (BRL) was demonstrated using a 25 km fibre. The use of

BRL in LO path significantly reduces the receiver bandwidth with less complexity, instead of using an expensive MZM and high bandwidth microwave generator. The last section of this chapter validated by means of employing an in-line EDFA to compensate for the fibre loss. An inline EDFA is employed using two circulators at a certain distance of 25 km to amplify the attenuated pulse. This amplification will increase the dynamic range without sacrificing the spatial resolution. The concept was experimentally demonstrated using a 50 km sensing fibre and 5 m spatial resolution. Chapters 4 and 5 demonstrated the limitations and performance improvement techniques in BOTDR system. The next chapter will demonstrate the proposed wavelength diversity technique to overcome the nonlinear effects within the sensing fibre, which limits the standard BOTDR sensing performance.

Chapter 6
Experimental Investigation of Wavelength Diversity Technique

6.1 Introduction

This chapter discusses the proposed wavelength diversity technique employed in the BOTDR system. The performance analysis of the proposed wavelength diversity technique is investigated experimentally and compared with the conventional single wavelength BOTDR system. In a BOTDR system, the signal-to-noise ratio (SNR) of the detected Brillouin signal determines the strain and temperature measurement accuracy at any given location. Moreover, the higher SNR requires a lower number of trace averages, thus a shorter measurement time. The SNR depends on the injected pump power, LO power, sensing fibre distance and polarization noise. Increasing the injected pump power in the BOTDR system will improve the SNR but the level of the pump power is limited by the non-negligible nonlinear effects in the sensing fibre, which comprises of stimulated Brillouin signal (SBS) [121]. If the pump power is above the nonlinear threshold, it will result in pump power depletion and invoke unwanted nonlinear effects, hence reducing the sensing range and the accuracy of strain and temperature measurements [184]. Considering the input pump power limitation, a novel wavelength diversity technique is proposed in this research study. This technique enables the maximization of the launch pump power and suppresses the nonlinear effects. As a result, the SNR increases significantly.

6.2 Operating Principle of Wavelength Diversity Technique

In the proposed wavelength diversity technique, multiple wavelengths are injected into the sensing fibre to improve the SNR, thus achieving a higher measurement accuracy. The multiple pump wavelengths significantly increase the total injected pump power into the sensing fibre without activating the unwanted nonlinear effects, while keeping each individual wavelength peak power below the SBS threshold level [176]. As described in [185], the SBS threshold for *N* pump wavelengths is given by,

$$P_N^{\text{th}} = NP_1^{\text{th}} \tag{6.1}$$

where P_1^{th} is the single pump wavelength SBS threshold. Therefore, the SBS threshold with *N* wavelengths with equal power will be *N* times greater than the single wavelength. The total pump power with *N* wavelengths cannot be raised significantly more than the stimulated Raman scattering (SRS) threshold, which imposes a power limit of ~400 to 600 mW [20, 21]. However, in the proposed technique using three wavelengths (*N*=3), the total peak power (3×18 dBm (190 mW)) is still below the SRS threshold. It is important to mention that, there are some prior works, which is employing a multi-mode Fabry–Pérot laser [186] using a polarization scrambler. Due to the large wavelength spacing (0.25 nm) between the Fabry–Pérot laser modes, the resultant beat spectrum significantly broadens, which leads to the BFS uncertainty. In 2014, M. A. Soto *et al*. [176] proposed a time and frequency pump-probe multiplexing method based on two arrays of fibre Bragg gratings (FBGs) in the BOTDA system in order to avoid the nonlinear effect, which is modulation instability (MI). The use of a larger pump frequency spacing of 17 GHz leads to a substantial spectral broadening at the receiver. Moreover, the use of a polarization scrambler induces an additional noise to the system. The method proposed here is based on the heterodyne BOTDR system to overcome the SBS

nonlinearity. In addition, we employ a simple, low-cost passive depolarizer and experimentally investigated in the proposed system. The concept of the conventional BOTDR (single wavelength) and our proposed wavelength diversity BOTDR are illustrated in Figure **6.1** and Figure 6.2, respectively. Figure **6.1**, illustrates the operating principle of the conventional single wavelength BOTDR system. The pump signal at the frequency, ν_1 is injected into the sensing fibre, which generates SpBS and detected at the same end. The backscattered Brillouin signal is downshifted with respect to pump signal by the Brillouin frequency shift of frequency shift (BFS) of (~11 GHz for

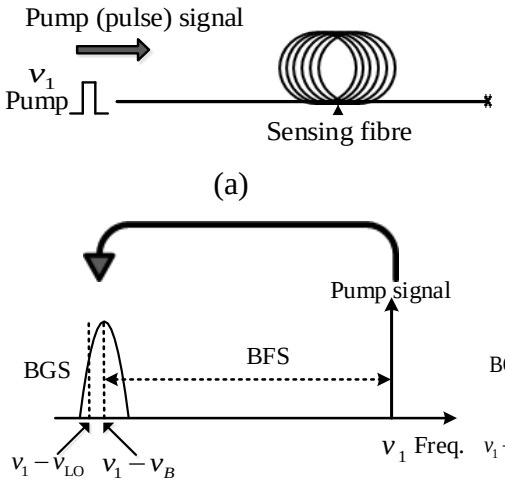

Figure 6.1. Conventional BOTDR (N=1) (a) operating principle (b) Brillouin gain spectrum

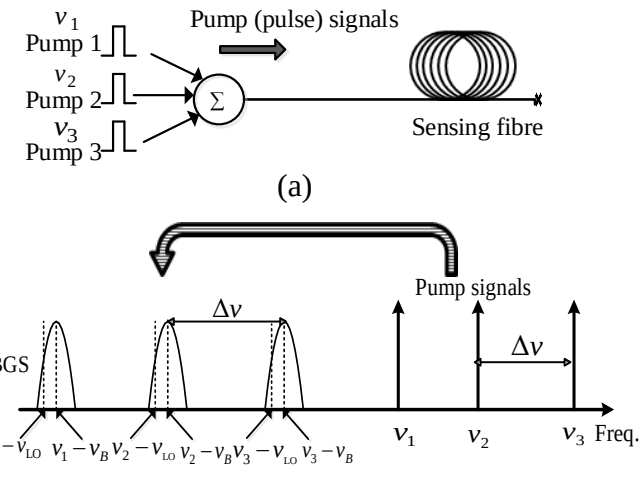

Figure 6.2. Proposed wavelength diversity BOTDR (N=3) (a) operating principle (b) Brillouin gain spectrums

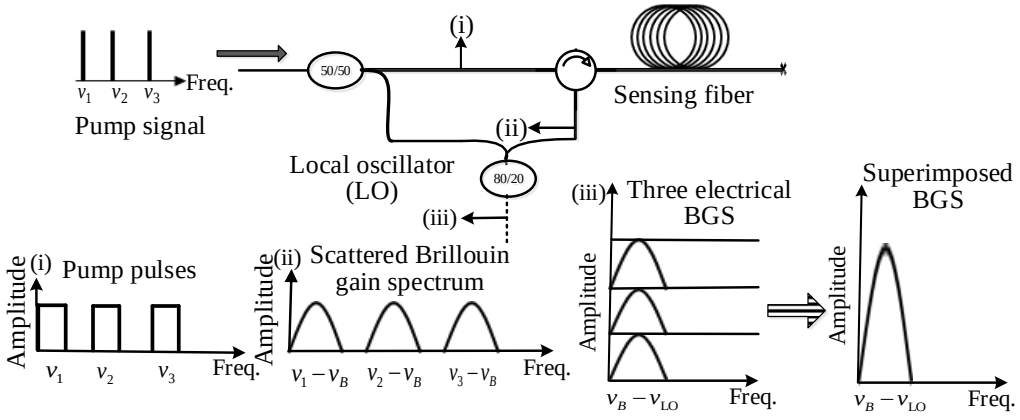

Figure 6.3. Schematic representation of proposed wavelength diversity BOTDR (N=3)

silica fibre). The Brillouin signal beat with LO signal with the frequency of $v_1 - v_{LO}$. The received electrical beat signal has the centre frequency of $v_B - v_{LO}$. In Figure 6.2 illustrates the proposed wavelength diversity technique, where, three pump wavelengths (N=3, where N is the number of wavelengths) with the corresponding frequencies of v_1, v_2 and v_3 have been considered for generating multiple pump wavelengths instead of a single wavelength in the conventional BOTDR. As shown in Figure 6.2, the three pump wavelengths generate three BGS, which beat with the corresponding LO signals and each pump wavelength has the same frequency separation (Δv) as shown in Figure 6.2(b). The Stokes and Anti-stokes of each pump wavelength, which are $v_N - v_B$ and $v_N + v_B$, respectively (where, N=1, 2, 3) beat with corresponding LO frequencies of $v_N - v_{LO}$ and $v_N + v_{LO}$, respectively. Therefore, at the receiver, the superimposed Brillouin gain amplitude (which is proportional to the sensor amplitude response improvement [176]) will be N (three) times larger than that of the conventional BOTDR as shown in Figure 6.3. As a result, the SNR will increase. Considering the LO frequencies of $v_N - v_{LO}$ and $v_N + v_{LO}$, and the backscattered Brillouin Stokes signals of $v_N - v_B$ (N=1, 2, 3), the potential obtained frequency components are described in Figure 6.4. It is noted that, the frequency spacing between the pump wavelengths should be larger than the PD bandwidth, in order to avoid the undesired beating between the other LO frequencies and backscattered Brillouin signals.

In our proposed technique, the following factors should be taken into account: (i) the frequency spacing between the pump wavelengths should be greater than the PD bandwidth, in order to avoid the undesired beating between the other LO frequencies and

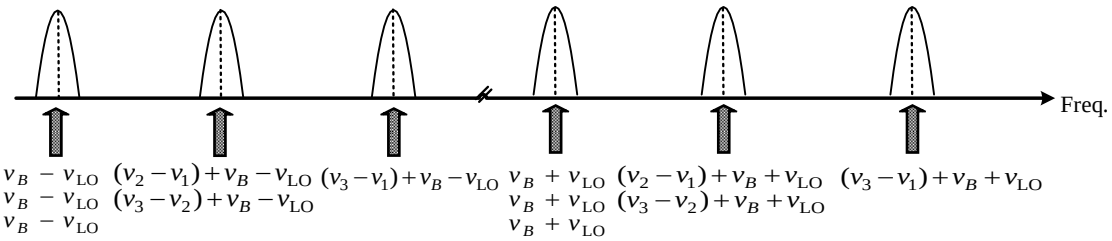

Figure 6.4. Schematic diagram of beat signal frequency components of LO frequencies $(\nu_1 \pm \nu_{LO}, \nu_2 \pm \nu_{LO}, \nu_3 \pm \nu_{LO})$ and Brillouin Stokes signals $(\nu_1 - \nu_B, \nu_2 - \nu_B, \nu_3 - \nu_B)$

backscattered Raleigh and Brillouin signals; (ii) the frequency spacing between the different pump wavelengths must be two times larger than the BGS linewidth of ~30 MHz to avoid the interference; (iii) on the other hand, if the frequency spacing is too large then it will result in a beat spectral broadening at the receiver, which causes a BFS uncertainty [187]. As shown in Figure 6.5, we experimentally verified that the BFS dependence on pump wavelength. Figure 6.5(a) shows the measured BGS for different pump wavelengths ranging from 1546 to 1562 nm and the resultant BFS dependence is 7.02 MHz/nm, as shown in Figure 6.5(b). This corresponds to 0.056 MHz/GHz. In the proposed system, the frequency spacing is 5 GHz, therefore, the total broadening is approximately 0.28 MHz, which is negligible as the natural BGS linewidth (FWHM) is about ~30 MHz. The other nonlinear effects such as four-wave mixing (FWM) and cross-

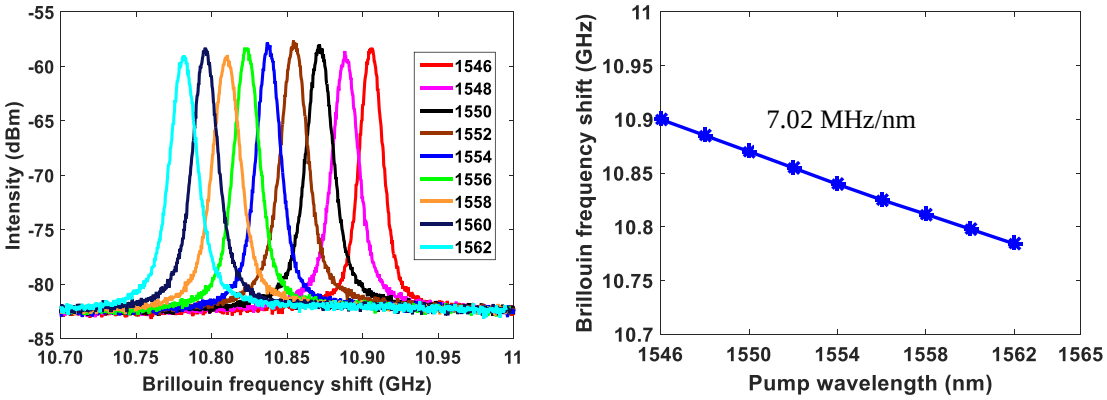

(a) (b)

Figure 6.5. (a). BGS measured for different pump wavelengths (b) calculated BFSs for wavelengths ranging from 1546 to 1562 nm

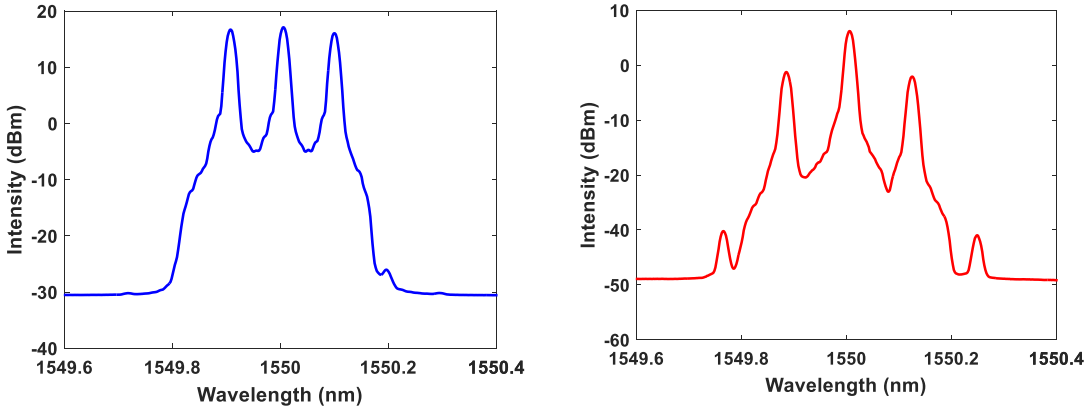

(a) (b)

Figure 6.6. Measured optical spectrums at (a) input and (b) output of the sensing fibre (25 km)

phase modulation are considered negligible in proposed technique, as each wavelength pump power is less than the SBS threshold and pump pulse repetition frequency normally less than 1 MHz [110], (in our experiment, the pulse repetition frequency is 4 KHz). We experimentally verified that, the power efficiency of FWM in our proposed system. The input pump optical spectrums at the beginning and end of the sensing fibre (25 km) are illustrated in Figure 6.6. At end of the sensing fibre, the power of the FWM spectral component is approximately -40 dBm, which is less than the 0.1% of the input pump power (18 dBm).

Furthermore, the pump wavelength frequency spacing can be set with following different cases:

Case 1 $\left(\Delta v > 2 \times \mathrm{BFS}\right)$: The frequency spacing between *N* pump wavelengths is at least twice as large as the BFS (~11 GHz) of the sensing fibre to ensure no frequency overlapping. In this case, the main disadvantage is that the large spectral coverage is required in the presence of higher pump wavelengths. In addition, the higher frequency RF signal generator and electro-optic modulator are needed to generate different pump wavelengths, which make the system expensive.

Case 2 $\left(\mathrm{BFS} < \Delta\nu < 2\times\mathrm{BFS}\right)$: The frequency spacing can be higher than the BFS but less than the twice of the BFS. This configuration is spectrally more efficient than the case 1. However, in both case 1 and 2, the use of large frequency spacing leads to the beat spectral broadening, thus BFS uncertainty.

Case 3 $\left(2\Delta\nu_B < \Delta\nu < \mathrm{BFS}\right)$: The frequency spacing is lower than the BFS but higher than the twice the BGS linewidth $2\Delta\nu_B$ (~60 MHz), hence avoiding the crosstalk between BGS. In this case, generation of multi-pump wavelengths could be easier since it only requires lower RF frequency components. Moreover, the BFS uncertainty induced by the beat spectral broadening can be considered negligible [43]. Therefore, the most effective configuration for separation of pump wavelength is case 3.

Furthermore, the detected photocurrent with *N* wavelengths can be expressed as [110],

$$I_{\mathrm{ph}}(t) = 2R_D\sum_{i=1}^{N}\sqrt{P_{Bi}(t)P_{\mathrm{LO}i}}\ \cos(\nu_{Bi}-\nu_{\mathrm{LO}i})t\cos\theta(t) \tag{6.2}$$

where R_D is the photodetector responsivity, $P_{Bi}(t)$ is the peak Brillouin signal power of i^{th} pump wavelength at time *t*, $P_{\mathrm{LO}i}$ is the peak power of i^{th} LO signal, $(\nu_{Bi}-\nu_{\mathrm{LO}i})$ is the frequency difference between the Brillouin signal and LO signal, θ denotes the polarization angle difference of Brillouin signal and LO signal. Furthermore, the SNR of the wavelength diversity BOTDR with *N* wavelengths can be expressed as follows [169],

$$\mathrm{SNR}_N = \frac{2R_D^2\cos^2\theta(t)P_{T_B}(t)P_{T_{\mathrm{LO}}}\sqrt{N_{\mathrm{avg}}}}{(4kTB/R_L)+(2qR_DP_{T_{\mathrm{LO}}}B)+\cos^2\theta(t)+<i^2_{\mathrm{E-noise}}>} \tag{6.3}$$

where $P_{T_B}(t)$ is the total peak power of the Brillouin signal, $P_{T_{\mathrm{LO}}}$ is the total LO power and N_{avg} is a number of trace averages. In the above denominator, the first term $(4kTB/R_L)$ and the second term $(2qR_DP_{T_{\mathrm{LO}}}B)$ denote the thermal noise and shot noise of the photodetector, respectively. k is the Boltzmann constant, *T* is the photodetector

operating temperature in Kelvin, R_L is the load resistance, q is the elementary charge, B is the bandwidth of the photodetector and the term $< i^2_{\text{E-noise}} >$ is the power of the electrical noise.

Assuming, the polarization state of both Brillouin signal and LO signal are identical to each other (θ=0, a passive depolarizer is used in the proposed system) and sufficient trace averages are used (N_{avg}>2000) [188], then the SNR can be modified as,

$$\text{SNR}_N = \frac{2R_D^2 P_{T_B}(t) P_{T_{\text{LO}}}}{(4kTB/R_L) + (2qR_D P_{T_{\text{LO}}} B) + < i^2_{\text{E-noise}} >} \tag{6.4}$$

$P_{T_B}(t)$ and $P_{T_{\text{LO}}}$ can be expressed as:

$$P_{T_B}(t) = \sum_{i=1}^{N} P_{Bi}(t) \tag{6.5}$$

$$P_{T_{\text{LO}}} = \sum_{i=1}^{N} P_{\text{LO}i} \tag{6.6}$$

where $P_{Bi}(t)$ is the peak power of the Brillouin signal of i^{th} pump wavelength and $P_{\text{LO}i}$ is the peak power of the i^{th} LO signal, respectively. In the proposed technique, each pump wavelength has the same level of peak power, which is below the SBS threshold. Therefore, the total injected pump power is spectrally distributed over three wavelengths to overcome the nonlinear effects.

6.3 Experimental Analysis of Wavelength Diversity BOTDR

The experimental system for the proposed wavelength diversity BOTDR using the passive depolarizer is shown in Figure **6.7**. A tunable distributed feedback (DFB) laser at a wavelength of 1550.116 nm with an output power of 10 dBm is used as a laser source. The single wavelength laser output is modulated by an MZM, which is driven by an external microwave signal generator at 5 GHz. In order to stabilize the frequency spacing

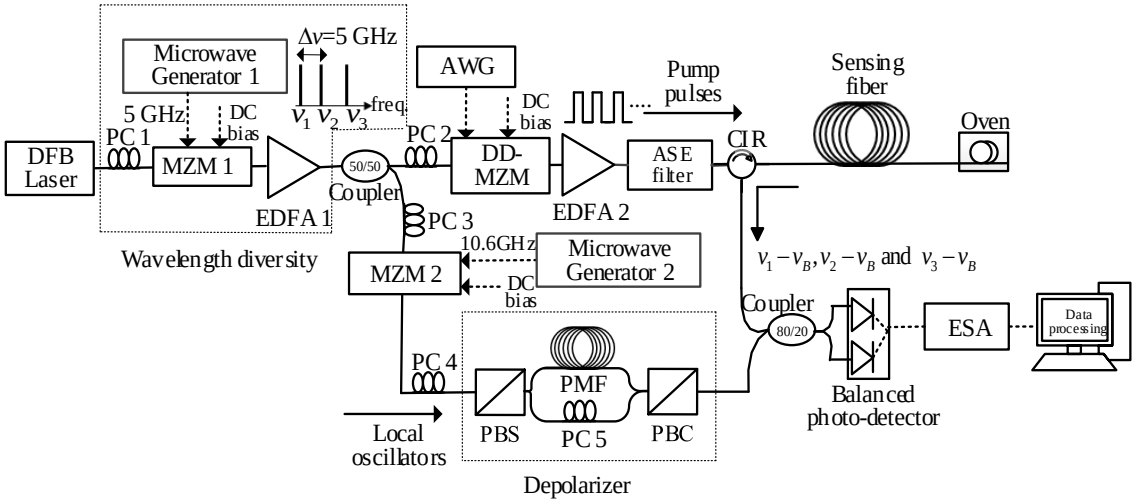

Figure 6.7. Experimental system of wavelength diversity BOTDR (N=3) using passive depolarizer

(DFB laser= distributed feedback laser, PC= polarization controller, MZM=Mach-Zehnder modulator, EDFA=erbium doped fibre amplifier, DD-MZM=dual drive-MZM, ASE=amplified spontaneous emission, CIR=circulator, PBS=polarization beam splitter, PBC=polarization beam combiner, PMF=polarization maintaining fibre, ESA=electrical spectrum analyzer)

Table 6.1. System Parameters

Component	**Parameter**	**Value**
Distributed feedback (DFB) laser	Linewidth	2 MHz
	Wavelength	1550.116 nm
	Output power	10 dBm
MZM 1	Bandwidth	15 GHz
	Modulation frequency	5 GHz
Microwave generator 1	Bandwidth	7 GHz
DD-MZM	Bandwidth	12 GHz
ASE filter	Passband	1545-1565 nm
MZM 2	Bandwidth	20 GHz
	Modulation frequency	10.6 GHz
Microwave generator 2	Bandwidth	20 GHz
Polarization maintaining fibre (PMF)	Length	5 km
Balanced-photodetector	Bandwidth	400 MHz

between the pump wavelengths, a specially designed bias control circuit is used, which ensures a stable operation over time. By tuning the DC bias of the modulator, the three pump wavelengths (i.e., the carrier and two sidebands) can be set to an equal peak power.

The three pump wavelengths are split into two propagation paths using 50/50 coupler, the upper branch signal is used for the pump and the lower branch signal is used for the local oscillator (LO) signal. The polarization controller (PC) is employed at the input of each MZM to achieve the maximum optical power at the output of the MZMs. The upper branch signal is modulated with a dual drive MZM (DD-MZM), which modulates the electrical pulses into an optical pulse with a high extinction ratio (~42 dB). Subsequently, the output signal is amplified by an EDFA 1. An amplified spontaneous emission (ASE) filter is used to eliminate the ASE noise from the EDFA 1. The peak pump power and pulse width of each pump wavelength are the same as those of the single wavelength, i.e., 18 dBm and 50 ns, respectively.

The LO signal is then modulated by the MZM 2, whose frequency is downshifted and upshifted by 10.6 GHz from the original frequency with six sidebands. Thereafter, the six LO signals are fed into the passive depolarizer to suppress the polarization. The LO signal beat with the three BGS. The beat signal is detected by the balanced photodetector and analysed by an electrical spectrum analyzer (ESA) in a zero-span mode. Acquisition procedure and data processing remain identical to those of the conventional single wavelength BOTDR. The electrical signal from the B-PD consist summed contribution of BGS generated by three pump wavelengths.

6.3.1 Results Discussion

The peak Brillouin frequency power traces obtained for wavelength diversity BOTDR with depolarizer and without depolarizer are illustrated in Figure 6.8. For both the cases, 2000 trace averages are used. As shown in Figure 6.8, the signal fluctuations induced by the polarization noise has been reduced significantly using a depolarizer, which proves that the introduction of a passive depolarizer can effectively reduce the beat signal fluctuations [189].

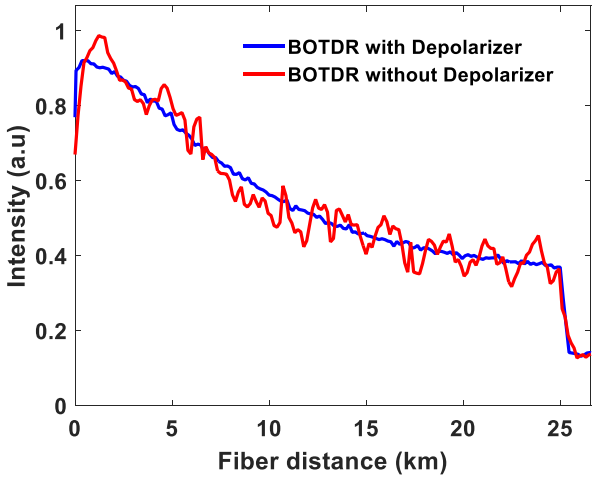

Figure 6.8. Peak Brillouin power traces of wavelength diversity BOTDR with depolarizer (blue curve) and without depolarizer (red curve)

To experimentally validate the proposed system, the peak Brillouin frequency power traces are measured for both the conventional single wavelength BOTDR and wavelength diversity BOTDR (N=3). Figure 6.9 illustrates the comparison of the SNR of measured traces for three different cases. The measured SNR of the wavelength diversity BOTDR without depolarizer (black curve) has strong oscillations induced by the polarization noise. Interestingly, the same SNR response has been obtained at the starting of the sensing fibre, due to the same input pump power and low polarization noise, as the shorter optical path. However, the polarization noise is significantly reduced using the passive depolarizer technique. At the far end of the sensing fibre, the SNR of the conventional BOTDR (red curve) is 5.1 dB. However, for the proposed wavelength diversity BOTDR (blue curve), the SNR has been significantly improved up to 9.95 dB. Therefore, the improved SNR is 4.85 dB, which corresponds to 174% improvement compared to a conventional BOTDR system.

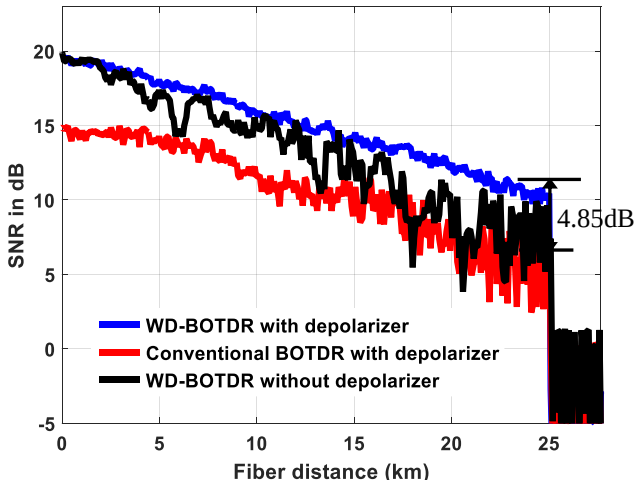

Figure 6.9. Comparison of measured signal-to-noise ratio (SNR) at peak Brillouin gain frequency of conventional BOTDR (red curve), WD-BOTDR with depolarizer (blue curve) and WD-BOTDR without depolarizer (black curve)

In order to obtain a three-dimensional spectral mapping, the frequencies are swept from 10.79 GHz to 10.94 GHz with a frequency step of 1 MHz and 2000 trace averages. The proposed wavelength diversity BOTDR spectrum with passive depolarizer is shown in Figure 6.10. The obtained BFS profile over the sensing fibre distance is shown in Figure 6.10 inset.

The BFS distribution of conventional BOTDR and wavelength diversity BOTDR (both with passive depolarizer) over the sensing fibre is shown in Figure 6.11. By calculating the standard deviation of measured BFS at each fibre location, the frequency

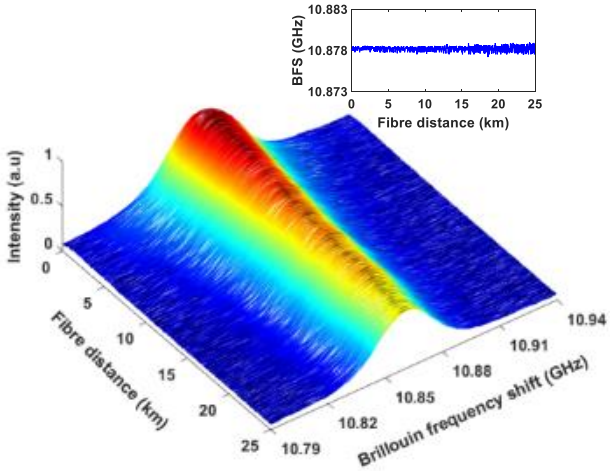

Figure 6.10. Measured three-dimensional spectrum over fibre distance of proposed wavelength diversity BOTDR with passive depolarizer

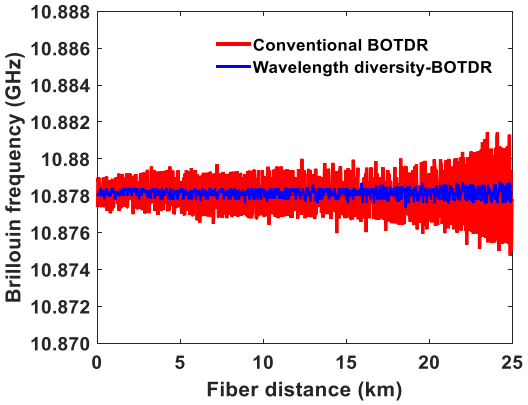

Figure 6.11. Brillouin frequency shift (BFS) distribution of conventional BOTDR and wavelength diversity BOTDR

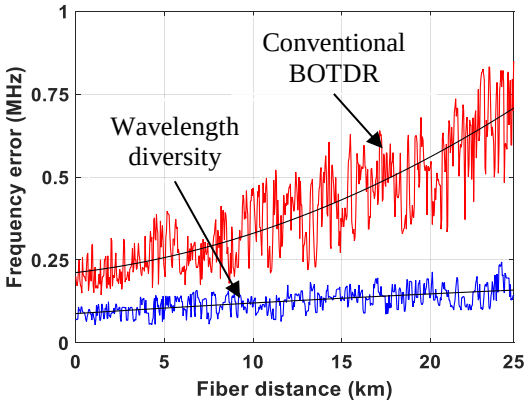

Figure 6.12. Brillouin frequency measurement error vs fibre distance of conventional BOTDR and wavelength diversity BOTDR

error along the fibre distance can be obtained. We experimentally verified the strain and temperature sensitivities of the sensing fibre. We obtained the strain sensitivity of 0.05 MHz/με and temperature sensitivity of 1.07 MHz/^{o}C. As shown in Figure 6.12, at the far end of the sensing fibre, the frequency error of the conventional BOTDR and wavelength diversity BOTDR are 0.65 MHz and 0.18 MHz, respectively. Therefore, at the far end of the sensing fibre, the accuracy of strain measurement is 13 με and 3.6 με, respectively (the calibrated strain coefficient of the fibre is 0.05 MHz/με). Whereas, the temperature measurement accuracies are 0.6^{o}C and 0.16^{o}C, respectively (the calibrated temperature coefficient is 1.07 MHz/^{o}C). This corresponds to measurement accuracy improved 3.6 times for the strain and 3.75 times for the temperature using the proposed wavelength diversity BOTDR compared to the conventional single wavelength BOTDR.

In order to evaluate the temperature sensing performance and spatial resolution of the proposed system, a 30 m fibre at the far end of the sensing fibre is placed in an oven. The rest of the fibre is kept strain free and at room temperature (~25^{o}C). At 65^{o}C, the three-dimensional spectral mapping is shown in Figure 6.13. The frequencies are swept from 10.8 GHz to 11 GHz, with a frequency step of 1 MHz and 2000 trace averages. The BFS

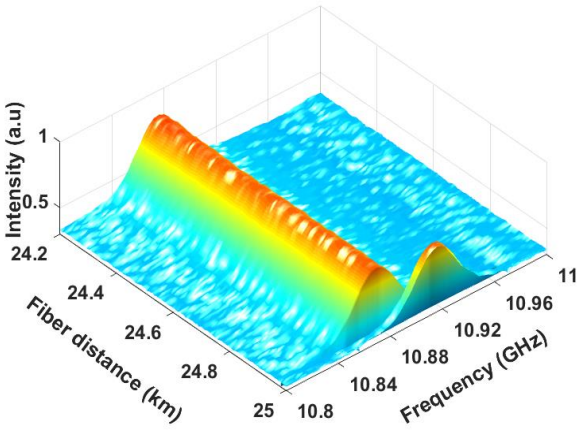

Figure 6.13. Temperature (65^{o}C) induced three-dimensional spectrum of wavelength diversity BOTDR at far end of the sensing fibre

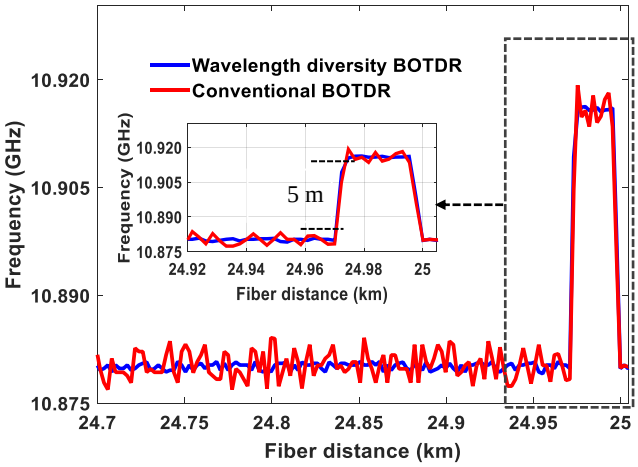

Figure 6.14. Comparison of measured BFS distribution of conventional BOTDR and proposed wavelength diversity BOTDR

distribution along the sensing fibre for both the conventional BOTDR and wavelength diversity BOTDR is illustrated in Figure 6.14. The pulse width determines the spatial resolution of the system, which can be also calculated in the time domain based on the rise time. The spatial resolution of 5 m is obtained as shown in Figure 6.14 inset, which confirms the 50 ns pulse width used in both systems. The results demonstrate an accurate temperature measurement and no penalty on the spatial resolution in our proposed technique.

6.4 Employing Wavelength Diversity Technique in Brillouin Ring Laser based BOTDR System

As described in Chapter 5, the Brillouin ring laser (BRL) is a simple and cost-effective for receiver bandwidth reduction rather than the complex and expensive Mach-Zehnder modulator (MZM) employed in local oscillator (LO) path. After the MZM in LO path, each frequency further up and down shifted, and the higher order sideband components make the signal interference between those backscattered Brillouin signals. Therefore, an excess noise easily generates from the additional LO frequencies. The BRL has a high spectral quality with minimized sideband components. Therefore, the proposed wavelength diversity technique is employed in a BRL based BOTDR system. The proposed system can improve the SNR significantly with a simple and cost-effective implementation. The experimental setup for the wavelength diversity BOTDR using the BRL and passive depolarizer is shown in Figure 6.15. The BRL output consists of three Brillouin signals, which beat with the backscattered Brillouin signals of the sensing fibre. The received signal is detected by the balanced PD and amplified by a low noise RF

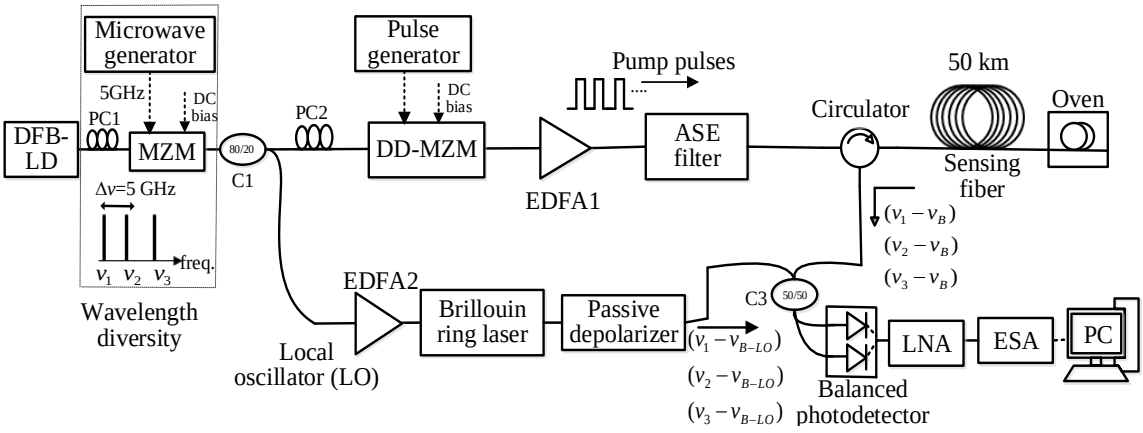

Figure 6.15. Experimental setup of wavelength diversity BOTDR using Brillouin ring laser

(DFB-LD= distributed feedback laser diode, PC= polarization controller, MZM=Mach-Zehnder modulator, C=coupler, DD-MZM=dual drive-MZM, EDFA=erbium doped fibre amplifier, ASE=amplified spontaneous emission, LNA= low-noise amplifier, ESA=electrical spectrum analyzer)

amplifier (LNA), then analysed by an electrical spectrum analyser (ESA). Acquisition procedure and data processing remain identical to those of the conventional single wavelength BOTDR. In order to evaluate the sensing performance, the temperature effects have been measured using a 50 km sensing fibre with a 5 m spatial resolution.

6.4.1 Results Discussion

Firstly, the BRL with three input wavelengths has been experimentally investigated. The three input wavelengths at a frequency of ν_1, ν_2, ν_3 ($\Delta\nu$ =5 GHz) and the three BRL output spectrums, $\nu_1 - \nu_{B-LO}$, $\nu_2 - \nu_{B-LO}$, $\nu_3 - \nu_{B-LO}$ are shown in Figure 6.16. The BRL output consists of three SBS spectrums corresponds to three input pump wavelengths. It is important to mention that, these optical spectrums are measured by an optical spectrum analyzer (OSA, AQ6370C) with a minimum resolution of 0.02 nm. The SBS peak powers can be easily adjustable using an EDFA 2 in LO path [190].

In order to experimentally validate the proposed system, the peak Brillouin frequency power traces are measured with a 50 km (two 25 km spools) fibre for both the conventional single wavelength BOTDR (N=1) and wavelength diversity BOTDR (N=3) using BRL. For a reliable comparison, the peak power and pulse width of each pump wavelength are the same as those of the conventional single wavelength, i.e., 18 dBm and

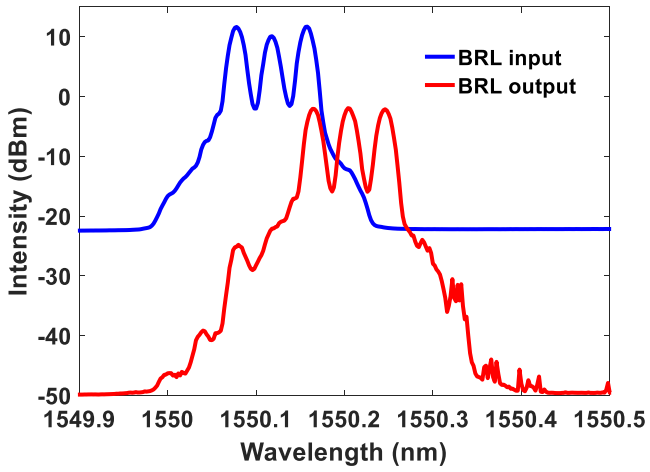

Figure 6.16. The Brillouin ring laser input and output optical spectrums

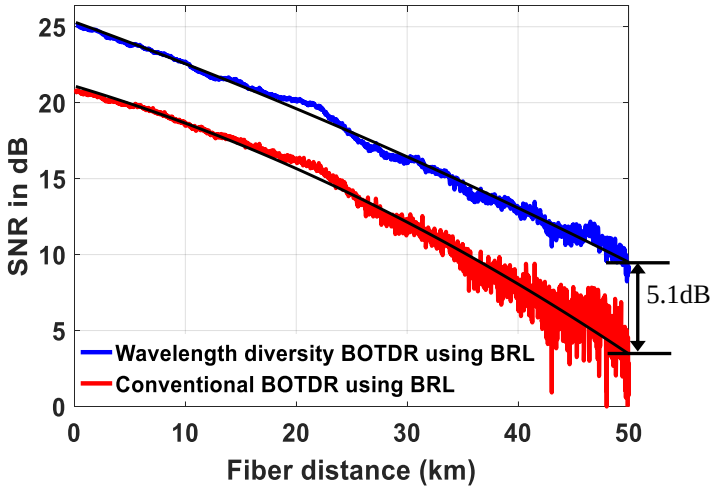

Figure 6.17. Measured signal-to-noise ratio (SNR) at peak Brillouin gain frequency of conventional BOTDR (red curve), wavelength diversity BOTDR (blue curve) using Brillouin ring laser (BRL)

50 ns, respectively. The SNR has been measured along the sensing fibre length, then fitted with a polynomial curve in both the cases as shown in Figure 6.17.

At the end of the sensing fibre, the obtained SNR for the conventional BOTDR using the BRL is 3.6 dB. The proposed wavelength diversity BOTDR using the BRL is found to be 8.7 dB. Therefore, the improved SNR is 5.1 dB. For the wavelength diversity BOTDR (N=3), even with the high injected pump power, the measured SNR (blue trace in Figure 6.17) has no distortions particularly from nonlinear effects and the pump power does not experience a power depletion, as the total power is spectrally distributed over the three wavelengths. It is worth mentioning the noise power level has been measured in both the cases, for N=1 and N=3. The measured RMS voltage of the noise level is found to be same for both cases, i.e., 71 µV with 2000 trace averages, as the system is dominated by the thermal noise [176]. Thus, the total noise floor level is same for the conventional BOTDR (N=1) and wavelength diversity BOTDR (N=3) using the BRL.

The three-dimensional spectral mapping of proposed wavelength diversity BOTDR using the BRL is obtained with a sweep frequency step of 1 MHz and 2000 trace averages

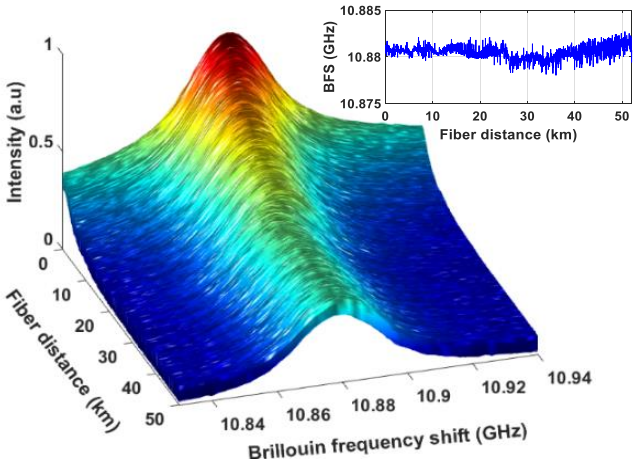

Figure 6.18. Brillouin gain spectrum over sensing fibre distance. (inset: BFS distribution over the fibre distance)

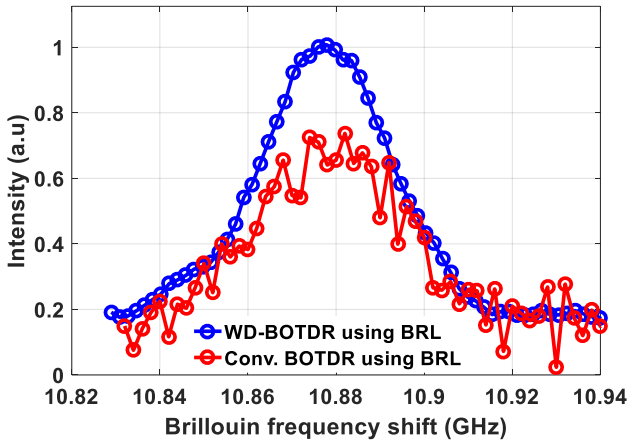

Figure 6.19. Brillouin gain spectrums at end of the sensing fibre of conventional and wavelength diversity BOTDR

and illustrated in Figure 6.18. The Lorentzian curve fitting is used for the obtained data and the measured BFS distribution over the fibre distance is shown in Figure 6.18 inset. The Brillouin gain spectrums at one fibre location (at end of the sensing fibre) are extracted in both cases and illustrated in Figure 6.19. It can be clearly seen that the signal fluctuations are greatly reduced using the proposed wavelength diversity technique.

By calculating the standard deviation of the measured BFS at each fibre location, the BFS error along the fibre distance can be obtained. The standard deviations have been measured for the BFS along the sensing fibre for conventional BOTDR (N=1) and the

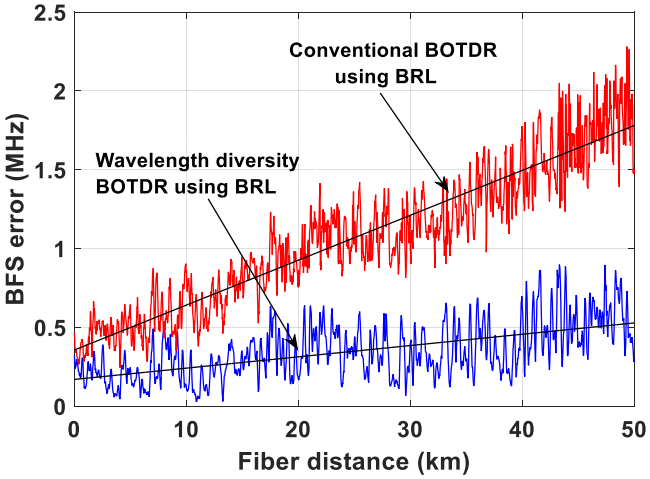

Figure 6.20. Brillouin frequency shift (BFS) error vs fibre distance of conventional BOTDR and wavelength diversity BOTDR using Brillouin ring laser

wavelength diversity BOTDR (N=3) using a BRL are illustrated in Figure 6.20. At the end of the sensing fibre, the BFS errors for the two cases are measured to be 1.75 and 0.52 MHz, respectively. Therefore, at the far end of the sensing fibre, the estimated accuracy of strain measurement is 35 με and 10 με, respectively (the calibrated strain coefficient of the sensing fibre is 0.05 MHz/με). Whereas, the temperature measurement accuracies are 1.63^{o}C and 0.48^{o}C, respectively (the calibrated temperature coefficient is 1.07 MHz/^{o}C).

Finally, the sensing performance and spatial resolution are characterized experimentally for the proposed wavelength diversity BOTDR using BRL. At the end of the sensing fibre, a 20 m fibre is kept in the temperature oven, while the rest of the fibre is kept at strain free and ambient room temperature (~25^{o}C). The temperature was set at 50^{o}C within the oven. The BFS distribution along the whole sensing fibre is shown in Figure 6.21 inset. The spatial resolution of 5 m is obtained as shown in Figure 6.21. The results demonstrate an accurate temperature measurement without sacrifice on the spatial resolution. For a 25^{o}C temperature change, the estimated BFS is 26.75 MHz (25×1.07 MHz). From the Figure 6.21, the measured BFS change is 27.18 MHz for a temperature

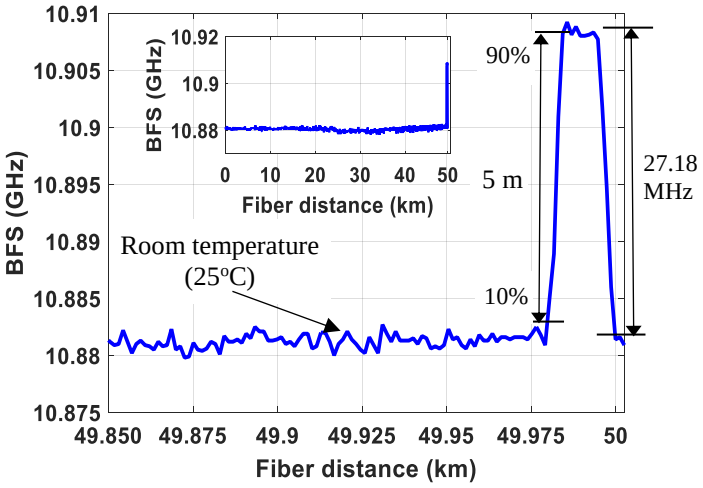

Figure 6.21. Brillouin frequency shift distribution under temperature effects on 20 m fibre at end of the sensing fibre

change of 25°C. Therefore, the BFS error is 0.43 MHz, which corresponds to temperature error of 0.4°C. So, we found a good agreement with the calculated standard deviation BFS error of 0.52 MHz from the Figure 6.20, which corresponds to temperature error of 0.48°C.

Considering the values listed in Table 6.2 and the data calculated using equation (6.4), (6.5) and (6.6), the theoretical SNR improvement in proposed technique compared to a single wavelength (N=1) BOTDR is illustrated in Figure 6.22. For the wavelength diversity BOTDR system (N=3), the obtained theoretical SNR improvement is 4.92 dB,

Table 6.2. Parameters used for theoretical calculation of SNR improvement [110]

Parameter	**Symbol**	**Value**
Photodetector responsivity	R_D	1 (A/W)
No. of wavelengths	N	1 to 10
Local oscillator (LO) power	P_{LO}	2.5 dBm (1.77mW)
Boltzmann constant	k	1.38×10^{-23} (J/K)
Thermodynamic temperature	T	300 (K)
Photodetector bandwidth	B	400 MHz
Load resistance	R_L	50 (Ω)
Elementary charge	q	1.6×10^{-19} (c)
Electrical (signal acquisition) noise	$< i^2_{\text{E-noise}} >$	4×10^{-13} (A^2)

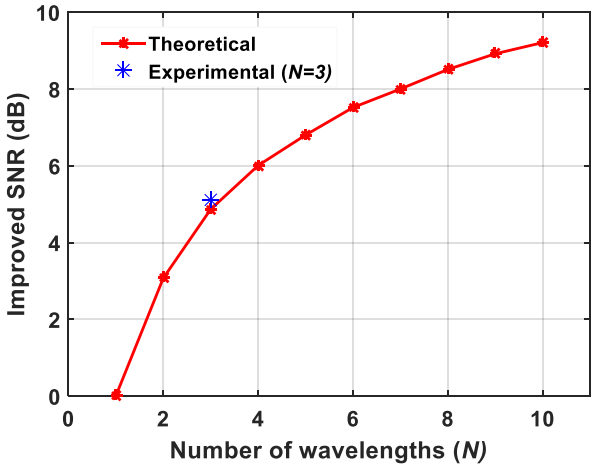

Figure 6.22. Improved SNR vs number of wavelengths

which is in a good agreement with the experimental result of 5.1 dB. As shown in Figure 6.22, the SNR improvement rate decreases as the number of wavelengths increases. This is because of the shot noise increases with increased Brillouin and LO signal power. The number of wavelengths can be increased by either multi EOMs or narrow spacing multi-wavelength laser source, however, the system will become more complex.

6.5 Summary

In this chapter, the implementation of proposed wavelength diversity BOTDR system is demonstrated. The wavelength diversity technique enables to maximize the launch pump power, hence achieving an improved SNR, while avoiding the unwanted nonlinear effects, which limits the conventional BOTDR performance. Firstly, the proof-of-concept has been implemented using a 25 km sensing fibre with 5 m spatial resolution. At end of the 25 km, the wavelength diversity BOTDR (N=3) is able to provide an enhanced SNR up to 4.85 dB, which corresponds to 174% improvement compared to the conventional single wavelength BOTDR. As a further improvement and to reduce the complexity of the system, a wavelength diversity technique employed in BRL based BOTDR system is experimentally demonstrated with an improved SNR of 5.1 dB, which is 180% improvement compared to the conventional single wavelength BOTDR using a 50 km

Table 6.3. Summary of strain and temperature measurement accuracies at 50 km distance for standard BOTDR and proposed wavelength diversity BOTDR

	Optimised conventional BOTDR (*N*=1)	**Wavelength diversity BOTDR (*N*=3)**
SNR at 50 km	3.6 dB	8.7 dB
BFS error at 50 km	1.75 MHz	0.52 MHz
Corresponding temperature accuracy	±1.63°C	±0.48°C
Corresponding strain accuracy	±35 με	±10 με
Required strain and temperature measurement accuracies for rail-track monitoring	< ±0.5°C and < ±10 με for temperature and train, respectively	

sensing fibre and 5 m spatial resolution. In the proposed system, the strain and temperature measurement accuracies were ±10 με and ±0.48°C, respectively.

The summary of strain and temperature measurement accuracies at 50 km fibre distance for optimised standard BOTDR (*N*=1) and proposed wavelength diversity BOTDR (*N*=3) are listed in Table 6.3. According to Rail Safety and Standards Board (RSSB), the required accuracy for strain and temperature measurements of the rail-track were, < ±10 με and < ±0.5°C, respectively [21, 191]. Moreover, we briefly discussed with Network Rail R&D team at Northumbria Photonics Research Laboratory and agreed for rail-track required measurement accuracies defined in Table 6.3. The proposed wavelength diversity BOTDR (*N*=3) can be able to achieve required measurement accuracies with a 50 km sensing range and 5 m spatial resolution.

This chapter focuses on the proposed wavelength diversity BOTDR system implementation, the next chapter will focus on the simultaneous integration of long-term evolution (LTE) radio over fibre (RoF) data system and BOTDR sensing system using a single optical fibre.

Chapter 7
Integration of LTE-RoF Data System and BOTDR Sensing System using a Single Optical Fibre

7.1 Introduction

Chapter 6 demonstrates the proposed wavelength diversity BOTDR system and summarised the strain and temperature measurement accuracies. This chapter solely dedicated to an efficient integration of long-term evolution (LTE) radio over fibre (RoF) data system and BOTDR sensing system using a single optical fibre. The proposed simultaneous integration of data and sensing system utilizes an existing active data transmission cable along the rail-track side. This simultaneous integration permits of rail-track monitoring and data transmission over a single optical fibre.

In recent years, mobile communication technology has developed rapidly, partly due to the huge demand for the high data rate services. Therefore, the 3rd generation partnership program (3GPP) has introduced a sophisticated technology known as the 4th generation long-term evolution (4G-LTE) to meet the demands of mobile broadband users [192]. In this regard, the 4G-LTE has introduced a network architecture that includes an enhanced NodeB (eNB) and home eNB (HeNB) for both indoor and outdoor wireless applications, respectively [11]. The LTE uses a single carrier modulation (SCM) of the quadrature-phase shift keying (QPSK), 16-quadrature amplitude modulation (16-QAM) and 64-QAM modulation based on the orthogonal frequency division multiplexing (OFDM) for downlink. QAM modulation in which data is transferred by modulating the

amplitude of two separate carrier waves (mostly sinusoidal), which are out of phase by 90 degrees. Due to their phase difference, they are called quadrature carriers. QAM modulation with *M* symbols is known as *M*-QAM, for eaxample 16-QAM and 64-QAM. The constallation sizes that are even powers of 2 (*M*=2, 4,…) are typically used to make the constallation in both axes. The 4G-LTE technology with radio-over-fibre (RoF) technique is widely adopted and the fibre infrastructure has been installed extensively, including fibre to the home (FTTH), fibre to the building/basement (FTTB), fibre to the cabinet (FTTC), fibre to the node (FTTN). [193]. Apart from that, the single-mode fibre (SMF) has been used for the broadband backbone network due to its low attenuation and large bandwidth [194]. However, there is a need to find sophisticated techniques for effective uses of the existing fibre infrastructure for other emerging applications.

On the other hand, structural health monitoring is a key element of safety and management of various infrastructures. Conventional fibre sensors, such as fibre Bragg gratings (FBG) and long-period Gratings (LPG) measure only at a specific location of interest. Over the last decade, the use of Brillouin based distributed fibre sensors for structural health monitoring applications has increased rapidly [195], due to their unique advantages, such as high sensing range over tens of kilometres, and capabilities of simultaneous strain and temperature measurements. In Brillouin based distributed fibre sensors, two techniques are commonly investigated: Brillouin optical time-domain reflectometry (BOTDR) [84], based on spontaneous Brillouin scattering (SpBS). The BOTDR system features simple implementation schemes and only requires access to the single end of the sensing fibre. The BOTDR system utilise a linear dependence of Brillouin frequency shift (BFS) on strain and/or temperature along the fibre length, while its position is determined by the pulsed time-of-flight method. However, providing a new fibre infrastructure for distributed sensing system is a huge economic burden with much complexity, which discourages the wide-spread uses of the distributed sensing system.

Therefore, sharing the existing data transmission fibre infrastructure for distributed sensing will be a cost-effective and efficient method for applications such as strain measurement in submarine active data transmission optical cable, earthquake damage, and frozen cable [197]. The Railway industry uses a fibre infrastructure installed along the track-side for the data transmission. The integration of distributed sensing system with the existing optical cable can be used for condition monitoring of land-slides, track ballast, electric-pole/tree fall, snow drifts, flooding and lineside fire detection in real-time and remotely. The integration of distributed sensing and active data transmission using a single optical fibre is an unexplored area of research.

For the first time, we proposed the simultaneous integration of LTE-RoF data transmission system and BOTDR sensing system using a single optical fibre link. The LTE-RoF data system is composed of three modulation formats of quadrature phase-shift keying (QPSK), 16-quadrature amplitude modulation (16-QAM) and 64-QAM. For the data transmission system, the error vector magnitude (EVM) is analysed for QPSK, 16-QAM and 64-QAM at different data and sensing powers and sensing powers using a 25 km single-mode silica fibre. In order to evaluate the sensing system performance, the temperature effect has been measured with a 5 m spatial resolution.

7.2 Overview of Radio-over-Fibre

Early days of telecommunication applications such as the global system for mobile communication (GSM) and general packet radio services (GPRS) can accept low data rates. However, today's users demand high data rates with secure transmission. An integration of wireless and optical systems will lead to high capacity, high data rate and mobility stations [198]. In a RoF system, light is modulated by a radio frequency (RF) signal and the modulated signal is then transmitted through an optical fibre. In other words, a system is used to transfer an RF signal over an optical fibre link is known as

RoF system. Figure 7.1 shows the RoF architecture for in-building transmission, base stations, and railway applications. At the central station (CS), the functions such as signal processing, signal routing and resource management are carried out and then the signal is transmitted to various destinations. The importance of the RoF system topology is that it could directly transmit RF signals over the fibre without any further processing at the base station (BS). All the complicated RF modem and signal processing functions remain at the CS [199]. Therefore, it directly introduces a reduction in the system wide installation and maintenance costs, reduces and simplifies BS complexity and allows a distributed system.

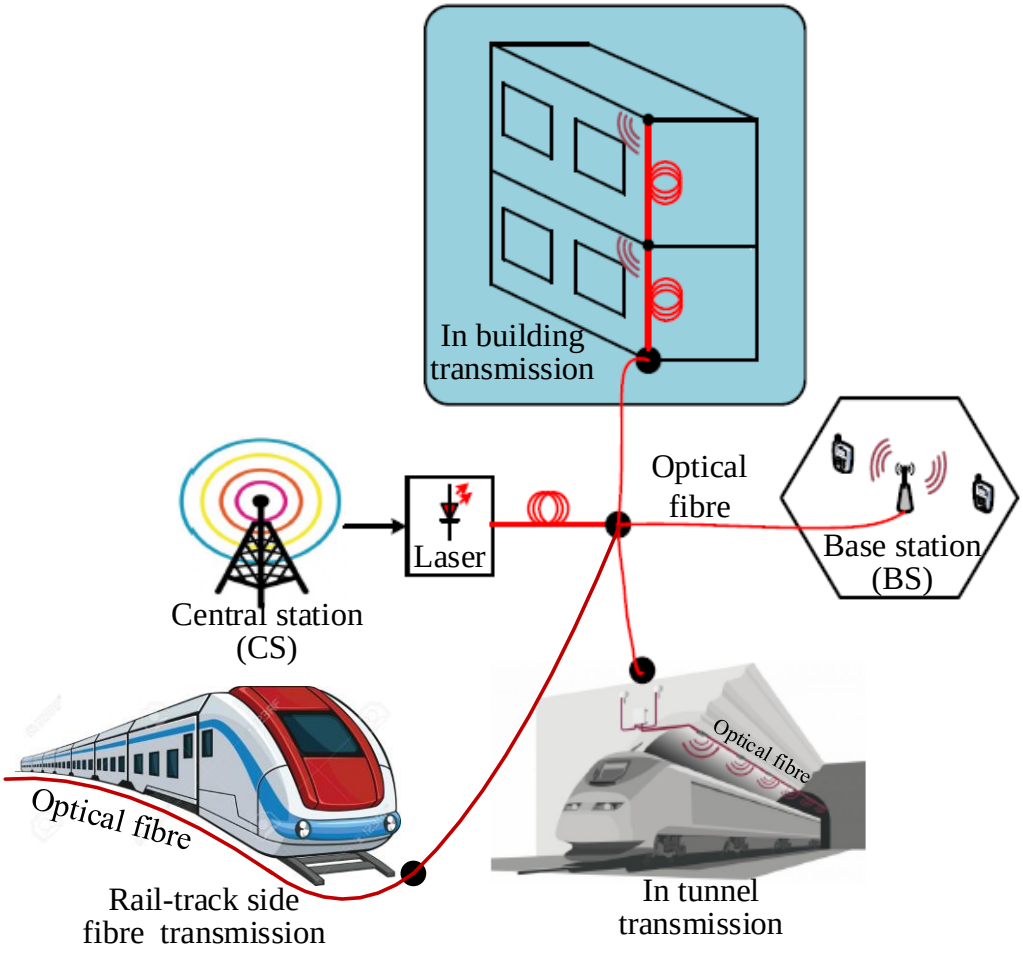

Figure 7.1. The usage of RoF for several applications

7.3 LTE-RoF Data System

The experimental setup of LTE-RoF data system is shown in Figure 7.2. A DFB laser at 1550 nm with an output power of 5 dBm is used as a laser source. The temperature controller (set at 25^{o}C) is used to maintain a constant DFB laser temperature. The continuous wave is then externally modulated using an MZM (Photline, MXAN-LN-20). The polarization controller (PC) is employed at the input of MZM to achieve the maximum optical power at the output of the MZM. The LTE signal is generated by a vector signal generator (VSG, Agilent- E4438C) with three different modulation formats of QPSK, 16-QAM and 64-QAM. The VSG generated a real-time LTE signal with a carrier frequency of 2.6 GHz and 10 MHz bandwidth via a signal studio software. After MZM, the signal is then amplified to the required launch power using an EDFA. Thereafter, the signal is transmitted through 25 km single-mode silica fibre.

At the receiver, the RF signal is detected by a PD (Thorlabs, PDA8GS) and amplified using a low noise RF amplifier (LNA, PE15A1008). The detected signal is analysed using a signal analyser (Agilent 9020A MXA), which is automated using an Agilent 89601B VSA software. The EVM of detected symbols is estimated using the VSA software in real-time. The EVM describes the system performance in the presence of noise and

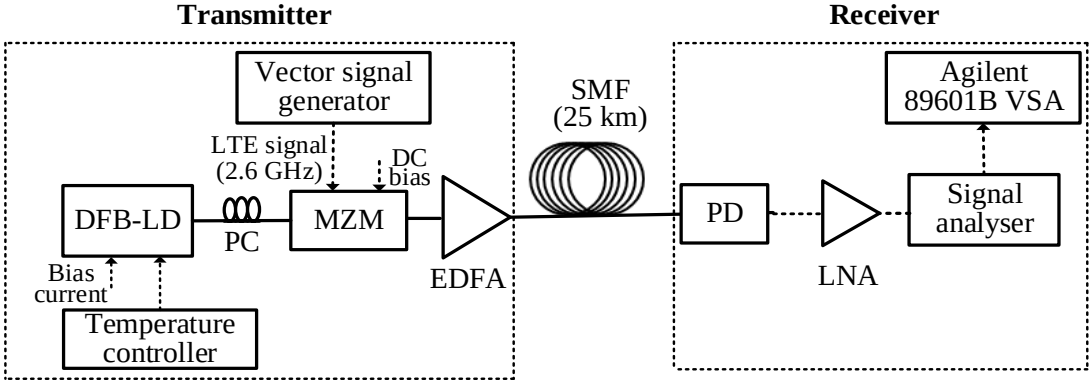

Figure 7.2. Experimental setup of LTE-RoF data system

(DFB= distributed-feedback laser, PC= polarization controller, MZM=Mach-Zehnder modulator, EDFA=erbium doped fibre amplifier, SMF=single-mode fibre, PD=photodetector, LNA=low noise amplifier)

channel impairments. The EVM is defined as the root-mean-squared (RMS) value of the difference between a collection of measured symbols and ideal symbols [200]. The value of the EVM is averaged over normally a larger number of symbols and it is often expressed as a percentage (%) or in dB. The EVM can be expressed as [201],

$$\mathrm{EVM_{RMS}} = \sqrt{\frac{\frac{1}{N}\sum_{n=1}^{N}\left|S_r(n) - S_t(n)\right|^2}{P_o}} \tag{7}$$

where N is the number of symbols for the in phase-quadrature (I-Q) constellation, $S_r(n)$ and $S_t(n)$ are the received and transmitted values of the n^{th} baseband symbol and P_o is the average power of the ideal transmitted symbol, which is utilized for normalization [202]. In an additive white Gaussian noise (AWGN) is ≈1 and a large value of N, the ideal EVM can be further expressed as [201],

$$\mathrm{EVM_{RMS}} \approx \sqrt{\frac{N_o}{P_o}} = \sqrt{\frac{1}{SNR}} \tag{8}$$

However, as regards SNRs and considering the channel impairments, the measured EVM values in this case is expected to be less than the ideal values [200].

7.4 BOTDR Sensing System

The experimental setup for the BOTDR sensing system is illustrated in Figure 7.3. A tunable DFB laser at a wavelength of 1546.12 nm and an output power of 12 dBm is used as a laser source. The LO signal is modulated by the MZM 2, whose frequency is downshifted and upshifted by 10.6 GHz from the original frequency. Thereafter, the LO signal is was fed into the passive depolarizer to suppress the polarization noise. the received signal is was detected using the balanced photodetector (bandwidth: 400 MHz) and analyzed using an electrical spectrum analyzer (ESA) in a zero-span mode.

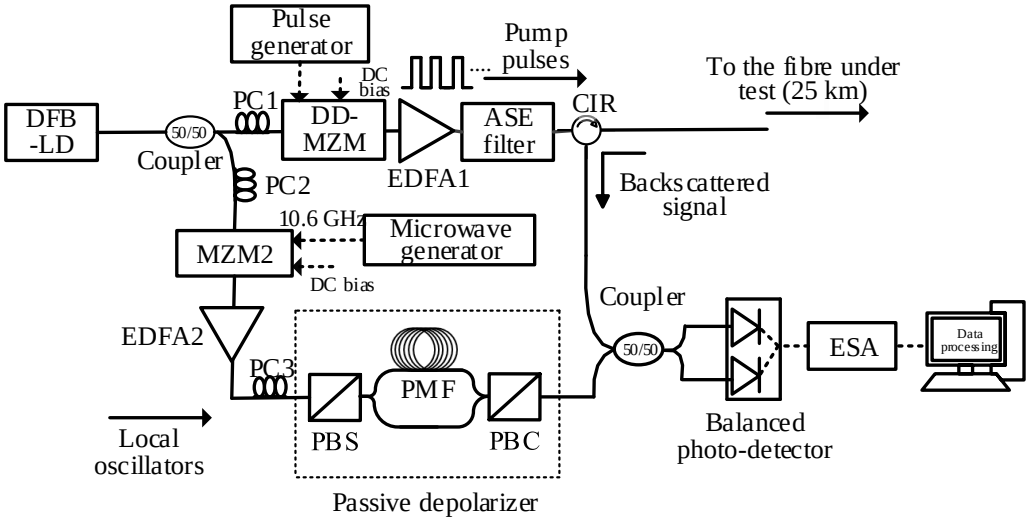

Figure 7.3. Experimental setup of BOTDR sensing system

(DFB= distributed-feedback laser, PC= polarization controller, MZM=Mach-Zehnder modulator, DD-MZM=dual drive-MZM, EDFA=erbium doped fibre amplifier, ASE=amplified spontaneous emission, PBS=polarization beam splitter, PMF=polarization maintaining fibre, CIR=circulator, ESA=electrical spectrum analyser)

7.5 Simultaneous Integration of LTE-RoF Data System and BOTDR Sensing System

The experimental setup for integration of LTE-RoF data system and BOTDR sensing system is illustrated Figure 7.4. The measured optical spectrums of different locations are illustrated in Figure 7.5. The proposed system parameters of both data system and sensing system are shown in Table **7.1**.

In order to mitigate the interference and maintain the optical spectral efficiency, the proposed system is designed with two dedicated wavelengths each for data system and sensing system. The complete BOTDR sensing system is located at one end, as the input pump signal and backscattered signal operated at the same end of the fibre. The pulse width set at 50 ns, corresponds to 5 m spatial resolution and the pulse period is 255 μs, whereas the pulse repetition frequency is 4 kHz. The data system is composed of a QPSK, 16-QAM and 64-QAM with a bit rate of 20, 40 and 60 Mbps, respectively. It is significant to employ an isolator after the data system transmitter; therefore, the signal reflections do

not impact on the data system operation. The data signal and the sensor signal are simultaneously sent through a multiplexer and then sent to a 25 km single-mode silica fibre. At the receiver, a band-pass filter (BPF) is used to eliminate the sensor signal and simply allowed the data signal. Therefore, the data detection at the receiver will not be influenced by the sensor signal.

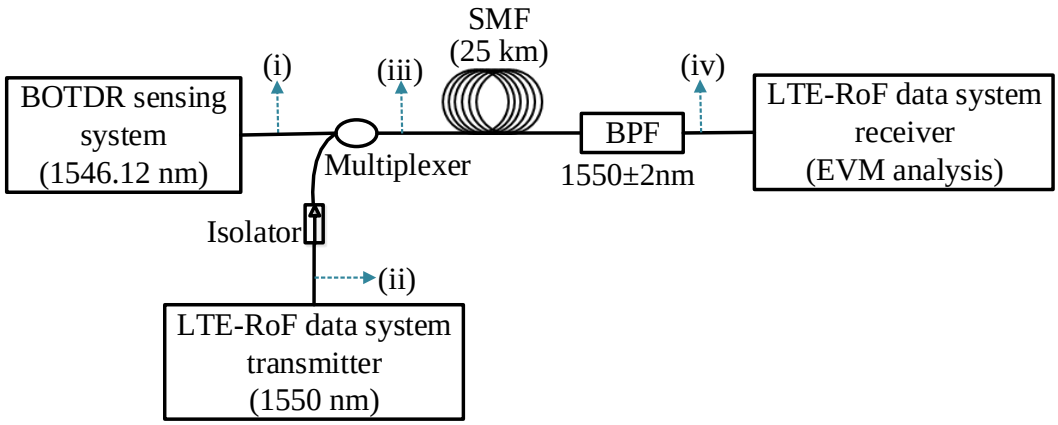

Figure 7.4. Experimental setup for integration of LTE-RoF data system and BOTDR sensing system using a single optical fibre

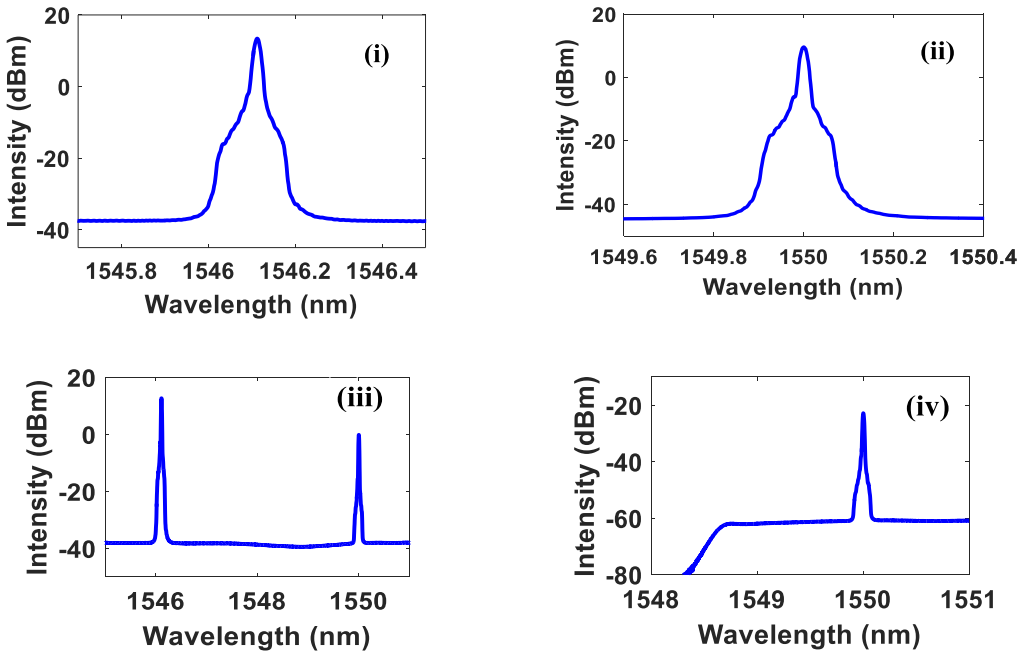

Figure 7.5. Measured optical spectrums of (i) BOTDR sensing system (ii) LTE-RoF data system (iii) after multiplexer and (iv) after band-pass filter (BPF)

Table 7.1. System Parameters

Parameter	Value
LTE-RoF Data system	
Optical wavelength	1550 nm
Optical power	0 to 10 dBm
Modulation scheme	QPSK, 16-QAM and 64-QAM
Bit rate	QPSK=20 Mbps 16-QAM= 40 Mbps 64-QAM=60 Mbps
Baseband multiplexing	OFDM
Carrier frequency	2.6 GHz
Signal bandwidth	10 MHz
RF power	0 dBm
MZM bandwidth/insertion loss	20 GHz/6.1 dB
EDFA gain, noise figure	28 dB, 3.8 dB
SMF length	25 km
PD responsivity	0.95 A/W (@1550 nm)
LNA-gain, NF (dB)	25 dB, 1.6 dB
BOTDR sensing system	
Optical wavelength	1546.12 nm
Optical power	14, 16 and 18 dBm
Pulse width/period	50 ns/255μs
Pulse repetition rate	4.2 KHz
EDFA1&2 gain, noise figure	30 dB, 4 dB
ASE filter passband	1545-1555 nm
PD responsivity	0.95 A/W (@1550 nm)

7.6 Results Discussions

In order to evaluate the data system performance in the presence of sensing signal, the EVM is analysed at different sensing power levels of 14, 16 and 18 dBm. In experiments, the EVM is estimated using an Agilent VSA software, which is connected to the signal analyser. Firstly, the EVM performance is analysed based on QPSK modulation using a 10 MHz bandwidth at 2.6 GHz carrier frequency. Figure 7.6 shows the measured EVM values against the different data powers at three fixed sensing power levels.

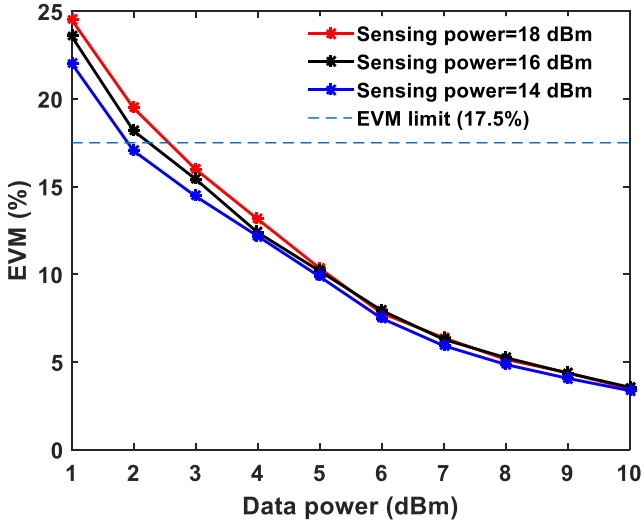

Figure 7.6. Measured EVM for various data powers at a fixed sensing power. The LTE modulation format is QPSK with 10 MHz bandwidth

The EVM values at 1 dBm data power, are ~24.5%, ~ 23.5% and ~ 22.1%, obtained with the sensing powers of 18 dBm, 16 dBm and 14 dBm, respectively. At the 10 dBm data power, the measured EVM values are approximately same as ~3.5% for different sensing powers. The wavelength spacing is sufficiently large, whereas the BPF successively eliminates the sensing power before data detection at the receiver end. Thereafter, at a fixed sensing power of 18 dBm, the EVM analysed with and without BPF

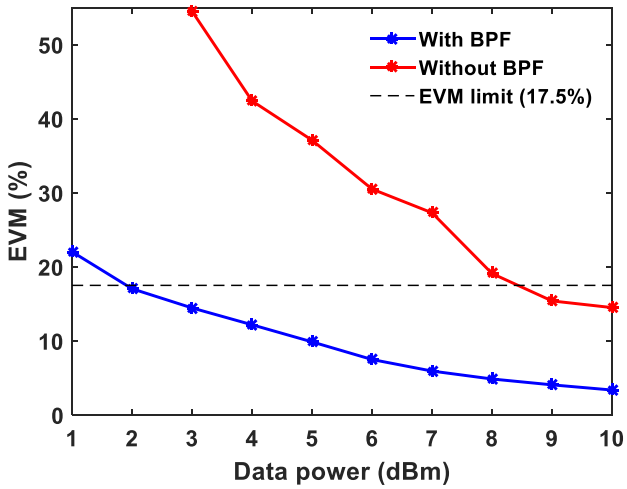

Figure 7.7. Measured EVM with and without band-pass filter (BPF) for various data powers and fixed sensing power of 18 dBm

are shown in Figure 7.7. Without BPF, the sensing signal power is significantly influence the data signal, thus degrades the data system performance.

Thereafter, the EVM values are analysed for 16-QAM and 64-QAM modulation formats independently. The measured EVM values at a fixed sensing powers are shown in Figure 7.8(a) and (b), respectively. In both modulation formats, at a 10 dBm data power, the EVM values are approximately the same for various sensing powers. The obtained EVM values for 16-QAM and 64-QAM at 10 dBm data power are ~3.4% and ~3.6%, respectively.

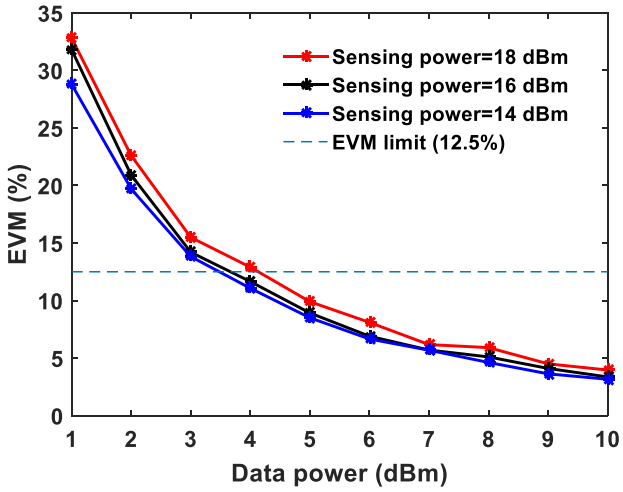

(a)

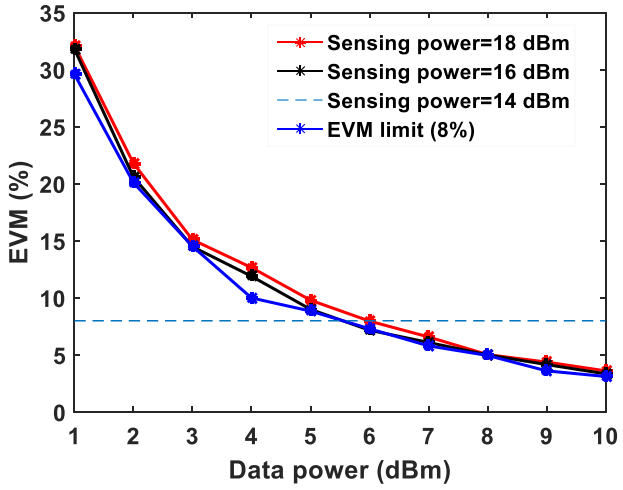

(b)

Figure 7.8. Measured EVM for various data powers at a fixed sensing power, (a) 16-QAM (b) 64-QAM with 10 MHz bandwidth

The temperature effects have been characterized both on data system and sensing system. The 25 km fibre was kept in a temperature controlled oven and subject to a range of temperatures. The data power and sensing power are fixed at 10 dBm and 18 dBm, respectively. The EVM values of the data system (64-QAM) and Brillouin gain spectrum (BGS) of the sensing system has been measured simultaneously and the results are shown in Figure 7.9(a) and (b). The measured EVM values are fitted with a linear fit and the obtained slope is 0.024±0.00025%/^{o}C. At room temperature (~25^{o}C), the obtained Brillouin frequency shift is 10.89 GHz and the slope (temperature sensitivity) is 1.07±0.013 MHz/^{o}C.

At the room temperature (~25^{o}C) and at a fixed data power (10 dBm) and a sensing power (18 dBm), the three- dimensional Brillouin spectrum is obtained and shown in Figure 7.10. In order to obtain a three-dimensional spectral mapping, the frequencies are swept from 10.85 GHz to 10.95 GHz with a frequency step of 1 MHz and 2000 trace averages. The measured BFS profile over the 25 km fibre is shown in Figure 7.10 inset.

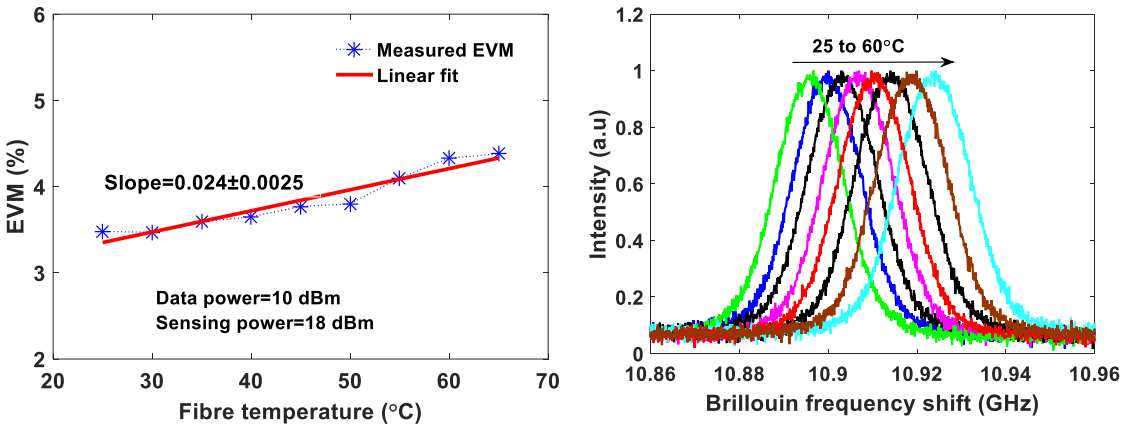

(a) (b)

Figure 7.9. The temperature effects on (a) data system EVM performance (b) sensing system Brillouin gain spectrum (BGS)

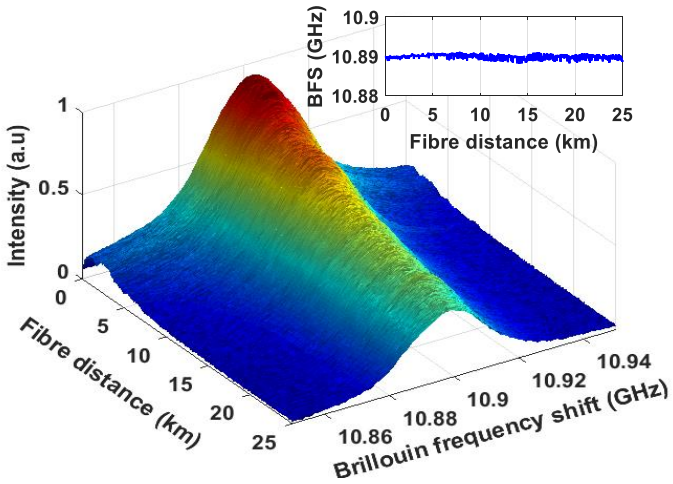

Figure 7.10. Three-dimensional distribution of Brillouin gain spectrum over the fibre distance. Inset: BFS distribution over fibre distance

Finally, in order to evaluate the sensing performance and spatial resolution of the sensing system in the presence of active data transmission, a 20 m fibre at end of the sensing fibre is kept in the temperature oven, while the rest of the fibre is at strain free and ambient room temperature (~25^{o}C). The temperature was set at 50^{o}C within the oven. The BFS distribution of the complete sensing fibre is shown in Figure 7.11 inset. The spatial resolution of 5 m is obtained as shown in Figure 7.11. For a 25^{o}C temperature change, the measured BFS value from the Figure 7.11 is 27.36 MHz. However, the

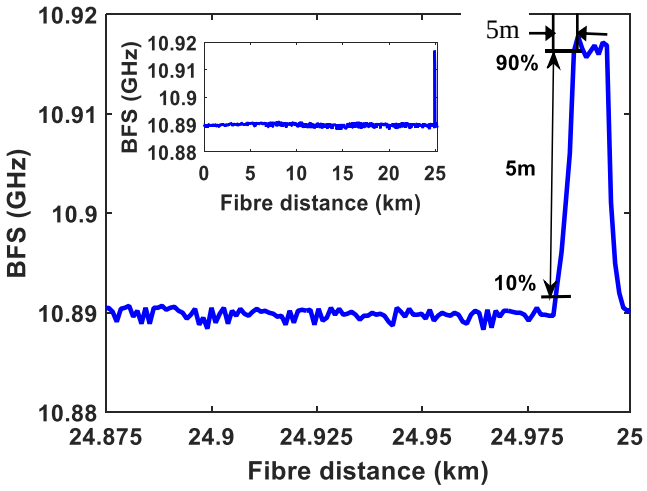

Figure 7.11. BFS distribution over fibre distance under 50^{o}C temperature on 20 m fibre at end of the sensing fibre. Inset: BFS over the whole length of the fibre

expected value for 25^{o}C temperature change is 26.75 MHz (1.07 MHz/^{o}C). Therefore, the temperature measurement error is 0.61 MHz, which corresponds to the temperature error of 0.57^{o}C. The results demonstrate an accurate temperature measurement without any effects originates from the data signal.

7.7 Summary

In this chapter, the simultaneous integration of LTE RoF data system and BOTDR sensing using a single optical fibre was proposed and demonstrated. Using a 25 km single-mode silica fibre, the optimised BOTDR sensing powers of 14, 16 and 18 dBm and LTE RoF data system powers from 0 to 10 dBm, the EVM performance has been analysed. The EVM was analysed for three modulation formats of QPSK, 16-QAM and 64-QAM independently. At an 18 dBm sensing power, the obtained EVM values for 16-QAM and 64-QAM at 10 dBm data power are ~3.4% and ~3.6%, respectively. The influence of sensing power on EVM performance at the data system receiver was investigated with and without band-pass filter (BPF). Thereafter, the various temperature effects on 25 km fibre under test have been demonstrated, which we found that the data system EVM is 0.024±0.00025%/^{o}C and the sensing system temperature sensitivity is 1.07±0.013 MHz/^{o}C. Finally, the sensing performance and spatial resolution of the sensing system has been investigated. For this purpose, a 20 m fibre at end of the fibre is kept in the temperature oven, while the rest of the fibre is at strain free and ambient room temperature (~25^{o}C). The proposed simultaneous integration of data and sensing system utilizes an existing active data transmission cable along the rail-track side, which significantly reduces the fibre optic infrastructure cost.

Chapter 8
Conclusions and Future Work

8.1 Conclusions

This thesis has presented performance improvement techniques for a Brillouin optical time domain reflectometry (BOTDR) system. Firstly, the performance optimisation techniques have been investigated, which includes; (i) a passive depolarizer (ii) employing balanced photodetector (iii) cost-effective Brillouin ring laser and (iv) an inline erbium-doped fibre amplifier (EDFA). It was the principal aim of this research to propose a novel wavelength diversity technique in BOTDR system to overcome the restricted input pump power, which limits the signal-to-noise ratio (SNR) of the system. The proposed wavelength diversity BOTDR has achieved a required rail-track monitoring measurement accuracies of strain (±10 με) and temperature (±0.48^{o}C) at a 50 km sensing distance. Moreover, for the first time, this thesis presented a simultaneous integration of BOTDR sensing system and long-term evolution (LTE) radio over fibre (RoF) data system using a single optical fibre, which can be effectively applied for existing optical fibre link along the rail-track side.

The thesis began with an overview of light scattering effects within the optical fibre, which was explored further in Chapter 2. The different scattering effects, such as Raleigh, Raman and Brillouin scatterings are discussed. The theoretical analysis of linear and nonlinear scattering, and the Brillouin and Raman threshold has been discussed. Due to the importance of the Brillouin scattering, a detailed explanation was given with comparison with Raman scattering.

Focusing on the current state of the technology, Chapter 3 reviewed the distributed fibre sensor techniques, which were based on Raleigh, Raman and Brillouin scattering. The operating principles with their schematic representations have been described. The different applications of distributed sensors are discussed. The Brillouin based distributed fibre sensor systems and their well-known techniques and achievements are summarized.

Chapter 4 describes the experimental investigation of the standard BOTDR and BOTDA systems. The experimental test-bed of both BOTDR and BOTDA systems were developed successfully at Northumbria's Photonics Research Laboratory. The strain and temperature effects on the Brillouin frequency shift (BFS) have been analysed, which were 0.05 MHz/με and 1.07 MHz/^{o}C, respectively. In order to eliminate the polarization noise, a simple, low-cost passive depolarizer is adopted and experimentally investigated. the different key factor effects such as, number of trace averages, Brillouin linewidth and sweep frequency step on BFS uncertainty are experimentally investigated and compared with the theoretical analysis. The limited SNR has been identified, which is restricted by the maximum input pump power and the major noise sources are classified.

In order to optimise the BOTDR system performance, Chapter 5 demonstrated the different techniques, includes (i) employing balanced photodetector (ii) cost-effective Brillouin ring laser and (iii) an inline EDFA. The use of a balanced photodetector significantly enhances the Brillouin gain spectrum at the receiver. On the other hand, the Brillouin ring laser (BRL) significantly reduces the receiver bandwidth with a less complexity. Finally, an in-line EDFA was used to compensate the fibre loss and this has been investigated using two 25 km fibre spools to demonstrate a system with a 5 m spatial resolution.

All the previous chapters concentrated on the theoretical analysis and optimised techniques for the BOTDR system performance. It is vital that overcome the nonlinear effects within the sensing fibre, which limits the BOTDR sensing performance.

Therefore, Chapter 6 investigated the proposed wavelength diversity technique, which enables the maximization of the launch pump power, while avoiding the unwanted nonlinear effects. Firstly, the proof-of-concept of proposed wavelength diversity BOTDR (N=3) was demonstrated using a 25 km fibre with a 5 m spatial resolution. At the end of the sensing fibre, the enhanced SNR is up to 4.85 dB, which corresponds to 174% improvement compared to the conventional single wavelength BOTDR. As a further improvement to the proposed system, the wavelength diversity technique was employed in Brillouin ring laser (BRL) based BOTDR system. The proposed system demonstrated with an improved SNR of 5.1 dB, which is 180% improvement compared to the conventional single wavelength BOTDR using 50 km sensing fibre and 5 m spatial resolution. At a 50 km fibre distance, the strain and temperature measurement accuracies were ±10 με and ±0.48^{o}C, respectively. The proposed system is able to provide rail-track condition monitoring which requires strain and temperature accuracies of <±10 με and <±0.5^{o}C over a sensing range of 50 km.

Considering the difficulties of providing new fibre infrastructure for rail-track condition monitoring in terms of installation cost, a system using existing communication fibres is considered. Chapter 7 demonstrated the simultaneous integration of long-term evolution (LTE) radio over fibre (RoF) data system and BOTDR sensing system using a single optical fibre. The LTE-RoF data system is composed of three modulation formats of quadrature phase-shift keying (QPSK), 16-quadrature amplitude modulation (16-QAM) and 64-QAM, which modulated onto orthogonal frequency division multiplexing (OFDM). The EVM performance is analysed for QPSK, 16-QAM and 64-QAM modulation formats using a 10 MHz bandwidth at 2.6 GHz carrier frequency at a fixed sensing powers. The proof-of-concept has been investigated using a 25 km single-mode silica fibre. Uisng 18 dBm of fixed sensing power and 10 dBm data power, the measured EVMs of QPSK, 16-QAM and 64-QAM are 3.5%, 3.4% and 3.6%, respectively. This

simultaneous integration enables to share two emerging applications using a single optical fibre link.

To conclude, a novel wavelength diversity BOTDR system was introduced to improve the SNR and strain and temperature measurement accuracies. Furthermore, utilizing the existing active data transmission cable along the rail-track side, we proposed the simultaneous integration of LTE-RoF data system and BOTDR sensing system using a 25 km fibre and demonstrated for the first time.

8.1 Future Work

It is noteworthy that within the given time frame, the present research has contributed to the design and development of the wavelength diversity BOTDR and an integration of LTE-RoF data system and BOTDR sensing system. In this section, the author recommends further research, which will be carried out in the future to extend the research reported in the present thesis.

This thesis has given a significant attention to optimisation of BOTDR sensing performance and strain, temperature measurement accuracy improvements. In addition, the research focused on the integration of LTE-RoF data system and BOTDR sensing system over single optical fibre.

For further improvements of proposed wavelength diversity BOTDR system in terms of spatial resolution in the range of few centimetres, the method can be freely combined with pulse coding techniques. For instance, the use of return-to-zero (RZ) simplex coding makes it possible to combine with the wavelength diversity technique proposed here. Moreover, in order to improve the sensing range further, the Raman amplification and multiple in-line EDFAs can be further employed in wavelength diversity BOTDR system. On the other hand, we considered only single-mode silica fibre in this research. There are various types of optical fibres, namely gold-coated SMF for improving the

strain/temperature sensitivity and photonic crystal fibres (PCF) to enhance the Brillouin gain response compared to the standard silica SMF.

Furthermore, the integration of LTE-RoF data system and BOTDR sensing system can be exploited into other data transmission systems, (i) dense wavelength division multiplexing (DWDM), which has a channel spacing of 0.8 nm; and (ii) coarse wavelength division multiplexing (CWDM) with a 20 nm channel spacing. Furthermore, the sensing systems, such as BOTDR/BOTDA for strain/temperature monitoring and phase-OTDR for vibration monitoring can be simultaneously employed in an existing data transmission optical fibre link. At high sensing powers, the data transmission performance, such as EVM need to be investigated. These qualitative measurements can be effectively used for simultaneous measurement of strain, temperature, and vibration in DWDM systems or other communication networks applications.

References

[1] P. Ferdinand, "The Evolution of Optical Fiber Sensors Technologies During the 35 Last Years and Their Applications in Structure Health Monitoring," in *7th European Workshop on Structural Health Monitoring*, Nantes, France, 2014.

[2] K. C. Kao and G. A. Hockham, "Dielectric-fibre surface waveguides for optical frequencies," *Proceedings of the Institution of Electrical Engineers*, vol. 113, pp. 1151-1158, 1966.

[3] G. P. Agrawal, *Fiber-Optic Communication Systems*, 2nd ed. John Wiley & Sons, Inc., 1997.

[4] T. H. Maiman, "Stimulated Optical Radiation in Ruby," *Nature*, vol. 187, pp. 493-494, 1960.

[5] B. Scott and H. Rawson, "Preparation of low loss glasses for optical fibre communication systems," *Opto-electronics*, vol. 5, pp. 285-288, 1973.

[6] J. I. Yamada, S. Machida, and T. Kimura, "2 Gbit/s optical transmission experiments at 1.3 Â¿m with 44 km single-mode fibre," *Electronics Letters*, vol. 17, pp. 479-480, 1981.

[7] G. Rajan, *Optical Fiber Sensors: Advanced Techniques and Applications*. CRC Press: Taylor and Francis Group, 2015.

[8] D. Luo, P. Li, Y. Yue, J. Ma, and H. Yang, "In-Fiber Optic Salinity Sensing: A Potential Application for Offshore Concrete Structure Protection," *Sensors* vol. 17, p. 962, 2017.

[9] Z. Liu and H.-Y. Tam, "Industrial and medical applications of fiber Bragg gratings (Invited Paper)," *Chinese Optics Letters*, vol. 14, p. 120007, 2016.

[10] H. Murayama, H. Igawa, K. Omichi, and Y. Machijima, "Application of distributed sensing with longlength FBG to structural health monitoring," in *9th International Conference on Optical Communications and Networks (ICOCN)*, 2010, pp. 18-24.

[11] Z. Fang, K. K. Chin, R. Qu, and H. Cai, *Fundamentals of Optical Fibers*: John Wiley & Sons, Inc., 2012.

[12] P. B. R. Shizhuo Yin, Francis T.S. Yu, *Fiber Optic Sensors*, Second Edition ed. CRC Press 2008.

[13] 2015 Photonic Sensor Consortium Market Survey Report [Online]. Available: http://www.igigroup.com/st/pages/photonic_sensor_report.html

[14] Distributed optical Sensor Market [Online]. Available: https://www.gminsights.com/industry-analysis/optical-sensor-market

[15] Network Rail: The public performance measure (PPM) [Online]. Available: http://www.networkrail.co.uk/about/performance/

[16] A better railway for a better Britain [Online]. Available: http://www.networkrail.co.uk/publications/strategic-business-plan-for-cp5/

[17] The common causes of delays - and what we're doing to reduce their frequency and impact [Online]. Available: http://www.networkrail.co.uk/timetables-and-travel/delays-explained/

[18] Periodic review 2013: Establishing Network Rail's efficient expenditure [Online]. Available: http://orr.gov.uk/__data/assets/pdf_file/0017/1808/pr13-efficient-expenditure-260711.pdf

[19] Arcadia_Factsheet. Modelling the impacts of climate change on cities: economic costs of rail buckle events [Online]. Available: http://www.arcc-network.org.uk/wp-content/pdfs/ARCADIA-09-buckling.pdf

[20] (2018, 26 March 2018). *Corning SMF-28 9/125µm Single Mode Fiber with NexCor Technology (G.652)*. Available:

https://www.fiberoptics4sale.com/collections/construction_bare-fiber/products/smf-28e?variant=51584676245
[21] (2017, 26 March 2018). *Rail Safety and Standards Board (RSSB)- Standards and the rail industry*. Available: https://www.rssb.co.uk/standards-and-the-rail-industry
[22] R. W. Boyd, *Nonlinear Optics*, Third ed.: Academic Press, 2001.
[23] A. Ghatak and K. Thyagarajan., *An Introduction to Fiber Optics*: Cambridge University Press, 1998.
[24] W. P. Ng and N. Lalam, "Future of distributed fiber sensors (invited paper)," in *2016 15th International Conference on Optical Communications and Networks (ICOCN)*, 2016, pp. 1-3.
[25] G. P. Agrawal, *Nonlinear Fiber Optics*, Second ed.: Academic press, 1995.
[26] C. V. Raman, "On the Molecular Scattering of Light in Water and the Colour of the Sea," *Proceedings of the Royal Society of London. Series A*, vol. 101, pp. 64-80, 1922.
[27] T. Horiguchi and M. Tateda, "BOTDA-nondestructive measurement of single-mode optical fiber attenuation characteristics using Brillouin interaction: theory," *Journal of Lightwave Technology*, vol. 7, pp. 1170-1176, 1989.
[28] T. Horiguchi, K. Shimizu, T. Kurashima, M. Tateda, and Y. Koyamada, "Development of a distributed sensing technique using Brillouin scattering," *IEEE Journal of Lightwave Technology*, vol. 13, pp. 1296-1302, 1995.
[29] X. Bao and L. Chen, "Recent Progress in Distributed Fiber Optic Sensors," *Sensors*, vol. 12, pp. 8601-8639, 2012.
[30] B. Stiller, "Brillouin scattering in photonic crystal fiber : from fundamentals to fiber optic sensors," PhD thesis, University of Franche-Comté, 2013.
[31] R. W. Boyd, *Nonlinear Optics, Third Edition*: Academic Press, 2008.
[32] A. K. Ghatak and K. Tyagarajan, *Introduction to Fiber Optics*: Cambridge University Press, 1998.
[33] A. Minardo, "Fiber-optic distributed strain/temperature sensors based on stimulated Brillouin scattering," PhD thesis, Second university of naples, 2004.
[34] D. ALASIA, "advanced trends in nonlinear optics applied to distributed optical-fibre sensors," PhD thesis, Ecole polytechnique, 2006.
[35] A. Minardo, "Fiber-optic distributed strain/temperature sensors based on stimulated Brillouin scattering," PhD thesis, Department of Civil Engineering, Second University of Naples, 2003.
[36] R. W. Shelby, *Nonlinear Optics*: Academic Press, 2003.
[37] P. Oberson, B. Huttner, and N. Gisin, "Frequency modulation via the Doppler effect in optical fibers," *Optics Letters*, vol. 24, pp. 451-453, 1999.
[38] J. Wang, "Distributed Pressure and Temperature Sensing Based on Stimulated Brillouin Scattering," Masters thesis, Virginia Polytechnic Institute and State University, 2013.
[39] M. Harb, W. Peng, G. Sciaini, C. T. Hebeisen, R. Ernstorfer, M. A. Eriksson, *et al.*, "Excitation of longitudinal and transverse coherent acoustic phonons in nanometer free-standing films of Silica (Si)," *Physical Review B*, vol. 79, p. 094301, 2009.
[40] R. M. Shelby, M. D. Levenson, and P. W. Bayer, "Guided acoustic-wave Brillouin scattering," *Physical Review B*, vol. 31, pp. 5244-5252, 1985.
[41] P. J. Thomas, N. L. Rowell, H. M. van Driel, and G. I. Stegeman, "Normal acoustic modes and Brillouin scattering in single-mode optical fibers," *Physical Review B*, vol. 19, pp. 4986-4998, 1979.

[42] S. F. Mafang, "Brillouin Echoes for Advanced Distributed Sensing in Optical Fibres," PhD thesis, Electrical engineering, École polytechnique fédérale de Lausanne 2011.
[43] M. Nikles, L. Thevenaz, and P. A. Robert, "Brillouin gain spectrum characterization in single-mode optical fibers," *IEEE Journal of Lightwave Technology,* vol. 15, pp. 1842-1851, 1997.
[44] B. Brixner, "Refractive-Index Interpolation for Fused Silica*," *Journal of the Optical Society of America,* vol. 57, pp. 674-676, 1967.
[45] P. Benassi, V. Mazzacurati, G. Ruocco, and G. Signorelli, "Elasto-optic constants in silicate glasses: Experiment and theory," *Physical Review B,* vol. 48, pp. 5987-5996, 1993.
[46] V. I. Kovalev and R. G. Harrison, "Threshold for stimulated Brillouin scattering in optical fiber," *Optics Express,* vol. 15, pp. 17625-17630, 2007.
[47] P. Dragic, J. Ballato, A. Ballato, S. Morris, T. Hawkins, P. C. Law, *et al.*, "Mass density and the Brillouin spectroscopy of aluminosilicate optical fibers," *Optical Materials Express,* vol. 2, pp. 1641-1654, 2012.
[48] R. Singh, "C. V. Raman and the Discovery of the Raman Effect," *Physics in Perspective,* vol. 4, pp. 399-420, 2002.
[49] E. L. Buckland and R. W. Boyd, "Measurement of the frequency response of the electrostrictive nonlinearity in optical fibers," *Optics Letters,* vol. 22, pp. 676-678, 1997.
[50] I. Dajani, C. Vergien, C. Robin, and C. Zeringue, "Experimental and theoretical investigations of photonic crystal fiber amplifier with 260 W output," *Optics Express,* vol. 17, pp. 24317-24333, 2009.
[51] R. Y. Chiao, C. H. Townes, and B. P. Stoicheff, "Stimulated Brillouin Scattering and Coherent Generation of Intense Hypersonic Waves," *Physical Review Letters,* vol. 12, pp. 592-595, 1964.
[52] E. L. Buckland and R. W. Boyd, "Electrostrictive contribution to the intensity-dependent refractive index of optical fibers," *Optics Letters,* vol. 21, pp. 1117-1119, 1996.
[53] A. Kobyakov, M. Sauer, and D. Chowdhury, "Stimulated Brillouin scattering in optical fibers," *Advances in Optics and Photonics,* vol. 2, pp. 1-59, 2010.
[54] "Nonlinear Scattering Effects in Optical Fibers," *Progress In Electromagnetics Research,* vol. 74, pp. 379–405, 2007.
[55] R. G. Smith, "Optical Power Handling Capacity of Low Loss Optical Fibers as Determined by Stimulated Raman and Brillouin Scattering," *Applied Optics,* vol. 11, pp. 2489-2494, 1972.
[56] R. Stolen, "Polarization effects in fiber Raman and Brillouin lasers," *IEEE Journal of Quantum Electronics,* vol. 15, pp. 1157-1160, 1979.
[57] S. H. Baek and W. B. Roh, "Single-mode Raman fiber laser based on a multimode fiber," *Optics Letters,* vol. 29, pp. 153-155, 2004.
[58] Y. Aoki, "Properties of fiber Raman amplifiers and their applicability to digital optical communication systems," *IEEE Journal of Lightwave Technology,* vol. 6, pp. 1225-1239, 1988.
[59] Y. T. C. a. T. P. N. Mohamed N Alahbabi, "Long-range distributed temperature and strain optical fibre sensor based on the coherent detection of spontaneous Brillouin scattering with in-line Raman amplification," *Measurement Science and Technology,* vol. 17, pp. 1082–1090, 2006.
[60] A. D. Kersey, M. A. Davis, H. J. Patrick, M. LeBlanc, K. P. Koo, C. G. Askins, *et al.*, "Fiber grating sensors," *Journal of Lightwave Technology,* vol. 15, pp. 1442-1463, 1997.

[61] L. Sang-Mae, S. S. Saini, and J. Myung-Yung, "Simultaneous Measurement of Refractive Index, Temperature, and Strain Using Etched-Core Fiber Bragg Grating Sensors," *Photonics Technology Letters, IEEE,* vol. 22, pp. 1431-1433, 2010.
[62] V. Bhatia, "Applications of long-period gratings to single and multi-parameter sensing," *Optics Express,* vol. 4, pp. 457-466, 1999/05/24 1999.
[63] G. Bai-ou, T. Hwa-yaw, H. Siu-Lau, L. Shun-yee, and D. Xiao-Yi, "Growth of long-period gratings in H2-loaded fiber after 193-nm UV inscription," *IEEE Photonics Technology Letters,* vol. 12, pp. 642-644, 2000.
[64] K. Shimizu, T. Horiguchi, Y. Koyamada, and T. Kurashima, "Coherent self-heterodyne Brillouin OTDR for measurement of Brillouin frequency shift distribution in optical fibers," *IEEE Journal of Lightwave Technology,* vol. 12, pp. 730-736, 1994.
[65] K. P. Koo and A. D. Kersey, "Bragg grating-based laser sensors systems with interferometric interrogation and wavelength division multiplexing," *Lightwave Technology, Journal of,* vol. 13, pp. 1243-1249, 1995.
[66] C. Carpenter, "Distributed Acoustic Sensing for Downhole Production and Injection Profiling," *Journal of Petroleum Technology,* vol. 68, pp. 1541-1542, 2016.
[67] Y. Rui, C. Kechavarzi, F. O'Leary, C. Barker, D. Nicholson, and K. Soga, "Integrity Testing of Pile Cover Using Distributed Fibre Optic Sensing," *Sensors* vol. 17, pp. 1-21, 2017.
[68] A. Datta, V. S.R, S. S. P, A. M.J, N. Gupta, and R. Sundaram, "Experimental Studies using Distributed Fiber Optic Sensor for Aircraft Structural Health Monitoring Applications," in *12th International Conference on Fiber Optics and Photonics*, Kharagpur, 2014, p. M3C.4.
[69] H. Hoff, "Using Distributed Fibre Optic Sensors for Detecting Fires and Hot Rollers on Conveyor Belts," in *2017 2nd International Conference for Fibre-optic and Photonic Sensors for Industrial and Safety Applications (OFSIS)*, 2017, pp. 70-76.
[70] W. Lienhart, "Case studies of high-sensitivity monitoring of natural and engineered slopes," *Journal of Rock Mechanics and Geotechnical Engineering,* vol. 7, pp. 379-384, 2015.
[71] P. Rajeev, J. Kodikara, W. K. Chiu, and T. Kuen, "Distributed Optical Fibre Sensors and their Applications in Pipeline Monitoring," *Key Engineering Materials,* vol. 558, pp. 424-434, 2013.
[72] (2018, 26 March 2018). *5 Cable Killers That Destroy Buried Fiber Cable - Norscan Instruments*. Available: https://www.norscan.com/5-cable-killers-that-destroy-buried-fiber-cable/
[73] How does an OTDR work [Online]. Available: http://blog.cubeoptics.com/index.php/2015/11/how-does-an-otdr-work
[74] M. K. Barnoski and S. M. Jensen, "Fiber waveguides: a novel technique for investigating attenuation characteristics," *Applied Optics,* vol. 15, pp. 2112-2115, 1976.
[75] J. S. Massa, G. S. Buller, A. C. Walker, S. Cova, M. Umasuthan, and A. M. Wallace, "Time-of-flight optical ranging system based on time-correlated single-photon counting," *Applied Optics,* vol. 37, pp. 7298-7304, 1998.
[76] A. Hartog, "A distributed temperature sensor based on liquid-core optical fibers," *Journal of Lightwave Technology,* vol. 1, pp. 498-509, 1983.
[77] T. M. Daley, B. M. Freifeld, J. Ajo-Franklin, S. Dou, R. Pevzner, V. Shulakova, *et al.*, "Field testing of fiber-optic distributed acoustic sensing (DAS) for subsurface seismic monitoring," *The Leading Edge,* vol. 32, pp. 699-706, 2013.

[78] A. Masoudi, M. Belal, and T. P. Newson, "Distributed optical fibre audible frequency sensor," in *23rd International Conference on Optical Fiber Sensors*, Santander, Spain, 2014, pp. 91573T-91573T-4.
[79] J. P. Dakin, D. J. Pratt, G. W. Bibby, and J. N. Ross, "Distributed optical fibre Raman temperature sensor using a semiconductor light source and detector," *Electronics Letters*, vol. 21, pp. 569-570, 1985.
[80] EricssonNetworks, "Distributed Temperature Measurement Using Optical Fibres," *Journal of Fire Protection Engineering*, vol. 13, pp. 129-151, 2003.
[81] M. G. Tanner, S. D. Dyer, B. Baek, R. H. Hadfield, and S. W. Nam, "High-resolution single-mode fiber-optic distributed Raman sensor for absolute temperature measurement using superconducting nano-wire single-photon detectors," *Applied Physics Letters*, vol. 99, pp. 201110:1–201110:3, 2011.
[82] M. Belal and T. P. Newson, "Performance comparison between Raman and Brillouin intensity based sub metre spatial resolution temperature compensated distributed strain sensor," in *12th European Quantum Electronics Conference*, 2011, pp. 1-5.
[83] M. Höbel, J. Ricka, M. Wüthrich, and T. Binkert, "High-resolution distributed temperature sensing with the multiphoton-timing technique," *Applied Optics*, vol. 34, pp. 2955-2967, 1995.
[84] T. Kurashima, T. Horiguchi, H. Izumita, S. Furukawa, and Y. Koyamada, "Brillouin optical-fiber time domain reflectometry," *IEICE Trans. Commun*, vol. E76-B, 1993.
[85] P. C. Wait and T. P. Newson, "Landau Placzek ratio applied to distributed fibre sensing," *Optics Communications*, vol. 122, pp. 141-146, 1996.
[86] T. R. Parker, M. Farhadiroushan, V. A. Handerek, and A. J. Roger, "A fully distributed simultaneous strain and temperature sensor using spontaneous Brillouin backscatter," *IEEE Photonics Technology Letters*, vol. 9, pp. 979-981, 1997.
[87] K. D. Souza, P. C. Wait, and T. P. Newson, "Double-pass configured fibre Mach-Zehnder interferometric optical filter for distributed fibre sensing," *Electronics Letters*, vol. 33, pp. 2148-2149, 1997.
[88] P. C. Wait and A. H. Hartog, "Spontaneous Brillouin-based distributed temperature sensor utilizing a fiber Bragg grating notch filter for the separation of the Brillouin signal," *IEEE Photonics Technology Letters*, vol. 13, pp. 508-510, 2001.
[89] J. Zhang, Y.-Q. Li, and S. Zhang, "Performance analysis of temperature and strain simultaneous measurement system based on heterodyne detection of Brillouin scattering," in *1st Asia-Pacific Conference on Optical Fiber Sensors*, 2008, pp. 1-5.
[90] H. H. Kee, G. P. Lees, and T. P. Newson, "All-fiber system for simultaneous interrogation of distributed strain and temperature sensing by spontaneous Brillouin scattering," *Optics Letters*, vol. 25, pp. 695-697, 2000.
[91] M. Loy, "Understanding and enhancing sensitivity in receivers for wireless applications," *Technical Brief SWRA030*, 1999.
[92] T. Horiguchi, T. Kurashima, and M. Tateda, "Tensile strain dependence of Brillouin frequency shift in silica optical fibers," *IEEE Photonics Technology Letters*, vol. 1, pp. 107-108, 1989.
[93] P. Xu, Y. Dong, J. Zhang, D. Zhou, T. Jiang, J. Xu, *et al.*, "Bend-insensitive distributed sensing in singlemode-multimode-singlemode optical fiber structure by using Brillouin optical time-domain analysis," *Optics Express*, vol. 23, pp. 22714-22722, 2015.

[94] L. Zou, X. Bao, S. Afshar V, and L. Chen, "Dependence of the Brillouin frequency shift on strain and temperature in a photonic crystal fiber," *Optics Letters*, vol. 29, pp. 1485-1487, 2004.
[95] M. Ding, N. Hayashi, Y. Mizuno, and K. Nakamura, "Brillouin gain spectrum dependences on temperature and strain in erbium-doped optical fibers with different erbium concentrations," *Applied Physics Letters*, vol. 102, p. 191906, 2013.
[96] M. Yosuke, H. Zuyuan, and H. Kazuo, "Dependence of the Brillouin Frequency Shift on Temperature in a Tellurite Glass Fiber and a Bismuth-Oxide Highly-Nonlinear Fiber," *Applied Physics Express*, vol. 2, p. 112402, 2009.
[97] Y. Mizuno and K. Nakamura, "Potential of Brillouin scattering in polymer optical fiber for strain-insensitive high-accuracy temperature sensing," *Optics Letters*, vol. 35, pp. 3985-3987, 2010.
[98] K. S. Abedin, "Observation of strong stimulated Brillouin scattering in single-mode As2Se3 chalcogenide fiber," *Optics Express*, vol. 13, pp. 10266-10271, 2005.
[99] Y. Mizuno, N. Hayashi, and K. Nakamura, "Dependences of Brillouin frequency shift on strain and temperature in optical fibers doped with rare-earth ions," *Journal of Applied Physics*, vol. 112, p. 043109, 2012.
[100] M. Nikles, L. Thevenaz, and P. A. Robert, "Brillouin gain spectrum characterization in single-mode optical fibers," *Journal of Lightwave Technology*, vol. 15, pp. 1842-1851, 1997.
[101] M. M. Sally, H. K. Huai, and P. N. Trevor, "Simultaneous distributed fibre temperature and strain sensor using microwave coherent detection of spontaneous Brillouin backscatter," *Measurement Science and Technology*, vol. 12, p. 834, 2001.
[102] K. D. Souza, P. C. Wait, and T. P. Newson, "Characterisation of strain dependence of the Landau-Placzek ratio for distributed sensing," *Electronics Letters*, vol. 33, pp. 615-616, 1997.
[103] M. Yuan, "Distributed optical fibre sensing system based on Brillouin scattering," PhD thesis, Department of Electronic and Information Engineering, The Hong Kong Polytechnique University, 2013.
[104] Y. Li, J. Wang, and Z. Yang, "A Method for Improving BOTDR System Performance," in *2012 Symposium on Photonics and Optoelectronics*, 2012, pp. 1-4.
[105] J. Schroeder, R. Mohr, P. B. Macedo, and C. J. Montrose, "Rayleigh and Brillouin Scattering in K2O–SiO2 Glasses," *Journal of the American Ceramic Society*, vol. 56, pp. 510-514, 1973.
[106] J.-S. Zhang, Y.-Q. Li, and S. Zhang, "Performance analysis of temperature and strain simultaneous measurement system based on heterodyne detection of Brillouin scattering," in *Optical Fiber Sensors Conference, 2008. APOS'08. 1st Asia-Pacific*, 2008, pp. 1-5.
[107] L. Thévenaz, "Brillouin distributed time-domain sensing in optical fibers: state of the art and perspectives," *Frontiers of Optoelectronics in China*, vol. 3, pp. 13-21, 2010.
[108] Y. T. Cho, "An investigation into using optical amplifiers for enhancing Brillouin based optical time domain reflectometry," PhD, Faculty of Engineering, science and mathematics, University of Southampton, 2004.
[109] T. Kurashima, M. Tateda, T. Horiguchi, and Y. Koyamada, "Performance improvement of a combined OTDR for distributed strain and loss measurement by

randomizing the reference light polarization state," *IEEE Photonics Technology Letters,* vol. 9, pp. 360-362, 1997.
[110] C. Li, Y. Lu, X. Zhang, and F. Wang, "SNR enhancement in Brillouin optical time domain reflectometer using multi-wavelength coherent detection," *Electronics Letters,* vol. 48, pp. 1139-1141, 2012.
[111] X. Zhang, Y. Lu, F. Wang, H. Liang, and Y. Zhang, "Development of fully-distributed fiber sensors based on Brillouin scattering," *Photonic Sensors,* vol. 1, pp. 54-61, 2011.
[112] H. H. Kee, G. P. Lees, and T. P. Newson, "Technique for measuring distributed temperature with 35-cm spatial resolution utilizing the Landau-Placzek ratio," *IEEE Photonics Technology Letters,* vol. 12, pp. 873-875, 2000.
[113] C. C. Lee, P. W. Chiang, and S. Chi, "Utilization of a dispersion-shifted fiber for simultaneous measurement of distributed strain and temperature through Brillouin frequency shift," *IEEE Photonics Technology Letters,* vol. 13, pp. 1094-1096, 2001.
[114] S. Yoshiyuki, M. Satoshi, A. Shoji, and K. Yahei, "Prototype double-pulse BOTDR for measuring distributed strain with 20-cm spatial resolution," in *Joint Conference of the Opto-Electronics and Communications Conference and the Australian Conference on Optical Fibre Technology*, 2008, pp. 1-2.
[115] Y. Koyamada, Y. Sakairi, N. Takeuchi, and S. Adachi, "Novel Technique to Improve Spatial Resolution in Brillouin Optical Time-Domain Reflectometry," *IEEE Photonics Technology Letters,* vol. 19, pp. 1910-1912, 2007.
[116] Y. Zhang, X. Wu, Z. Ying, and X. Zhang, "Performance improvement for long-range BOTDR sensing system based on high extinction ratio modulator," *Electronics Letters,* vol. 50, pp. 1014-1016, 2014.
[117] M. Song, Q. Xia, K. Feng, Y. Lu, and C. Yin, "100 km Brillouin optical time-domain reflectometer based on unidirectionally pumped Raman amplification," *Optical and Quantum Electronics,* vol. 48, p. 30, 2015.
[118] Q. Li, J. Gan, Y. Wu, Z. Zhang, J. Li, and Z. Yang, "High Spatial Resolution BOTDR Based on Differential Brillouin Spectrum Technique," *IEEE Photonics Technology Letters,* vol. 28, pp. 1493-1496, 2016.
[119] F. Wang, C. Zhu, C. Cao, and X. Zhang, "Enhancing the performance of BOTDR based on the combination of FFT technique and complementary coding," *Optics Express,* vol. 25, pp. 3504-3513, 2017.
[120] R. Shibata, H. Kasahara, L. P. Elias, and T. Horiguchi, "Improving performance of phase shift pulse BOTDR," *IEICE Electronics Express,* p. 14.20170267, 2017.
[121] M. Alem, M. A. Soto, and L. Thévenaz, "Analytical model and experimental verification of the critical power for modulation instability in optical fibers," *Optics Express,* vol. 23, pp. 29514-29532, 2015.
[122] L. Thevenaz, M. Nikles, A. Fellay, M. Facchini, and P. A. Robert, "Truly distributed strain and temperature sensing using embedded optical fibers," 1998, pp. 301-314.
[123] K. Kishida, C. H. Li, S. Lin, and K. Nishiguchi, "Pulsed pre-pump method to achieve cm-order spatial resolution in Brillouin distributed measuring technique," *IEICE Tech. Rep,* vol. 105, pp. 1-6, 2005.
[124] A. W. Brown, B. G. Colpitts, and K. Brown, "Dark-Pulse Brillouin Optical Time-Domain Sensor With 20-mm Spatial Resolution," *IEEE Journal of Lightwave Technology,* vol. 25, pp. 381-386, 2007.
[125] Z. Mohd Saiful Dzulkefly Bin, T. Tatsuya, and H. Tsuneo, "The use of Walsh code in modulating the pump light of high spatial resolution phase-shift-pulse Brillouin

optical time domain analysis with non-return-to-zero pulses," *Measurement Science and Technology*, vol. 24, p. 094025, 2013.
[126] M. A. Soto, G. Bolognini, and F. D. Pasquale, "Long-range simplex-coded BOTDA sensor over 120km distance employing optical preamplification," *Optics Letters*, vol. 36, pp. 232-234, 2011.
[127] Y. Dong, L. Chen, and X. Bao, "Extending the Sensing Range of Brillouin Optical Time-Domain Analysis Combining Frequency-Division Multiplexing and In-Line EDFAs," *IEEE Journal of Lightwave Technology*, vol. 30, pp. 1161-1167, 2012.
[128] X. Bao, D. J. Webb, and D. A. Jackson, "32-km distributed temperature sensor based on Brillouin loss in an optical fiber," *Optics Letters*, vol. 18, pp. 1561-1563, 1993.
[129] T. Horiguchi, T. Kurashima, and Y. Koyamada, "1 m spatial resolution measurement of distributed brillouin frequency shift in single-mode fibres," in *Proceedings of Optical Fibre Measurement*, 1994, p. 73.
[130] W. Li, X. Bao, Y. Li, and L. Chen, "Differential pulse-width pair BOTDA for high spatial resolution sensing," *Optics Express*, vol. 16, pp. 21616-21625, 2008/12/22 2008.
[131] M. A. Soto, G. Bolognini, F. Di Pasquale, and L. Thévenaz, "Simplex-coded BOTDA fiber sensor with 1 m spatial resolution over a 50 km range," *Optics Letters*, vol. 35, pp. 259-261, 2010.
[132] S. Martin-Lopez, M. Alcon-Camas, F. Rodriguez, P. Corredera, J. D. Ania-Castañon, L. Thévenaz, *et al.*, "Brillouin optical time-domain analysis assisted by second-order Raman amplification," *Optics Express*, vol. 18, pp. 18769-18778, 2010.
[133] H. Q. Chang, X. H. Jia, X. L. Ji, C. Xu, L. Ao, H. Wu, *et al.*, "DBA-Based BOTDA Using Optical Comb Pump and Pulse Coding With a Single Laser," *IEEE Photonics Technology Letters*, vol. 28, pp. 1142-1145, 2016.
[134] R. Ruiz-Lombera, I. Laarossi, L. Rodríguez-Cobo, M. Á. Quintela, J. M. López-Higuera, and J. Mirapeix, "Distributed High-Temperature Optical Fiber Sensor Based on a Brillouin Optical Time Domain Analyzer and Multimode Gold-Coated Fiber," *IEEE Sensors Journal*, vol. 17, pp. 2393-2397, 2017.
[135] A. Fellay, L. Thévenaz, M. Facchini, M. Niklès, and P. Robert, "Distributed sensing using stimulated Brillouin scattering : towards ultimate resolution," in *12th International Conference on Optical Fiber Sensors*, Williamsburg, Virginia, 1997, p. OWD3.
[136] T. Hasegawa and K. Hotate, "Measurement of Brillouin gain spectrum distribution along an optical fiber by direct frequency modulation of a laser diode," 1999, pp. 306-316.
[137] K. Hotate and M. Tanaka, "Enlargement of measurement range of optical-fiber Brillouin distributed strain sensor using correlation-based continuous-wave technique," in *Conference on Lasers and Electro-Optics*, Baltimore, USA, 2001, pp. 119-120.
[138] J. H. Jeong, K. Lee, K. Y. Song, J.-M. Jeong, and S. B. Lee, "Differential measurement scheme for Brillouin Optical Correlation Domain Analysis," *Optics Express*, vol. 20, pp. 27094-27101, 2012.
[139] G. Ryu, G. T. Kim, K. Y. Song, S. B. Lee, and K. Lee, "BOCDA system enhanced by concurrent interrogation of multiple correlation peaks with a 10 km sensing range," in *2017 25th Optical Fiber Sensors Conference (OFS)*, 2017, pp. 1-4.
[140] KeysightTechnologies, "Keysight Technologies Digital Communication Analyzer (DCA), Measure Relative Intensity Noise (RIN)," ed, 2014.

[141] Y.-Q. Hao, Q. Ye, Z.-Q. Pan, H.-W. Cai, and R.-H. Qu, "Influence of laser linewidth on performance of Brillouin optical time domain reflectometry," *Chinese Physics B,* vol. 22, p. 074214, 2013.
[142] H. Ludvigsen, M. Tossavainen, and M. Kaivola, "Laser linewidth measurements using self-homodyne detection with short delay," *Optics Communications,* vol. 155, pp. 180-186, 1998.
[143] P. Goldberg, P. W. Milonni, and B. Sundaram, "Theory of the fundamental laser linewidth," *Physical Review A,* vol. 44, pp. 1969-1985, 1991.
[144] L. B. Mercer, "1/f frequency noise effects on self-heterodyne linewidth measurements," *IEEE Journal of Lightwave Technology,* vol. 9, pp. 485-493, 1991.
[145] O. Ishida, "Delayed-self-heterodyne measurement of laser frequency fluctuations," *Journal of Lightwave Technology,* vol. 9, pp. 1528-1533, 1991.
[146] H. Tsuchida, "Simple technique for improving the resolution of the delayed self-heterodyne method," *Optics Letters,* vol. 15, pp. 640-642, 1990.
[147] E. Voges and A. Neyer, "Integrated-optic devices on LiNbO3 for optical communication," *IEEE Journal of Lightwave Technology,* vol. 5, pp. 1229-1238, 1987.
[148] J. Svarny, "Bias driver of the Mach–Zehnder intensity electro–optic modulator, based on harmonic analysis," *Advances in robotics, mechatronics and circuits,* vol. 6, pp. 184-189, 20`4.
[149] P. S. Devgan, J. F. Diehl, V. J. Urick, C. E. Sunderman, and K. J. Williams, "Even-order harmonic cancellation for off-quadrature biased Mach-Zehnder modulator with improved RF metrics using dual wavelength inputs and dual outputs," *Optics Express,* vol. 17, pp. 9028-9039, 2009.
[150] N. Lalam, W. P. Ng, X. Dai, Q. Wu, and Y. Q. Fu, "Analysis of Brillouin Frequency Shift in Distributed Optical Fiber Sensor System for Strain and Temperature Monitoring," in *Proceedings of the 4th International Conference on Photonics, Optics and Laser Technology (PHOTOPTICS)*, Rome, Italy, 2016, pp. 335-342.
[151] M. D. Mermelstein, "SBS threshold measurements and acoustic beam propagation modeling in guiding and anti-guiding single mode optical fibers," *Optics Express,* vol. 17, pp. 16225-16237, 2009.
[152] G. P. Agrawal, "Chapter 9 - Stimulated Brillouin Scattering," in *Nonlinear Fiber Optics (Second Edition)*, ed Boston: Academic Press, 1995, pp. 370-403.
[153] F. Poletti, K. Furusawa, Z. Yusoff, N. G. R. Broderick, and D. J. Richardson, "Nonlinear tapered holey fibers with high stimulated Brillouin scattering threshold and controlled dispersion," *Journal of the Optical Society of America B,* vol. 24, pp. 2185-2194, 2007.
[154] G. Samavedam and A. Kish, "Continuous welded rail track buckling safety assurance through field measurements of track resistance and rail force," *Transportation Research Record,* 1995.
[155] W. Ping, X. Kaize, S. Liyang, Y. Lianshan, X. Jingmang, and C. Rong, "Longitudinal force measurement in continuous welded rail with bi-directional FBG strain sensors," *Smart Materials and Structures,* vol. 25, p. 015019, 2016.
[156] M. O. Deventer and A. J. Boot, "Polarization properties of stimulated Brillouin scattering in single-mode fibers," *IEEE Journal of Lightwave Technology,* vol. 12, pp. 585-590, 1994.
[157] M. Song, B. Zhao, and X. Zhang, "Optical coherent detection Brillouin distributed optical fiber sensor based on orthogonal polarization diversity reception," *Chinese Optics Letters,* vol. 3, pp. 271-274, 2005.

[158] Y. Cao, Q. Ye, Z. Pan, H. Cai, R. Qu, Z. Fang, *et al.*, "Mitigation of polarization fading in BOTDR sensors by using optical pulses with orthogonal polarizations," 2014, pp. 915764-915764-4.
[159] J. V. Rees, "Impact of coherence length on the amplitude variations of the delay power profile in a mobile environment," *Electronics Letters,* vol. 22, pp. 1078-1079, 1986.
[160] X. Zhang, R. Wang, and Y. Yao, "Brillouin optical time domain reflectometry using a reference Brillouin ring laser," in *22nd International Conference on Optical Fiber Sensors*, China, 2012, pp. 84219G-84219G-4.
[161] Y. Cao, Q. Ye, Z. Pan, H. Cai, R. Qu, Z. Fang, *et al.*, "Mitigation of polarization fading in BOTDR sensors by using optical pulses with orthogonal polarizations," in *23rd International Conference on Optical Fiber Sensors*, Spain, 2014, pp. 915764-915764-4.
[162] M. A. Soto and L. Thévenaz, "Modeling and evaluating the performance of Brillouin distributed optical fiber sensors," *Optics Express,* vol. 21, pp. 31347-31366, 2013.
[163] X. Angulo-Vinuesa, S. Martin-Lopez, P. Corredera, and M. Gonzalez-Herraez, "Raman-assisted Brillouin optical time-domain analysis with sub-meter resolution over 100 km," *Optics Express,* vol. 20, pp. 12147-12154, 2012/05/21 2012.
[164] M. A. Soto, S. Faralli, M. Taki, G. Bolognini, and F. Di Pasquale, "BOTDA sensor with 2-m spatial resolution over 120 km distance using bi-directional distributed Raman amplification," 2011, pp. 775325-775325-4.
[165] M. Alem, M. A. Soto, and L. Thévenaz, "Modelling the depletion length induced by modulation instability in distributed optical fibre sensors," in *OFS2014 23rd International Conference on Optical Fiber Sensors*, 2014, p. 4.
[166] Y. Q. Hao, Y. Qing, Z. Q. Pan, H. W. Cai, and R. H. Qu, "Influence of laser linewidth on performance of Brillouin optical time domain reflectometry," *Chinese Physics B,* vol. 22, p. 074214, 2013.
[167] V. Lecoeuche, M. W. Hathaway, D. J. Webb, C. N. Pannell, and D. A. Jackson, "20-km distributed temperature sensor based on spontaneous Brillouin scattering," *IEEE Photonics Technology Letters,* vol. 12, pp. 1367-1369, 2000.
[168] E. Säckinger, "Photodetectors, in Broadband Circuits for Optical Fiber Communication," in *Fundamentals of Solid State Engineering*, M. Razeghi, Ed., ed Boston, MA: John Wiley & Sons, 2002, pp. 545-581.
[169] Y. Lu, Y. Yao, X. Zhao, F. Wang, and X. Zhang, "Influence of non-perfect extinction ratio of electro-optic modulator on signal-to-noise ratio of BOTDR," *Optics Communications,* vol. 297, pp. 48-54, 2013.
[170] N. Lalam, W. P. Ng, X. Dai, Q. Wu, and Y. Q. Fu, "Performance improvement of BOTDR system using wavelength diversity technique," in *25th International Conference on Optical Fiber Sensors (OFS)*, Korea, 2017, pp. 1032366-1032366-4.
[171] A. Zornoza, M. Sagues, and A. Loayssa, "Self-Heterodyne Detection for SNR Improvement and Distributed Phase-Shift Measurements in BOTDA," *IEEE Journal of Lightwave Technology,* vol. 30, pp. 1066-1072, 2012.
[172] A. Motil, R. Hadar, I. Sovran, and M. Tur, "Gain dependence of the linewidth of Brillouin amplification in optical fibers," *Optics Express,* vol. 22, pp. 27535-27541, 2014.
[173] S. T. Davey, D. L. Williams, B. J. Ainslie, W. J. M. Rothwell, and B. Wakefield, "Optical gain spectrum of GeO/sub 2/-SiO/sub 2/ Raman fibre amplifiers," *IEE Proceedings J - Optoelectronics,* vol. 136, pp. 301-306, 1989.

[174] V. R. Supradeepa, "Stimulated Brillouin scattering thresholds in optical fibers for lasers linewidth broadened with noise," *Optics Express,* vol. 21, pp. 4677-4687, 2013.
[175] L. Nageswara, N. Wai Pang, D. Xuewu, W. Qiang, and F. Yong Qing, "Performance analysis of Brillouin optical time domain reflectometry (BOTDR) employing wavelength diversity and passive depolarizer techniques," *Measurement Science and Technology,* 2017.
[176] M. A. Soto, A. L. Ricchiuti, L. Zhang, D. Barrera, S. Sales, and L. Thévenaz, "Time and frequency pump-probe multiplexing to enhance the signal response of Brillouin optical time-domain analyzers," *Optics Express,* vol. 22, pp. 28584-28595, 2014.
[177] D. Y. Tang, W. S. Man, H. Y. Tam, and M. S. Demokan, "Modulational instability in a fiber soliton ring laser induced by periodic dispersion variation," *Physical Review A,* vol. 61, p. 023804, 2000.
[178] S. P. Singh and N. Singh, "Nonlinear effects in optical fibers: origin, management and applications," *Progress In Electromagnetics Research,* vol. 73, pp. 249-275, 2007.
[179] X. Zhang, R. Wang, and Y. Yao, "Brillouin optical time domain reflectometry using a reference Brillouin ring laser," 2012, pp. 84219G-84219G-4.
[180] D. Iida and F. Ito, "Cost-effective bandwidth-reduced Brillouin optical time domain reflectometry using a reference Brillouin scattering beam," *Applied Optics,* vol. 48, pp. 4302-4309, 2009.
[181] D. Iida and F. Ito, "Low-Bandwidth Cost-Effective Brillouin Frequency Sensing Using Reference Brillouin-Scattered Beam," *IEEE Photonics Technology Letters,* vol. 20, pp. 1845-1847, 2008.
[182] N. Lalam, W. P. Ng, and X. Dai, "Employing wavelength diversity technique to enhance the Brillouin gain response in BOTDA system," in *Optical Fiber Communication Conference (OFC)*, Anaheim, California, 2016, p. M2D.4.
[183] N. Lalam, W. P. Ng, X. Dai, and H. K. Al-Musawi, "Characterization of Brillouin frequency shift in Brillouin Optical Time Domain Analysis (BOTDA)," in *20th European Conference on Networks and Optical Communications - (NOC),* 2015, pp. 1-4.
[184] M. Alem, M. A. Soto, and L. Thévenaz, "Modelling the depletion length induced by modulation instability in distributed optical fibre sensors," in *23rd International Conference on Optical Fiber Sensors*, Spain, 2014, pp. 91575S-91575S-4.
[185] Y. Aoki and K. Tajima, "Stimulated Brillouin scattering in a long single-mode fiber excited with a multimode pump laser," *Journal of the Optical Society of America B,* vol. 5, pp. 358-363, 1988.
[186] M. A. Soto, G. Bolognini, and F. D. Pasquale, "Distributed optical fibre sensors based on spontaneous Brillouin scattering employing multimode Fabry-Perot lasers," *Electronics Letters,* vol. 45, pp. 1071-1072, 2009.
[187] H. Lee, N. Hayashi, Y. Mizuno, and K. Nakamura, "Observation of Brillouin gain spectrum in optical fibers in telecommunication band: Effect of pump wavelength," *IEICE Electronics Express,* vol. 13, pp. 1066-1076, 2016.
[188] J. Hu, B. Chen, G. Li, and Z. Lin, "Methods for signal-to-noise ratio improvement on the measurement of temperature using BOTDR sensor," in *Proc. of Advanced Sensor Systems and Applications IV*, 2010, pp. 785309-785309-7.
[189] Nageswara Lalam, Wai Pang Ng, Xuewu Dai, Qiang Wu, and Y. Q. Fu, "Performance analysis of Brillouin optical time domain reflectometry (BOTDR) employing wavelength diversity and passive depolarizer techniques," *Measurement Science and Technology,* 2017.

[190] W. P. N. N. Lalam, X. Dai, Q. Wu and Y. Q Fu, "Performance Improvement of Brillouin Ring Laser based BOTDR System Employing a Wavelength Diversity Technique," *IEEE/OSA Journal of Lightwave Technology*, pp. 1-1, 2017.
[191] R. D. Programme, "Measurement, Modelling and Mapping to Predict Rail Temperature," ed, p. 4.
[192] C. Park and T. S. Rappaport, "Short-Range Wireless Communications for Next-Generation Networks: UWB, 60 GHz Millimeter-Wave WPAN, And ZigBee," *IEEE Wireless Communications*, vol. 14, pp. 70-78, 2007.
[193] S. Chatzi and I. Tomkos, "Techno-economic study of high-splitting ratio PONs and comparison with conventional FTTH-PONs/FTTH-P2P/FTTB and FTTC deployments," in *2011 Optical Fiber Communication Conference and Exposition and the National Fiber Optic Engineers Conference*, 2011, pp. 1-3.
[194] S. Ohmori, Y. Yamao, and N. Nakajima, "The future generations of mobile communications based on broadband access technologies," *IEEE Communications Magazine*, vol. 38, pp. 134-142, 2000.
[195] J. R. C. a. S. V. António Barrias, "A Review of Distributed Optical Fiber Sensors for Civil Engineering Applications," *Sensors*, vol. 16, pp. 1-35, 2016.
[196] T. Horiguchi, T. Kurashima, and M. Tateda, "A technique to measure distributed strain in optical fibers," *IEEE Photonics Technology Letters*, vol. 2, pp. 352-354, 1990.
[197] P. Munster, J. Radil, J. Vojtech, O. Havlis, T. Horvath, V. Smotlacha, *et al.*, "Simultaneous transmission of the high-power phase sensitive OTDR, 100Gbps dual polarisation QPSK, accurate time/frequency, and their mutual interferences," in *Fiber Optic Sensors and Applications XIV*, Anaheim, California, 2017, p. 102080D.
[198] S. Al-Janabi, I. Al-Shourbaji, M. Shojafar, and S. Shamshirband, "Survey of main challenges (security and privacy) in wireless body area networks for healthcare applications," *Egyptian Informatics Journal*, vol. 18, pp. 113-122, 2017.
[199] H. Al-Raweshidy and S. Komaki, *Radio over Fiber Technologies for Mobile Communications Networks*. Artech House, 2002.
[200] H. A. Mahmoud and H. Arslan, "Error vector magnitude to SNR conversion for nondata-aided receivers," *IEEE Transactions on Wireless Communications*, vol. 8, pp. 2694-2704, 2009.
[201] Y. D. Chung, K. S. Choi, J. S. Sim, H. K. Yu, and J. Kim, "A 60-GHz-Band Analog Optical System-on-Package Transmitter for Fiber-Radio Communications," *Journal of Lightwave Technology*, vol. 25, pp. 3407-3412, 2007.
[202] R. Schmogrow, B. Nebendahl, M. Winter, A. Josten, D. Hillerkuss, S. Koenig, *et al.*, "Error Vector Magnitude as a Performance Measure for Advanced Modulation Formats," *IEEE Photonics Technology Letters*, vol. 24, pp. 61-63, 2012.